Design of an Exhaust Gas Energy Recovery System for Internal Combustion Engines

Abdallah Ali

A Thesis
in
The Department
of
Mechanical and Industrial Engineering

Presented in Partial Fulfillment of the Requirements
For the Degree of Master of Applied Science in Mechanical Engineering at
Concordia University
Montréal, Québec, Canada

March 2016

CONCORDIA UNIVERSITY
School of Graduate Studies

This is to certify that the thesis prepared

By: Abdallah Ali

Entitled: Design of an Exhaust Gas Energy Recovery System for Internal Combustion Engines

and submitted in partial fulfillment of the requirements for the degree of

Master of Applied Science in Mechanical Engineering

complies with the regulations of the University and meets the accepted standards with respect to originality and quality.

Signed by the final examining committee:

Dr. Marius Paraschivoiu ______ Chair

Dr. Lyes Kadem ______ Examiner

Dr. Fuzhan Nasiri ______ Examiner

Dr. Hoi Dick Ng ______ Supervisor

Approved by ______
Chair of Department or Graduate Program Director

______
Dean of Faculty

Date ______

ABSTRACT

Design of an Exhaust Gas Energy Recovery System for Internal Combustion Engines

Abdallah Ali

The current research paper presents the experimental findings following exhaust runner heat exchanger tests as well as a realistic theoretical proof of concept for steam turbocharging by using said results. A preliminary heat analysis was completed in order to first assess the magnitude of recoverable energy from the spent exhaust gases. Through experimentation, actual heat absorbed by the water was successfully obtained and was higher than predicted. The proof of concept was then completed by inputting the experimental engine parameters into a turbocharged Otto cycle combined to a Rankine cycle using experimental figures for the heat input stages of the assessment. The theory ultimately resulted in peak improvements of 7.446% in engine thermal efficiency and an interesting reduction in brake specific fuel consumption of 6.930% near 2500 RPM. Furthermore, through the use of steam turbocharging, brake engine power can theoretically be improved by 35.00%, resulting in a 13.73% increase in the current experimental engine's power density. The test engine was mounted onto a hydraulic engine dyno and a baseline of its power and torque output was recorded for final confirmation that the heat recuperated via this energy recovery system was not being negated elsewhere in the combined cycle. Finally, a preliminary steam turbine was designed and the optimal system configuration was presented for future use. The obtained results clearly demonstrate that steam turbocharging is a novel energy recovery system with great potential.

ACKNOWLEDGEMENTS

I would like to sincerely thank my supervisor, Dr. Hoi Dick Ng for having given me this great opportunity of completing such an interesting research project. I am truly grateful for his support and guidance throughout this project. I also want to thank him for the trust he bestowed upon me with regards to his instrumentation and for granting me access to his test facilities.

I want to express my gratitude towards the whole Formula SAE team at Concordia for having allowed me to use their engine for my experiments. I specifically want to thank the engine team for their help with running the engine dyno.

Moreover, I want to thank my colleagues, specifically Rocco Portaro for his help in manufacturing the prototype boilers.

I would also like to thank the whole team of the EDML for allowing me the use of their equipment in order to manufacture my parts.

Additionally, I want to thank Gilles Huard for his generous help in calibrating and setting up various sensors essential to the success of the experiments.

Last but not least, a special acknowledgment goes to my parents, my brother and sister for their everlasting support and encouragement throughout the years. I also want to thank all my family and friends for their belief in me.

TABLE OF CONTENTS

LIST OF FIGURES

LIST OF TABLES

NOMENCLATURE

T	Temperature, K
P	Pressure, kPa
ϕ	Equivalency ratio
ρ	Density, $\frac{\mathrm{kg}}{\mathrm{m}^3}$
C_p	Constant pressure specific heat, $\frac{\mathrm{J}}{\mathrm{kg \cdot K}}$
C_v	Constant volume specific heat, $\frac{\mathrm{J}}{\mathrm{kg \cdot K}}$
v	Kinematic viscosity, $\frac{\mathrm{m}^2}{\mathrm{s}}$
μ	Dynamic viscosity, $\frac{\mathrm{kg}}{\mathrm{m \cdot s}}$
k	Thermal conductivity, $\frac{\mathrm{W}}{\mathrm{m \cdot K}}$
R	Gas constant, $\frac{\mathrm{J}}{\mathrm{kg \cdot K}}$
Pr	Prandtl number
γ	Ratio of specific heats
$\dot{m}$	Mass flow rate, $\frac{\mathrm{kg}}{\mathrm{s}}$
V_d	Engine displacement, m^3
N	Engine speed, RPM
η_v	Volumetric efficiency
r_c	Compression ratio
A/F	Air/fuel ratio
$\dot{W}$	Power, kW
η_c	Combustion efficiency
$\dot{Q}$	Heat, kW
f	Residual gas fraction (Eq. 2.11 & 2.12)
f	Friction factor (Eq. 2.24 & 2.25)
η_{th}	Thermal efficiency
Re	Reynolds number
V	Velocity, m/s

D	Diameter, m
h	Convection heat transfer coefficient, $\frac{\mathrm{W}}{\mathrm{m^2 \cdot K}}$
Nu	Nusselt number
A	Area, m^2
ΔT_{lm}	Log mean temperature difference, K
σ	Surface tension, N/m
g	Gravitational acceleration, m/s^2
τ_{out}	Torque output, N · m
	Subscripts
i	Inlet or inner
o	Outer or stagnation
ex	Exhaust
1, 2, ...	State 1, 2, 3, …
in	Input
out	Output
e	Exit
	Superscripts
*	Choked
	Acronyms
ICE	Internal Combustion Engine
ERS	Energy Recovery System
bsfc	Brake Specific Fuel Consumption, $\frac{\mathrm{kg}}{\mathrm{kW \cdot hr}}$
isfc	Indicated Specific Fuel Consumption, $\frac{\mathrm{kg}}{\mathrm{kW \cdot hr}}$
OEM	Original Equipment Manufacturer
FSAE	Formula Society of Automobile Engineers
mep	Mean Effective Pressure, kPa
RPM	Revolution per minute
LHV	Lower heating value, MJ/kg
LMTD	Log Mean Temperature Difference
NTU	Number of Transfer Units

1. INTRODUCTION

Ever since its initial conception, the internal combustion engine (ICE) has undergone several significant design improvements over the years, from the optimization of component geometries to the application of continuously higher performing materials in all areas, maximizing the ICE's power density has always been the driving force behind its development. Currently, ICEs are able to convert approximately 30 to 40% of useful mechanical work from fuels, the remainder of the energy is expelled through exhaust gases, engine cooling systems, heat radiated to the surroundings and friction [1]. This means that there is a significant amount of energy being wasted which could otherwise be recovered in order to produce useful work. It is obvious here that the next great step towards revolutionary increases in the engine’s power density resides in the further development of energy recovery systems.

1.1 Methods Used to Improve Heat Engine’s Efficiencies

The use of an exhaust gas turbocharger has long been applied as a method for reusing the exhaust gases and is thus, in a sense, the pioneer energy recovery system (ERS) used on ICEs. However, its primary use is to boost the pressure of the intake gases which in turn increases the engine’s power by effectively eliminating pumping losses as well as allowing for more air to enter the combustion chamber, consequently allowing for more fuel to be added which then allows for a superior power-stroke. The turbocharger has functional limitations that cap the extent to which it can actually recover energy and can furthermore add restrictions to the ICE due to the characteristics of the energy transfer between the two [2]. It is worthy to note here that the turbocharger was initially invented to improve the engine’s performances [3].

Looking past the turbocharger towards new methods of recovering waste energy from the exhaust gases, new developments yield direct methods such as thermoelectric generators which harness the great temperature difference between the waste heat and the surroundings to produce electricity by means of the Seeback effect and semiconductors. Another way of converting otherwise wasted heat into power is by means of piezoelectric devices which can convert mechanical energy present in the form of ambient vibration into electrical energy. Here a thin film membrane can take advantage of the expansion of exhaust gases, which have a pulsating nature due to the operating characteristics of the engine, and create a voltage output. It should be noted here that piezoelectric devices are mainly used for low temperature ranges, typically 100 to 150℃. The use of thermionic generation has also been identified as a potential energy recovery method. This thermoelectric device operates on thermionic emission which uses a temperature difference in order to drive the flow of electrons through inter-electrode plasma from a hot, typically above 1000℃, emitter electrode, from which electrons are vaporized by thermionic emission, onto a colder collector electrode, where they are condensed. There is also the possibility of using a thermo photo-voltaic process which converts radiant energy into electricity by means of heating an emitter which then emits electromagnetic radiation. Unfortunately these technologies have low efficiencies (approximately 2 to 5%) and are currently high cost [1].

Another direct energy recovery method that merits attention here is the kinetic energy recovery system which recuperates the vehicle's linear momentum. One system that works on this principle is the regenerative braking system which uses an intricate assembly of electrical motors and generators to provide negative torque at the driven wheels in order to slow down the vehicle by converting its kinetic energy to electrical energy which can then recharge the batteries by means of power inverters [4]. Another type of system recovers kinetic energy by coupling a heavy flywheel to the braking system by means of a magnetorheological fluid. During braking manoeuvres, the fluid engages, thus coupling the flywheel to the braking system. The former then spins up by transferring the available linear momentum into rotational kinetic energy. This energy can then be transferred back to the wheels during accelerations thus improving the latter and reducing fuel consumption. This novel type of kinetic energy recovery system weighs less than its rival thanks to the facts that no additional electrical components, such as motors, generators, batteries nor inverters are required [5].

An interesting indirect method of recovering energy from exhaust gases is by means of a steam Rankine cycle [6]. Several electric power generating plants around the world currently use a Rankine cycle to recover energy out of the exhaust gases produced by the gas turbine being used as the primary cycle to generate electricity thus forming a combined Brayton-Rankine cycle. Several automobile manufacturers such as BMW & Honda are therefore turning towards the use of a Rankine cycle in order to develop a new ERS, the Otto-Rankine cycle [6]. This field of research have yielded promising preliminary results, an estimated 15% gain in fuel efficiency according to BMW [6].

1.2 Previous Work on Steam Turbocharging

The remarkable gains by means of steam turbocharging have opened up a new branch in the field of energy recovery systems relative to the internal combustion engines used in the automotive industry. Several researchers have decided to replicate this technology in order to validate the concept and its feasibility to be applied to production vehicles in the future.

By coupling a Rankine cycle to the waste heat side of an Otto cycle, the combined Otto-Rankine cycle is born. Its functioning is fairly straightforward, the high temperature exhaust gases of the Otto cycle are used as the heat input into the Rankine cycle's boiler, thus generating the required superheated steam to drive the turbine. Depending on the system's requirements, the turbine can be either coupled to a compressor or a generator, both resulting in increased power density and therefore better fuel economy can be achieved.

Since the use of steam turbocharging is still in its development stage, there is very little available literature on this subject, yet the preliminary results obtained to date are promising. One research, performed by Fu et al. on an inline four cylinder 1.573L diesel engine, yielded power improvements of 7.2% at 4000 RPM and a noteworthy increase in thermal efficiency from 37.3% to 39.9% accompanied by a decrease of approximately 6.7% in brake specific fuel consumption (*bsfc*). They have also stated in their findings that the addition of a steam turbocharging system has very little impact on the normal operation of an IC engine and it can be directly applied to it without changing its main structure [7].

Furthermore, a great portion of the energy released by the fuel is dissipated into the engine’s cooling and lubricating systems through conduction and friction. In order to further increase the energy recovery capability of this system, the Kalina cycle can be introduced here in series to the Rankine cycle. Although prior research done on this cycle focused on using the low grade waste heat to drive an Organic Rankine Cycle [2] , the purpose of adding a Kalina cycle here would be to first recover the low grade waste heat in these oil and water circuits prior to sending the working fluid of the ERS to get superheated by the engine’s spent exhaust gases.

1.3 Present Work

Since the use of the Otto-Rankine cycle is fairly recent, the purpose of the present research is that of an independent, unbiased proof of concept which can then be used as a benchmark for further research activities in this field. System weaknesses will be identified and improvements or alternatives will be proposed along the process. This research will be conducted on a Honda CBR600F4i motorcycle engine. In the initial phase, a benchmark of the current engine performances will be recorded on an engine dynamometer in order to properly assess the impact of the Otto-Rankine ERS.

In order to efficiently design a turbine for this system, it will be critical to measure the maximum amount of heat that can be extracted from the exhaust gases, therefore the design of a boiler test will be the essential system component and will therefore be the focus of this research. The experimental boiler design will essentially be comprised of exhaust tubes with outer concentric ones, through which water will flow in direct contact with the runner’s surface for maximum heat transfer. The system performance analysis will therefore be obtained through experimental testing and the measured rise in water temperature along with the corresponding mass flow rates will determine the maximum practical energy which could be extracted from the exhaust system. This experimental data combined with the maximum and minimum temperatures along both independent cycles will lead to an initial analysis of the Rankine cycle. Initial conservative assumptions will be made for the additional energy which can be recovered from the engine’s water and oil coolers by a Kalina cycle [2]. The final magnitude of energy recovered will then lead to the preliminary design of the steam turbine.

2. PRELIMINARY ANALYSIS

2.1 Engine Parameters & Design

This research was conducted on an in-line, 4-cylinder, 600cc, 4-stroke Honda CBR600F4i, water cooled, naturally aspirated gasoline engine with electronic fuel injection. All of the engine's internals were OEM with the exception of a Cometic head gasket and a modified intake camshaft which had the same profile as the exhaust cam yet with a 10° timing advance. The test unit was additionally equipped with a fully custom intake manifold with a flow restrictor of 20 mm in diameter downstream of the throttle body (as per the FSAE regulations). Additional engine specifications are listed in Table 2.1. The engine was controlled by means of a MoTeC M400 electronic control unit along with an independent SuperFlow hydraulic engine dynamometer rig and monitoring of the engine's sensors was achieved via a laptop running the MoTeC software as well as the SuperFlow Xconsole.

Table 2.1 Restricted Engine Specifications [8]

Displacement (L)	0.6
Bore (mm)	67
Stroke (mm)	42.5
Compression Ratio	12.5:1
Peak Power (kW) @ 8000 RPM	46.6
Peak Torque (N · m) @ 8000 RPM	55.3
Engine Weight (wet) (kg)	65.2
Power Density (kW/kg)	0.715
Torque Density (N · m/kg)	0.848

2.2 Preliminary Heat Analysis

2.2.1 Otto Cycle Analysis

In order to obtain a good estimate of the quantity of energy contained and thus released through the exhaust gases, it is essential to start the research with a careful Otto cycle study of this particular engine. This initial exercise will ultimately result in the theoretical calculation of the combustion gases temperature in the exhaust stroke, which will then be used further on to obtain key parameters of the heat exchange process occurring in the exhaust runners.

Theoretical calculations from here on in shall be completed using the values supplied in Table 2.2 below. From prior experimental runs using this engine configuration, the air on the intake side has been measured to be, on average, T_i = 298 K and P_i = 96 kPa and the exhaust gas properties have been obtained by setting the air/fuel ratio slightly rich, namely to 14.54 ($\phi = 1.05$), in GASEQ, a software specifically created to obtain combustion gases properties under various conditions.

Table 2.2 Intake and Exhaust Gas Properties

	Air	**Exhaust**
$\boldsymbol{\rho}\left(\frac{\mathbf{kg}}{\mathbf{m^3}}\right)$	1.127	0.2996
$\boldsymbol{C_p}\left(\frac{\mathbf{J}}{\mathbf{kg\cdot K}}\right)$	1006	1327
$\boldsymbol{C_v}\left(\frac{\mathbf{J}}{\mathbf{kg\cdot K}}\right)$	719.6	1027
$\boldsymbol{\upsilon}\left(\frac{\mathbf{m^2}}{\mathbf{s}}\right)$	1.639E-05	1.550E-04
$\boldsymbol{\mu}\left(\frac{\mathbf{kg}}{\mathbf{m\cdot s}}\right)$	1.847E-05	4.630E-05
$\boldsymbol{k}\left(\frac{\mathbf{W}}{\mathbf{m\cdot K}}\right)$	0.02610	0.07810
$\boldsymbol{R}\left(\frac{\mathbf{J}}{\mathbf{kg\cdot K}}\right)$	287.0	300.0
Pr	0.7130	0.7868
$\boldsymbol{\gamma}$	1.398	1.292

Through this analysis, various parameters will be determined, yet the ones of interest will specifically be the net work output, the thermal efficiency, the mean effective pressure (*mep*) and of course the temperature of the exhaust gases at the end of the exhaust stroke following their expansion into the runners. All states are depicted in Figure 2.1. Prior to starting the cycle analysis, the engine's air mass flow rate will be determined [9]:

$$\dot{m}_{air} = \frac{V_d \rho N \eta_v}{n_R} \tag{2.1}$$

where $\dot{m}_{air}$ is the intake air mass flow rate, V_d the engine's displacement, ρ the intake air density, N the engine's rotational speed, η_v the engine's volumetric efficiency and n_r the number of engine revolutions to complete one full Otto cycle.

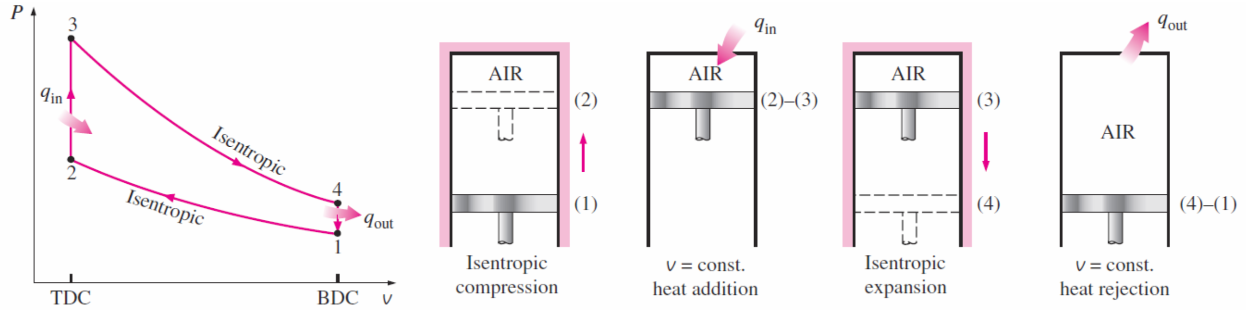

Figure 2.1 Ideal Otto Cycle and its *P*-*V* Diagram [10]

Using the initial parameters, taken to be representative of the intake conditions (state 1), the temperature and pressure of the air at the end of the isentropic compression process (state 2) can be calculated [10]:

State 1: Inlet temperature $T_1 = 298$ K and pressure $P_1 = 96$ kPa

Using the engine's compression ratio of $r_c = 12.5$, $\gamma_{air} = 1.398$ and $\gamma_{ex} = 1.292$

State 2:

$$\frac{T_2}{T_1} = r_c^{\gamma_{air}-1} \tag{2.2}$$

$$\frac{P_2}{P_1} = r_c^{\gamma_{air}} \tag{2.3}$$

Using the literature value of 15.27 as the stoichiometric air/fuel mixture for 94 octane gasoline [9]:

From literature $\phi = 1 \rightarrow {}^{A}/_{F} = 15.27$

$$\dot{m}_{total} = \dot{m}_{air}\left(1 + \frac{\phi}{\left({}^{A}/_{F}\right)_{\phi=1}}\right) \tag{2.4}$$

$$\dot{W}_{in} = \dot{m}_{total}C_{v_{air}}(T_2 - T_1) \tag{2.5}$$

where $T_{1,2}$ and $P_{1,2}$ are the temperatures and pressures of states 1 and 2 respectively, r_c is the engine's compression ratio, γ_{air} the ratio of specific heats for air, $\dot{W}_{in}$ the power required to perform the compression stroke, $\dot{m}_{air}$ the intake air mass flow rate and $C_{v_{air}}$ the specific heat capacity at constant volume of the intake air.

Once the properties of state 2 have been determined, the ones of state 3 can be obtained using constant-volume heat addition process with a combustion efficiency of 95% as is used in similar cases as this one [9].

State 3:

Using $C_v = 0.7191 \ \frac{\text{kJ}}{\text{kg·K}}$ and assuming $\eta_c = 0.95$

$$\dot{Q}_{in} = LHV \cdot \dot{m}_{fuel} \cdot \eta_c = \dot{m}_{total}C_v(T_3 - T_2) \tag{2.6}$$

$$\frac{P_3}{P_2} = \frac{T_3}{T_2} \tag{2.7}$$

where $\dot{m}_{total}$ is the total mass flow rate through the engine including the fuel, $\dot{Q}_{in}$ the heat input during the combustion process, *LHV* the fuel's lower heating value, taken as 44.5 MJ/kg [9], and $\dot{m}_{fuel}$ is the fuel's mass flow rate.

Finally, using the isentropic expansion relations in order to determine the properties at state 4 and therefore the exhaust gas parameters [10]:

State 4:

$$\frac{T_4}{T_3} = \frac{1}{\mathrm{r}_\mathrm{c}^{\gamma_\mathrm{ex}-1}} \tag{2.8}$$

$$\frac{P_4}{P_3} = \frac{1}{r_c^{\gamma_{ex}}} \tag{2.9}$$

where γ_{ex} is the ratio of specific heats for the burnt exhaust gases.

The previously calculated values for state 4 represent the properties of the burnt gases in the combustion chamber right at the end of the expansion stroke. In order to obtain more accurate values during the heat rejection calculations, the temperature and pressure of the spent gases as they exit the exhaust valve should be evaluated and used for further calculations instead of state 4 properties. Using commonly found values in literature for similar engine configurations, the exhaust system pressure (*P_e*) is assumed to be 105 kPa and therefore the temperature of the exhaust gas flowing through the runners can be further refined [9]:

$$T_e = T_4 \left(\frac{P_e}{P_4}\right)^{\frac{\gamma_{ex}-1}{\gamma_{ex}}} \tag{2.10}$$

In order to obtain a more comprehensive model of the cycle, in this step, the residual exhaust gases left inside the combustion chamber following the exhaust stroke are included in the analysis [9]:

$$f = \frac{1}{r_c}\left(\frac{P_e}{P_4}\right)^{\frac{1}{\gamma_{ex}}} \tag{2.11}$$

$$T_1 = (1-f)T_i + fT_e\left[1 - \left(1 - \frac{P_i}{P_e}\right)\left(\frac{\gamma_{ex}-1}{\gamma_{ex}}\right)\right] \tag{2.12}$$

These gases have the effect of raising the state 1 temperature and therefore Eq. (2.12) is used to obtain a better approximation for T_1. Once this is completed, this whole process can be repeated from Eq. (2.2) using the new value obtained here for T_1 and it should be iterated until the values converge. Once each state properties have converged, the final characteristics of this engine configuration can be calculated in order to conclude the preliminary Otto cycle analysis.

Now that all the state parameters have been obtained, it is possible to obtain the work output during the expansion stroke as well as the heat rejected through the exhaust gases directly afterwards [9]:

$$\dot{W}_{out} = \dot{m}_{total} C_{v_{ex}} (T_3 - T_4) \tag{2.13}$$

$$\dot{Q}_{out} = \dot{m}_{total} C_{v_{ex}} (T_1 - T_4) \tag{2.14}$$

where $\dot{W}_{out}$ is the power output during the expansion stroke, $C_{v_{ex}}$ the specific heat capacity at constant volume of the burnt exhaust gases and $\dot{Q}_{out}$ is the heat expelled through the exhaust gases.

To obtain an accurate value for the indicated engine power, the power necessary to complete the compression stroke and to pump the gases in and out of the combustion chamber need to be obtained and then subtracted from the output power over the whole cycle, keeping in mind that it takes two engine revolutions to complete each cycle [9]:

$$\dot{W}_{pump} = \frac{N(P_e - P_i)V_d}{60n_r} \tag{2.15}$$

where $\dot{W}_{pump}$ is the pumping power.

$$\dot{W}_i = \dot{W}_{out} - \dot{W}_{in} - \dot{W}_{pump} \tag{2.16}$$

$$\dot{W}_i = \dot{m}_{total} C_{v_{ex}} (T_3 - T_4) - \dot{m}_{total} C_{v_{air}} (T_2 - T_1) - \frac{N(P_e - P_i)V_d}{60n_r} \tag{2.17}$$

Next, in order to accurately compare the engine's theoretical performance improvements achieved due to exhaust thermal energy recovery, the indicated mean effective pressure (*imep*), the indicated specific fuel consumption (*isfc*) and the thermal efficiency (η_{th}) of the current setup need to be calculated at this stage in order to be used later on as the baseline values for comparative purposes [9].

$$imep = \frac{\dot{W}_i n_R}{V_d N} \tag{2.18}$$

$$isfc = \frac{\dot{m}_f}{\dot{W}_i} \tag{2.19}$$

$$\eta_{th} = \frac{\dot{W}_i}{\dot{Q}_{in}} \tag{2.20}$$

All the state properties parameters obtained following the theoretical Otto cycle analysis as well as engine speed specific values can be viewed in Table A.1 and Table A.2 located in Appendix A. It should be noted here that the selection of engine speeds used for the analysis are based on the speeds at which the experimental engine is stable enough to run tests at.

2.2.2 Peak Physical Thermal Recovery

Following the Otto cycle analysis, the next step in the preliminary energy recovery study is to assess the maximum thermal energy that can physically be transferred from the exhaust gases into the water circuit via the heat exchanger. From the previous analysis, it was determined that the maximum theoretical heat rejection out of this cycle, at 6000 RPM is 44.89 kW. It is interesting to note here that even by assuming that only 5% of this thermal energy can be recuperated, an increase in thermal efficiency of about 4.7% would therefore be feasible.

In order to correctly approximate the heat absorption potential of this system, the log mean temperature difference (LMTD) method shall be applied in order to obtain the physical heat transfer limits. This method in particular was determined to be ideal for the present analysis and was therefore chosen thanks to its vast inclusiveness of multiple parameters used in obtaining a solution, thus allowing for the observation of their individual contributions to the heat transfer process. Furthermore, the use of additional terms also allows for extra precision in the theoretical assessment. It should be noted here that this method was selected instead of the effectiveness-NTU (the number of transfer units) methods due to the particularities of the current design and its limitations [11]. Although the layout and size of the heat exchanger to be used are partially fixed due to space (i.e., engine and dyno configuration), resources and design manufacturability constraints, the mass flow rate and outlet temperature of the water circuit remain as variables to be solved for. As it will be demonstrated in the equations that follow, any variation in the previously stated parameters will in turn influence the temperature of the exhaust tube's wall contained in the section of the custom heat exchangers, thus influencing the downstream exhaust gas temperatures and therefore the maximum heat transfer physically achievable via this setup.

As previously stated, the physical dimensions of the heat exchanger need to be fixed in order to simplify the heat exchange calculations. Due to limitations on the materials that were economically feasible to be used for the current extreme high temperature and corrosiveness application, 304 stainless steel was selected as the material of choice for the manufacturing of the custom exhaust runner/boiler component. Furthermore, a limitation on the possible length of these units was imposed by the current setup of the experimental engine onto the dyno. In order to provide a visual reference, an example of the exhaust heat exchangers used to complete the following calculations is shown below in Figure 2.2.

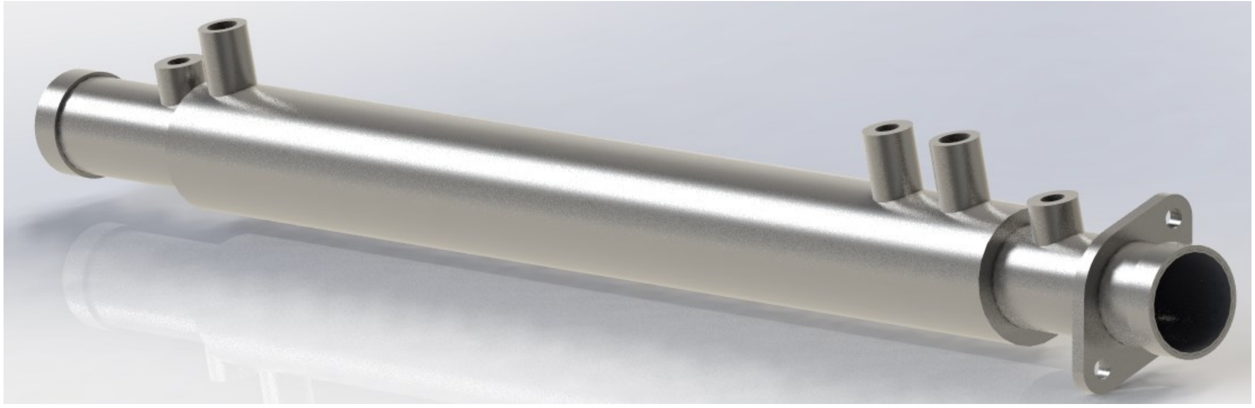

Figure 2.2 Isometric View of Exhaust Heat Exchanger

Below is a detailed cross-sectional longitudinal and axial view of the heat exchanger which details the flow directions and the separate compartments through which the exhaust gases and the water flow through. The directions of the flows have been selected to be opposite due to the fact that counter-flow double-pipe heat exchanger configuration yield higher variations in temperatures of the working mediums [11]. It should be noted that the end caps were removed from the axial cross-sectional view in order to demonstrate the presence of the fins in the water jacket and whose impact on both heat transfer improvements and pressure loss will be briefly assessed later on.

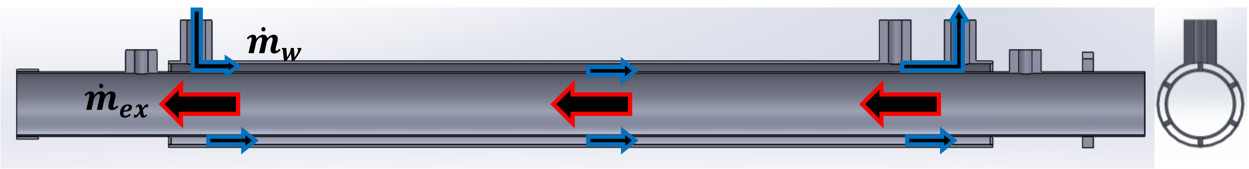

Figure 2.3 Longitudinal and Axial Cross-sectional Views of Heat Exchanger

2.2.2.1 *Determining the Exhaust Gas Convection Heat Transfer Coefficient*

Now that the flow directions and overall configuration of the exhaust heat exchangers have clearly been detailed, the theoretical heat recovery analysis can begin. The first step will be to obtain the velocity of exhaust gases as they flow through the runners. This will be done by using the total mass flow rate through the combustion chamber, which has previously been obtained in the Otto cycle analysis, as well as the density of the burnt gases and the cross-sectional area of the runners [11].

Since

$$\dot{m}_{ex} = \rho A V_{ex} \tag{2.21}$$

Therefore

$$V_{ex} = \frac{\dot{m}_{ex}}{\rho A} \tag{2.22}$$

This obtained velocity for the exhaust gases shall be considered as the lower bound of the velocity spectrum of which the upper bound shall be determined in the following section. For the present moment, this lower velocity shall be used so that the Reynolds number can now be obtained [12]:

$$\mathrm{Re} = \frac{V_{ex} D}{\nu} \tag{2.23}$$

where Re is the Reynolds number, V_{ex} the exhaust gas velocity, D the pipe diameter and ν the kinematic viscosity of the gas. Since the calculated Reynolds number is above 4000 throughout the engine's operating speed range, the flow is considered as being turbulent [12].

The tubes used for the construction of the exhaust system have a ground finish and will therefore be assumed as being smooth for the purpose of friction factor calculations.

From the explicit first Petukhov equation [11]:

Since $3000 < \mathrm{Re} < 5 \cdot 10^6$

$$f = (0.790\, ln\, \mathrm{Re} - 1.64)^{-2} \tag{2.24}$$

where *f* is the friction factor in turbulent flow.

Next, the Nusselt number is to be determined in order to proceed in obtaining the convection heat transfer coefficient necessary in the LMTD method.

Since $0.5 \leq \mathrm{Pr} \leq 2000$ & $3000 < \mathrm{Re} < 5 \cdot 10^6$

$$\mathrm{Nu} = \frac{\frac{f}{8}(\mathrm{Re}-1000)\,\mathrm{Pr}}{1+12.7\left(\frac{f}{8}\right)^{0.5}\left(\mathrm{Pr}^{\frac{2}{3}}-1\right)} \tag{2.25}$$

where Nu is the Nusselt number, Pr the Prandtl number and *f* the friction factor.

From here, obtaining the convection heat transfer coefficient is straightforward [11]:

$$\mathrm{Nu} = \frac{h_i D_i}{k_{ex}} \tag{2.26}$$

where h_i is the convection heat transfer coefficient of the exhaust gas, D_i the internal diameter of the runner and k_{ex} the gas's thermal conductivity.

The convection heat transfer coefficients obtained in this section range from 17.94 to 57.02 $\frac{\mathrm{W}}{\mathrm{m}^2\cdot\mathrm{K}}$ as seen in Table A.5 located in Appendix A.

2.2.2.2 Heat Exchanger Upper Bound Exhaust Gas Velocity Calculation

Prior to solving for the maximum theoretical heat exchange that can occur through the tube walls, an additional parameter needs to be obtained, namely, the upper bound velocity of the exhaust gases as they enter the heat exchanger section.

From ratio of the downstream exhaust system pressure (P_e) to the stagnation pressure calculated in the Otto cycle's exhaust stroke (P_4), it will be determined if the flow is choked at the valves by verifying if this ratio is smaller than the critical pressure ratio of 0.5457 as obtained in the isentropic flow tables for $\gamma = 1.3$ [13]:

Since

$$\frac{P_e}{P_4} < \frac{P^*}{P_o} \tag{2.27}$$

Therefore the flow is choked at the exhaust valves and the isentropic flow relations are to be used with the assumption that the flow area at the valves is the critical area where $M = 1$.

Next, the flow area out of the exhaust ports needs to be calculated. This flow area is obtained by calculating the curtain area of the valve at maximum lift, as specified in the engine's service manual [8], and multiplying it by a corresponding discharge coefficient [9]:

$$A_f = 2(\pi D_v L)C_d \tag{2.28}$$

where A_f is the curtain area, D_v the exhaust valve diameter, L represents the maximum exhaust valves lift as measured on the exhaust camshaft lobes and C_d represents the discharge coefficient obtained from Annand and Roe [9] using the current L/D_v ratio. The equation is multiplied by 2 since there two exhaust valves per cylinder. All values are recorded in Table A.4 of Appendix A.

Finally, by calculating the runner's cross-sectional area and dividing it by the choked area, an area ratio will be obtained and through the use of the isentropic flow tables for $\gamma = 1.3$ [13], the Mach number of the flow and therefore the upper bound velocity of the exhaust gases as they enter the heat exchanger (V_{ex}) can be obtained.

$$\frac{A_{ex}}{A^*} = 2.142 \tag{2.29}$$

which represents $M = 0.288$.

In the previous section, the lower bound of the exhaust gas velocity was obtained using Eq. (2.22) and the engine's average mass flow rate at a given speed. Now that the Mach number of the flow has been determined, the upper bound value of the gas velocity can be obtained [13]:

$$V_{ex} = M_{ex}\sqrt{\gamma R T_{ex}} \tag{2.30}$$

From here, Eq. (2.23) to Eq. (2.26) can be repeated using this higher value for the exhaust gas velocity in order to obtain an upper bound value for the convection heat transfer coefficient of the exhaust gas, which in this case is calculated as 223.7 $\frac{\mathrm{W}}{\mathrm{m^2 \cdot K}}$. All other values have been calculated and are displayed in Table A.9 located in Appendix A.

2.2.2.3 Using the LMTD Method

Now that all the parameters, needing separate calculations, required for the application of the LMTD method have been obtained, this method can finally be applied in order to yield the maximum heat physically recoverable. Ultimately, the equation which will be used is [11]:

$$\dot{Q}_{out} = h_i A_s \Delta T_{lm} \tag{2.31}$$

where $\dot{Q}_{out}$ is the sought after heat transferred through the pipe walls, h_i is the average convection heat transfer coefficient of the exhaust gas, A_s the heat transfer surface area and ΔT_{lm} the log mean temperature difference.

The heat transfer surface area is obtained through:

$$A_s = \pi D_i L \tag{2.32}$$

where D_i is the inner diameter of the exhaust tube and L is its length in the heat exchanger section.

The last term in Eq. (2.31) that needs to be defined is the ΔT_{lm} term. The equation used to find this term is as follows [11]:

$$\Delta T_{lm} = \frac{T_i - T_e}{ln\left(\frac{T_s - T_e}{T_s - T_i}\right)} \tag{2.33}$$

where T_i, T_e and T_s respectively represent the inlet and outlet gas temperatures through the exchanger and finally the surface temperature of the tubes.

Now in order to find a value for the outlet gas temperature, the equation below needs to be used [11]. One will note that every variable in the present equation has been previously determined except for the surface temperature, this is where the iterative process begins. An initial approximation for the temperature of the exhaust tubes must be made here in order to proceed.

$$T_e = T_s - (T_s - T_i) e^{\frac{-h_i A_s}{\dot{m}_{ex} c_p}} \tag{2.34}$$

Next, Eq. (2.31) can be used in order to evaluate the magnitude of the heat transferred out of the exhaust gases given the current assumed surface temperature of the heat exchanger. In order to validate that the assumed value is accurate enough, the process has to be completed in reverse for the water in the annular volume. Finally, both sides of the exchanger will be held energetically balanced and will need to converge to an identical surface temperature. Heat dissipated from the exhaust gases range from 2.321 to 6.522 kW. All values have been calculated and displayed in Appendix A, Table A.3 contains the constant values and Table A.5 and Table A.9 have the engine speed dependant variables.

2.2.2.4 Heat Transfer into the Water Circuit

Determining the magnitude of heat extracted from the exhaust gases is only one side of the energy balance in this heat exchanger. The next step is to carefully determine the variables on the water side in order to zero in on the theoretical energy recovered via this setup.

First, due to the very high thermal conductivity of the 304 stainless steel, it will be assumed here that all the energy out from the gases as calculated in the previous section is flowing into the water and therefore:

$$\dot{Q}_{out} = \dot{Q}_{in} \tag{2.35}$$

From here Eq. (2.31) is reformatted with new subscripts to reflect the parameters in the annular space.

$$\dot{Q}_{in} = h_o A_s \Delta T_{lm} \tag{2.36}$$

Initial attention will be given to the ΔT_{lm} term. As it will be detailed in the following sections, the higher the inlet temperature into the steam turbine, the more power it can produce and therefore in order to limit the amounts of variables involved in the iterative process, the outlet temperature of the boiler section will be assumed to be 5°C less than the surface temperature and therefore:

$$T_e = T_s - 5 \tag{2.37}$$

Here Eq. (2.33) can easily be solved for ΔT_{lm} on the water circuit side since the inlet water temperature will be assumed as being held constant at the engine's operating temperature, namely 85°C. This will be done by means of recovering the required thermal energy from the engine's cooling system via the Kalina cycle which will be detailed in the following section.

The next step is to obtain the initial value of the average convection heat transfer coefficient in the water circuit using Eq. (2.31). The heat transfer surface area used for the water side is taken from the CAD model shown in Figure 2.2. Due to the high thermal conductivity of the steel, the entire inner shell surface (exhaust runner wall) as well as the fins exposed to the water are assumed to be at the indicated surface temperature specified during each iteration and therefore it is assumed to be the transfer surface area for the purpose of this study. Finally, the outer shell surface is considered as being adiabatic and its area will be neglected.

From Eq. (2.31):

$$h_o = \frac{\dot{Q}_{in}}{A_s \Delta T_{lm}} \tag{2.38}$$

Now that all parameters have been identified on the water side, it is possible, using Eq. (2.34) to solve for the water mass flow rate required to maintain continuity in the equations. Therefore

$$\dot{m}_w = \frac{-h_o A_s}{C_p \ln\left(\frac{T_s - T_e}{T_s - T_i}\right)} \tag{2.39}$$

From here, a separate thermal analysis shall be performed in order to obtain an actual value for the average convection heat transfer coefficient now that the order of magnitude for the water mass flow rate has been identified.

This separate thermal analysis will start by taking the water mass flow rate determined above in order to obtain its velocity using Eq. (2.21).

$$V_w = \frac{\dot{m}_w}{\rho \pi \frac{D_h^2}{4}} \tag{2.40}$$

where D_h is defined as the hydraulic diameter calculated by subtracting the outer shell diameter from the inner one [11].

Next, using Eq. (2.23), the Reynolds number is obtained using the above stated hydraulic diameter in the equation. Since Reynolds number obtained here is of the order of 10^2, the flow is considered laminar and therefore the thermal entrance region is determined as follows [11]:

$$L_{t,laminar} \approx 0.05 \text{ Re Pr } D_h \tag{2.41}$$

Since the thermal entrance is less than 10% of the length of the heat exchanger throughout the range of Reynolds numbers obtained during the iterations, the flow is considered as being fully developed and laminar. The Nusselt number can therefore be taken directly from the relation developed by Kays and Perkins [11] for this type of annular configuration and given the current of the inner to outer diameter ratio, it is determined to be held constant at 4.92. Therefore using Eq. (2.26) the average convection heat transfer coefficient can be determined.

$$h_o = \frac{k_w \text{Nu}}{D_h} \tag{2.42}$$

The whole process in obtaining this final value from the beginning has been summarized in Figure 2.4 for simplicity and the constants have been displayed in Table A.3 of Appendix A.

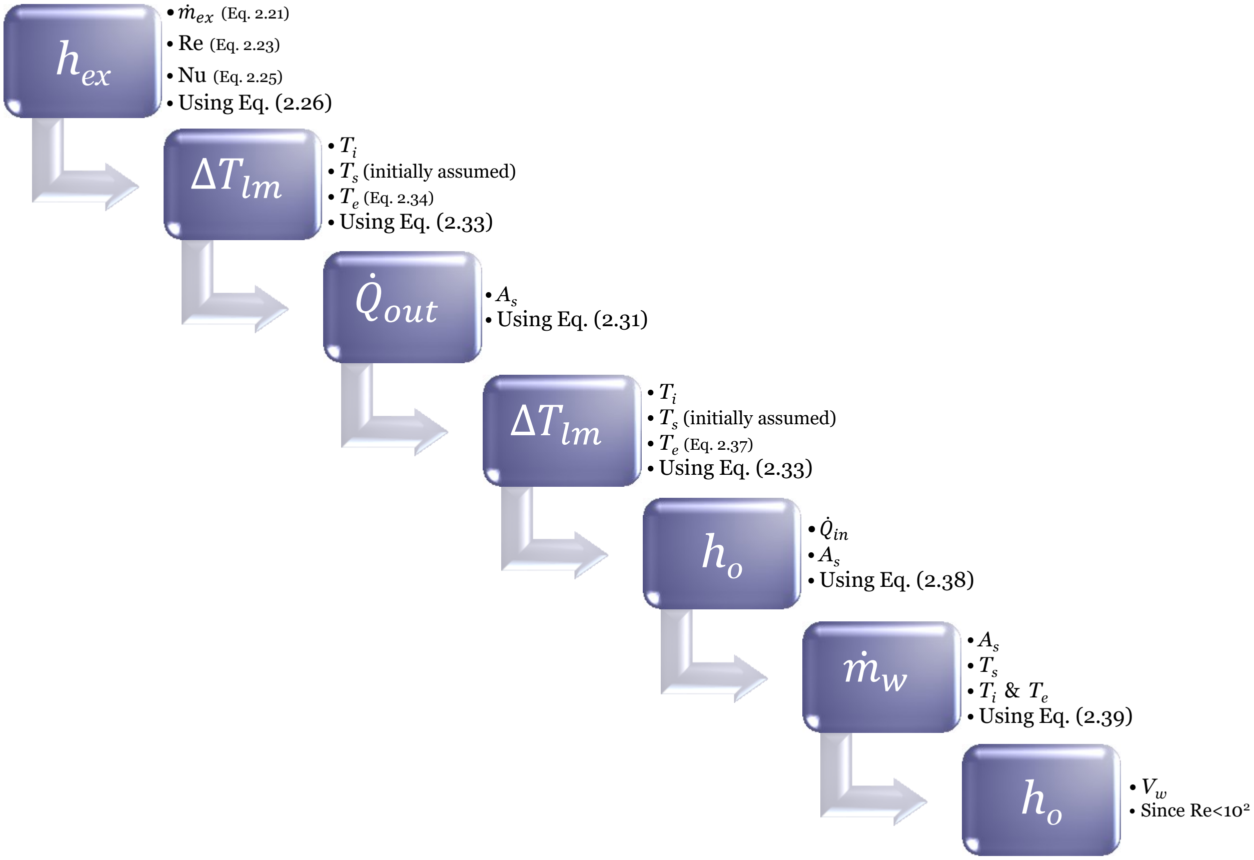

Figure 2.4 Heat Analysis Process Chart

Now taking a closer look at Eq. (2.31), it can be noticed that all terms have been independently solved for and in order for the energy balance to hold true, one of the terms needs to be changed. Now since the heat transfer surface area is a design constant in this case and that the average convection heat transfer coefficient is constant given the range of flow rates in this study, the only term that remains as a variable here is the log mean temperature difference (ΔT_{lm}). By observing this term's definition through Eq. (2.33) and recalling that it was stated that the outlet temperature of the water would be a direct function of the surface temperature and that the inlet temperature would be held constant, it is obvious here that the ultimate term left to solve for, in order to complete the peak physical thermal recovery analysis, is the surface temperature.

This is where the iterative process happens in order to complete this section. As it was stated above, the surface temperature used initially was simply an initial approximation. It would seem that all that is left to do is solve for this final term since all other parameters have been independently solved for, yet it should be noted that as the surface temperature is varied so is the magnitude of the heat transferred through the walls and therefore the whole analysis has to be repeated until this final value converges to a proper theoretical value. The process used to complete this analysis will be initiated by first assuming a value for the surface temperature and then using Eq. (2.31) to find the heat output from the exhaust gases and therefore input into the water. From here, using Eq. (2.31) once again, yet on the water side, the new log mean temperature difference will be determined. Next using Eq. (2.33), the log mean temperature difference is independently calculated in order to confirm that these values have converged, if not, the log mean temperature difference obtained from Eq. (2.36) on the water side is then used in Eq. (2.33) to solve for the new surface temperature term to be used and the process is iterated until convergence is obtained. Ultimately the surface temperatures obtained range from 522 to 765K for the lower bound values and from 850 to 980K for the upper bound values. The whole process is displayed in flow chart form in Figure 2.5 and the complete results have been presented in Table A.6 and Table A.10 of Appendix A.

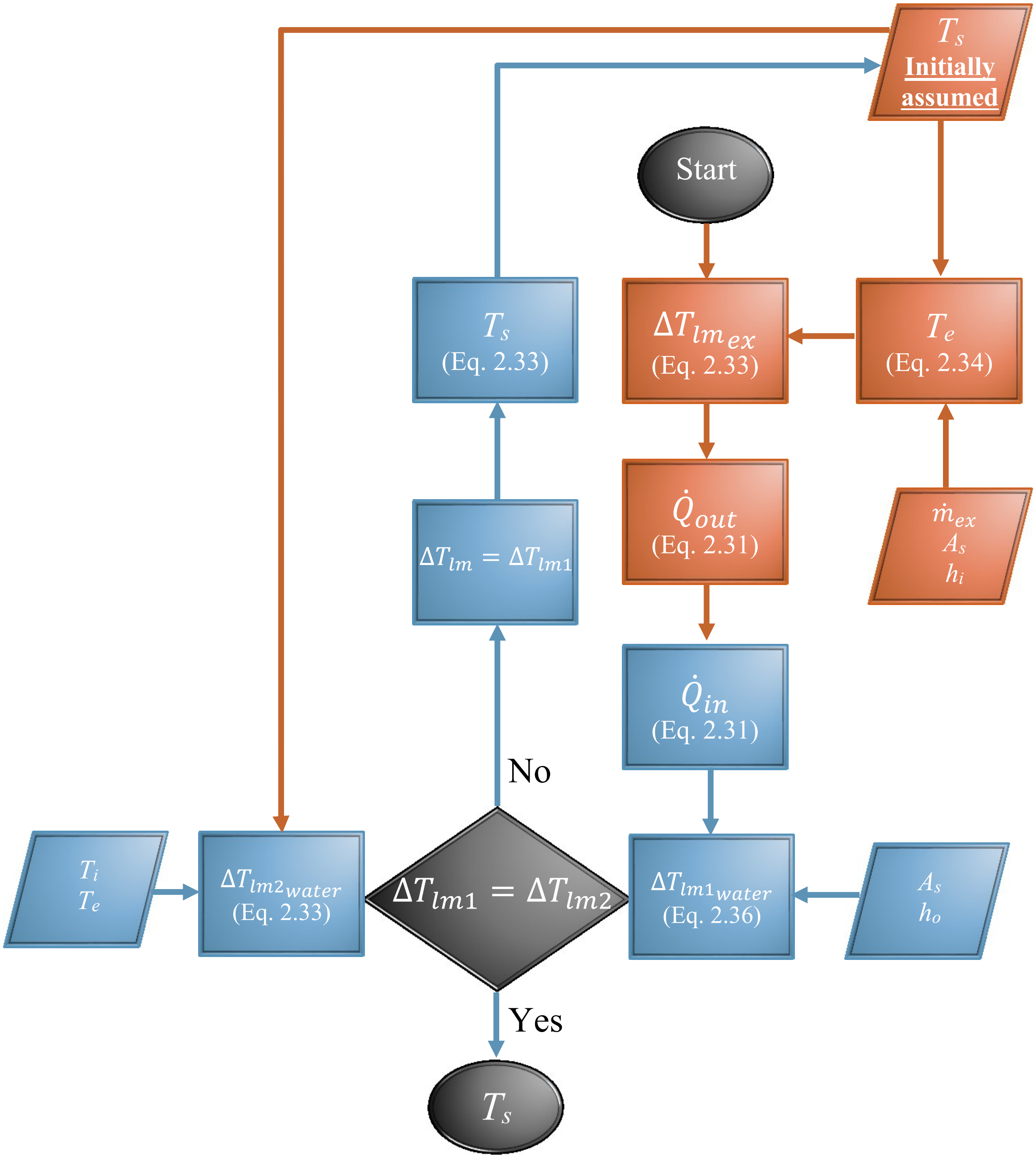

Figure 2.5 Heat Transfer Iterative Process Flow Chart

2.2.3 Minimum Water Heat Flux Capacity

In order to further confirm the feasibility of this theory, it should be verified that the water flowing through the annular area can physically absorb all this energy or if this heat flux is beyond its physical limitations. In order to be conservative, the equation yielding the minimum heat flux capacity of the water shall be utilized [11].

$$\dot{q}_{max} = 0.09\rho_v h_{fg}\left[\frac{\sigma g(\rho_l - \rho_v)}{(\rho_l + \rho_v)^2}\right]^{0.25} \tag{2.43}$$

where $\dot{q}_{max}$ is the conservative maximum heat flux the water can absorb, h_{fg} the enthalpy of vaporization, σ the surface tension of the liquid-vapor interface, g the gravitational acceleration constant, ρ_v and ρ_l are vapor and liquid densities respectively.

$$\dot{Q}_{in} \leq \dot{q}_{max} A_s \tag{2.44}$$

Since the maximum heat flux into the water from the previous thermal analysis is below the water's lower bound limit on heat flux absorption capability, of 8.413 kW, it is therefore assumed that there will be no foreseen physical heat absorption limitations imposed by the working fluid undergoing its phase change.

2.2.4 Rankine Cycle Analysis

To correctly conclude the preliminary assessment of the impact of this energy recovery on the system as a whole, a full analysis of the Rankine cycle has to be performed. This will be done by taking the previously calculated energy recovered in the heat exchanger-boiler and imposing this input into a modified Rankine circuit, as seen in Figure 2.6, which will be coupled to a Kalina cycle in order to extract as much energy out of the waste heat from the engine as possible.

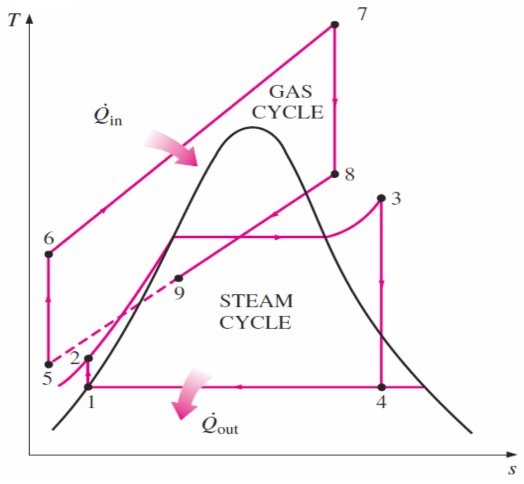

Figure 2.6 Combined Otto-Rankine Cycle [10]

The analysis will go as follows: first the pressure ratio of the system will be imposed by the performance limitations of the experimental water pump used in this research. Next, the amount of energy transferred into the water will be applied in two stages, the first of which will be by means of the Kalina cycle in order to raise the temperature of the water from saturated liquid to the engine cooling system's operating temperature of 85°C. The second stage will be to introduce the energy recovered from the exhaust gases to the cycle. Finally, the peak power theoretically recoverable by the steam turbine will be calculated.

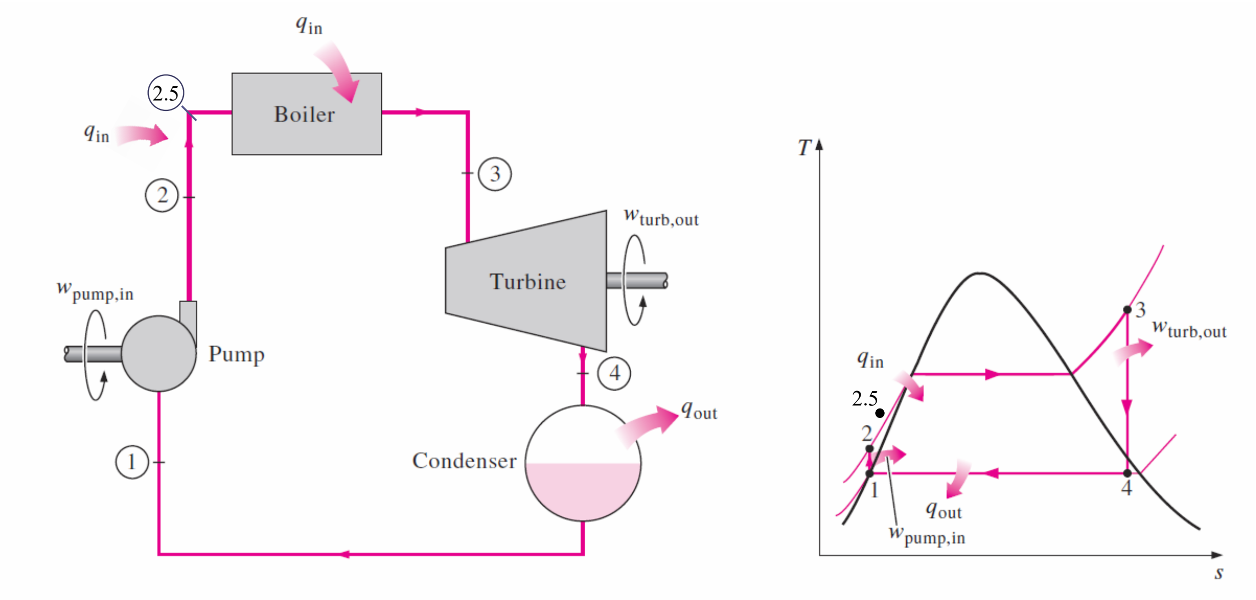

Figure 2.7 Ideal Modified Rankine Cycle and its *T-S* Diagram [10]

The analysis will start here by initially using the water mass flow rate calculated in the prior section as an initial parameter. Here the pressures have been arbitrarily selected from the experimental pump's pressure capability and typical pressures found in steam condensers [10]. This example displayed here will be completed using the lower bound theoretical values obtained from the previous section at 2475 RPM, the complete range of theoretically calculated values obtained using the lower and upper boundaries can be seen in Table A.7 and Table A.11 respectively, of Appendix A.

The first step in the cycle analysis will be to determine from the thermodynamic tables the enthalpy of the saturated water coming from the condenser which will be identified as state 1 [10]. The water mass flow rate previously calculated shall be used as an initial assumption.

State 1: $T_1 = 333.1$ K & $P_1 = 20$ kPa $\rightarrow h_1 = 251.2\,\frac{\text{kJ}}{\text{kg}}$

Next the water will be pressurized as it passes through the pump and the enthalpy of the water will be determined at that point. Here the power consumed by the pump will be calculated by assuming it having an efficiency of 0.65, a value which is typically found for pumps in Rankine cycles [14] [15].

State 2: $T_2 = 333.1$ K & $P_2 = 800$ kPa $\rightarrow h_2 = 251.8\,\frac{\text{kJ}}{\text{kg}}$

$$\dot{W}_p = \frac{Q_w(P_2 - P_1)}{\eta_p} \tag{2.45}$$

where $\dot{W}_p$ is the power consumed by the pump, Q_w the volume flow rate, P_1 and P_2 are the water pressures before and after the pump respectively.

As it can be seen in Figure 2.7, there is a state 2.5 which in this case corresponds to the heat input from the Kalina cycle. This heat is absorbed from the engine's cooling system and is therefore used to raise the water temperature up to the engine's operating temperature. A separate heat analysis could be made here to detail the nature of this exchange, but suffice to say that this exchange is straight forward and its detailed analysis will be limited to specifying the magnitude of heat recovered in order to bring the water from state 2 to 2.5.

State 2.5:

$$\dot{Q}_{Kalina} = \dot{m}_w(h_{2.5} - h_2) \tag{2.46}$$

$T_{2.5}$ = 358.2 K & $P_{2.5}$ = 800 kPa $\rightarrow h_{2.5} = 356.5\,\frac{\text{kJ}}{\text{kg}}$

Next, the preheated water will pass through the boilers and the lower bound energy recovered from the previous section at 2475 RPM will be used in this heat addition step.

State 3:

$$\dot{Q}_{in} = \dot{m}_w(h_3 - h_{2.5}) \tag{2.47}$$

$$\therefore\ h_3 = \frac{\dot{Q}_{in}}{\dot{m}_w} + h_{2.5} \tag{2.48}$$

$h_3 = 2936\,\frac{\text{kJ}}{\text{kg}}$ → T_3 = 517.2 K & P_3 = 800 kPa

Finally, the turbine power output can be obtained by initially assuming an isentropic turbine and determining the specific entropy at state 3 and setting it equal to that of state 4. From there, it can be assumed that the turbine has an isentropic efficiency of 0.7, typical for expanders under these conditions [14] [15], and the enthalpy of state 4 can be obtained, therefore the corresponding temperature at the condenser inlet can be determined since its pressure is known.

State 4:

Initially assuming isentropic turbine:

T_3 = 517.2 K & P_3 = 800 kPa $\rightarrow h_3 = 2936\,\frac{\text{kJ}}{\text{kg}}$ & $s_3 = 7.01\,\frac{\text{kJ}}{\text{kg·K}}$

$s_4 = s_3$ & P_4 = 20 kPa $\rightarrow h_{4_s} = 2311\,\frac{\text{kJ}}{\text{kg}}$

$$\dot{W}_t = \eta_t \dot{m}_w\left(h_{4_s} - h_3\right) \tag{2.49}$$

Therefore

$$\dot{Q}_{out} = \dot{m}_w(h_4 - h_1) \tag{2.50}$$

The last step necessary here prior to concluding this section with the improvements achievable is to define the energy recovered by including all the terms in order to obtain an inclusive and realistic model. This is done by subtracting the real pump work from the actual turbine work and including the losses in transmission and power generation. Assuming that the turbine here is coupled to a generator and using an efficiency value of 0.9, a typical value for generators [15]:

$$\dot{W}_r = \eta_g \left(\eta_t \dot{W}_t - \frac{\dot{W}_p}{\eta_p} \right) \tag{2.51}$$

where $\dot{W}_r$ is the final energy recovered from the Otto cycle via the Rankine cycle and η_g the generator efficiency.

Following the calculation of the maximum theoretical turbine energy output, the potential decrease in specific fuel consumption and increase in efficiency of this combined Otto-Rankine cycle can be determined using Eq. (2.19) and (2.20) respectively, both modified to include the power generated recovered by the Rankine cycle.

$$isfc = \frac{\dot{m}_f}{(\dot{W}_i + \dot{W}_r)} \tag{2.52}$$

$$\eta_{th} = \frac{(\dot{W}_i + \dot{W}_r)}{\dot{Q}_{in}} \tag{2.53}$$

This final calculation of the preliminary heat analysis ultimately proves that given the current engine operating conditions and configuration, it is therefore possible to recover anywhere from 2.321 up to 6.522 kW from the engine's exhaust gases. This energy can in turn be used to drive a steam turbine which could theoretically produce between 0.3939 to 1.526 kW which would otherwise be lost out the tailpipe. The turbine's shaft power output boundaries, which include efficiency losses, are displayed in Figure 2.8. This hypothetical energy recovery would ultimately result in a 5.131% reduction in indicated specific fuel consumption and an increase in thermal efficiency of 5.408% near the 2500 RPM range. The variation in these improvements with respect to engine speed can be observed in Figure 2.9. A comprehensive data set can be seen in Table A.5 to Table A.12 of Appendix A.

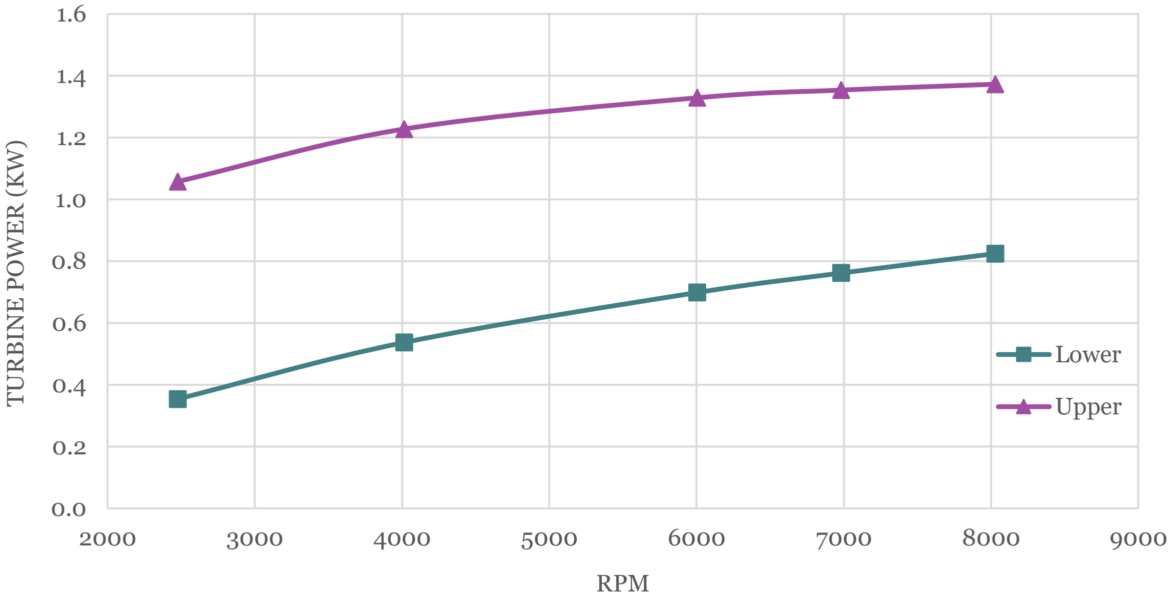

Figure 2.8 Turbine Upper and Lower Bound Theoretical Shaft Power

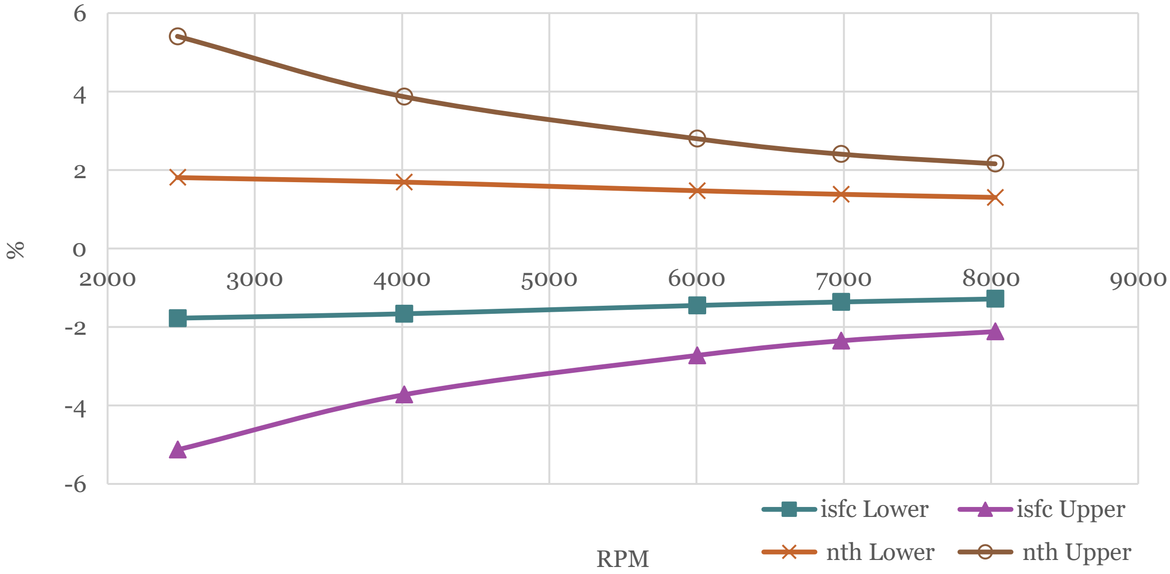

Figure 2.9 Theoretical Upper and Lower Bound Improvements in *isfc* and η_{th}

2.3 Heat Rejection Optimization

As previously stated, the effect of the addition of fins in the annular volume shall be studied in this section in order to understand their contribution to the heat transfer process. As it can be observed in Eq. (2.36), increasing the surface area available for heat transfer could result in greater heat absorption capabilities into the water circuit. The efficiency of such fins will be determined here along with the effect an increased surface area in the water circuit has on the system as a whole.

2.3.1 Baseline - No Fins

Here, the surface area considered for the heat transfer shall simply be the outer side of the exhaust gas tube enclosed within the boiler section including the end caps as they will be considered as being held constantly at the runner wall temperature. Using this stated surface area, which corresponds here to 0.05915 m^2 per heat exchanger runner, the baseline energy recovered by this system is obtained by using the complete procedure described in Section 2.2 and is given to be 2.180 kW at the lower bound value for 2475 RPM.

2.3.2 Fin Addition Effect

Next, the improvements achieved via the addition of fins in the annular space will be obtained and compared to the baseline value in order to give an idea as to the magnitude of the achievable improvements.

When adding fins, it is important to determine their efficiency prior to including the added surface area in the heat equation. This is done as follows for straight rectangular fins, as is currently the case [11]:

$$\eta_{fin} = \frac{\tanh mL_c}{mL_c} \tag{2.54}$$

where

$$m = \sqrt{\frac{2h}{kt}} \tag{2.55}$$

$$L_c = L + t/2 \tag{2.56}$$

where h is the average convection heat transfer coefficient previously obtained for the water side and k the thermal conductivity of 304 stainless steel, which is taken to be 19.8 W/m·K given the operational temperature range of the water. The dimensions referred to in above equations are detailed in Figure 2.10 which displays the design used for the purpose of this research. The limitation on the amount of fins that could be used was imposed by manufacturability constraints.

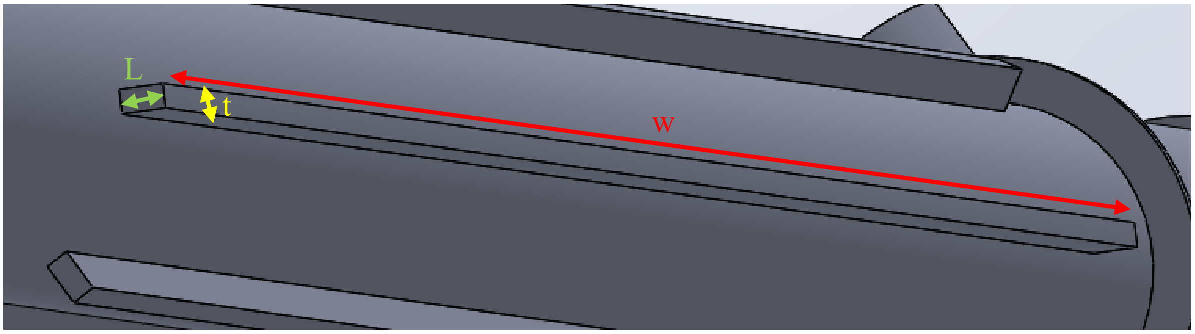

Figure 2.10 Fin Dimensional Representation

Finally, the effect of adding the fins can be assessed noting that there are six fins identical to the one depicted in Figure 2.10. The surface area used in this case will be:

$$A_t = \pi D_i L_t + 2\frac{\pi}{4}(D_o^2 - D_i^2) - 6wt + 6\eta_{fin}A_{fin} \tag{2.57}$$

where

$$A_{fin} = 2wL_c \tag{2.58}$$

A_t is the total surface area, L_t the total shell length, D_i and D_o are the inner and outer diameter of the shell.

Now that fin efficiency has been obtained and that the total area has been calculated taking this into consideration, the impact of this addition can be evaluated and compared to the baseline value previously obtained.

The energy recovered by the finned design was calculated as being 2.321 kW, a net improvement of 6.468%. It should be noted here that adding fins here resulted in a lower surface temperature as well as in an increased mass flow rate through the steam turbine, which is what partially contributed to the improvements in this section.

It is important to note that adding fins increases the wetted area and thus could induce unforeseen losses. A preliminary CFD analysis is seen in Appendix F on the change these added fins have on the flow.

2.4 Combined Turbocharged Otto-Rankine Cycle

In the previous section, a focus was given to energy potentially recoverable from the exhaust gases in order to drive a steam turbine to yield additional energy from the wasted products of combustion. This section will focus on recycling that energy back into the engine by means of a compressor in order to increase the engine's performances.

From the previous cycle calculations, it has been determined that the steam turbine is capable of producing between 0.3939 to 1.526 kW of shaft power under the current engine air intake properties. In this section, it will be assumed that the turbine's output shaft is coupled to a compressor which will be used to pre-compress the inlet air thus resulting in a hybrid turbocharged Otto-Rankine cycle. The impact of this addition on the engine's overall performances will be the subject of focus here.

Now instead of coupling the turbine to a generator, it is coupled to a centrifugal compressor in order to raise the inlet pressure to the cycle. The power input to the compressor is related to the turbine's shaft power as following:

$$\dot{W}_c = \eta_c \eta_m \dot{W}_t \tag{2.59}$$

where $\dot{W}_c$ is the power input to the compressor, $\dot{W}_t$ the turbine's shaft power, η_c the compressor's efficiency and η_m the mechanical transmission efficiency of the coupling system assumed as 0.8 and 0.95, respectively.

From here, the rise in intake air pressure can be obtained from the relation between the compressor power at a given mass flow rate and temperature which is defined as [16]:

$$P_r = \left(\frac{\eta_c \dot{W}_c}{\dot{m}_a C_p T_i} + 1\right)^{\frac{\gamma}{\gamma-1}} \tag{2.60}$$

where P_r is defined as the ratio of the compressor's outlet to inlet pressure, $\dot{W}_c$ the compressor's power input, $\dot{m}_a$ the engine's air intake mass flow rate, C_p the air's specific heat capacity at constant pressure, T_i the intake air temperature and γ the ratio of air's specific heats.

Now since the inlet pressure to the engine has been raised, the air's density needs to be recalculated along with the mass airflow into the engine. The change in mass flow rate directly impacts the heat input into the Otto cycle and therefore the whole thermal recovery analysis needs to be recalculated and iterated simultaneously in order to obtain final values. The process in obtaining the new engine performances under this configuration is an iterative one because as the intake pressure is raised, more air can enter the combustion chamber and therefore more fuel can be added thus resulting in higher heat addition. This extra heat addition, among other things, results in extra heat rejection, which in turn adds extra heat to the Rankine cycle and ultimately results in higher turbine power driving the compressor, thus further raising the pressure ratio and so the coupled cycles along with the heat analysis must all be iterated simultaneously. The process is detailed in Figure 2.14 and is considered as having converged once the heat output stabilizes from one iteration to the next.

Following the whole iterative process on the upper and lower boundary values, it was therefore established that by coupling the turbine to a compressor, it is possible to recover anywhere between 2.619 up to 6.341 kW from the engine's exhaust gases which would ultimately drive the compressor by means of a steam turbine. This recovered energy would allow the turbine to produce between 0.4499 to 1.470 kW seen in Figure 2.11. By carefully selecting the right compressor for this application, it would be able to produce pressure ratios ranging from 1.164 up to 1.564, which translates to boosting the inlet gasses by 16.61 to 57.13 kPa (2.409 to 8.286 psi) over atmospheric. The amount of boost available in function of engine speed and its direct effect on indicated power can be observed in Figure 2.12. This hypothetical energy recovery would ultimately result in a 3.698% reduction in indicated specific fuel consumption and an increase in thermal efficiency of 3.847% near the 2500 RPM range. The variation in these improvements with respect to engine speed can be observed in Figure 2.13. A comprehensive data set can be seen in Table B.1 to Table B.9 of Appendix B.

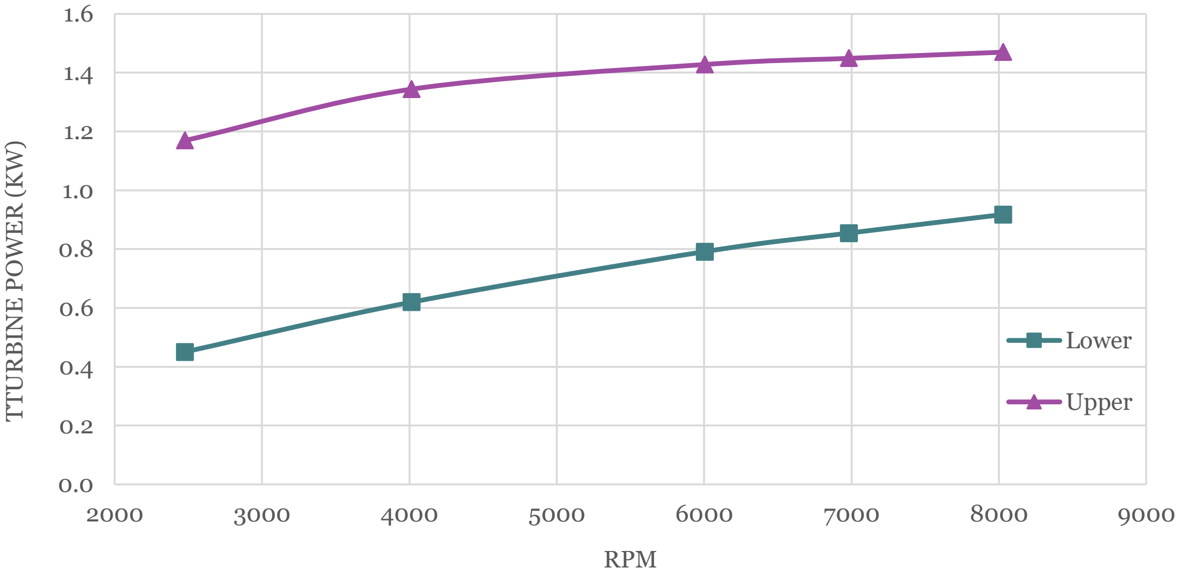

Figure 2.11 Turbine Upper and Lower Bound Theoretical Shaft Power

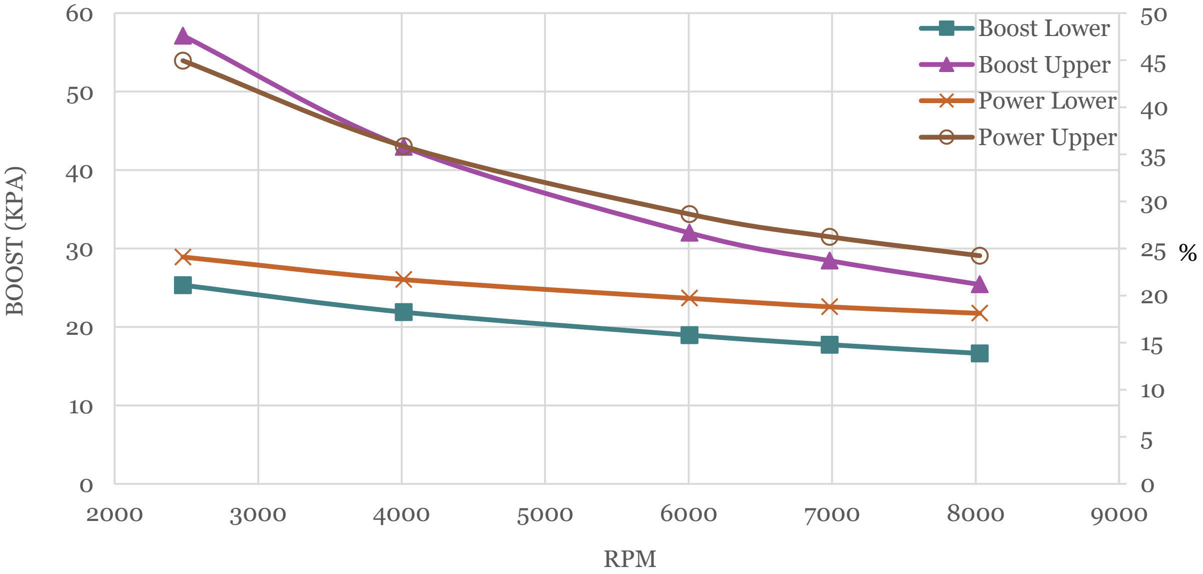

Figure 2.12 Turbo Potential Boost and Potential Indicated Power Improvements

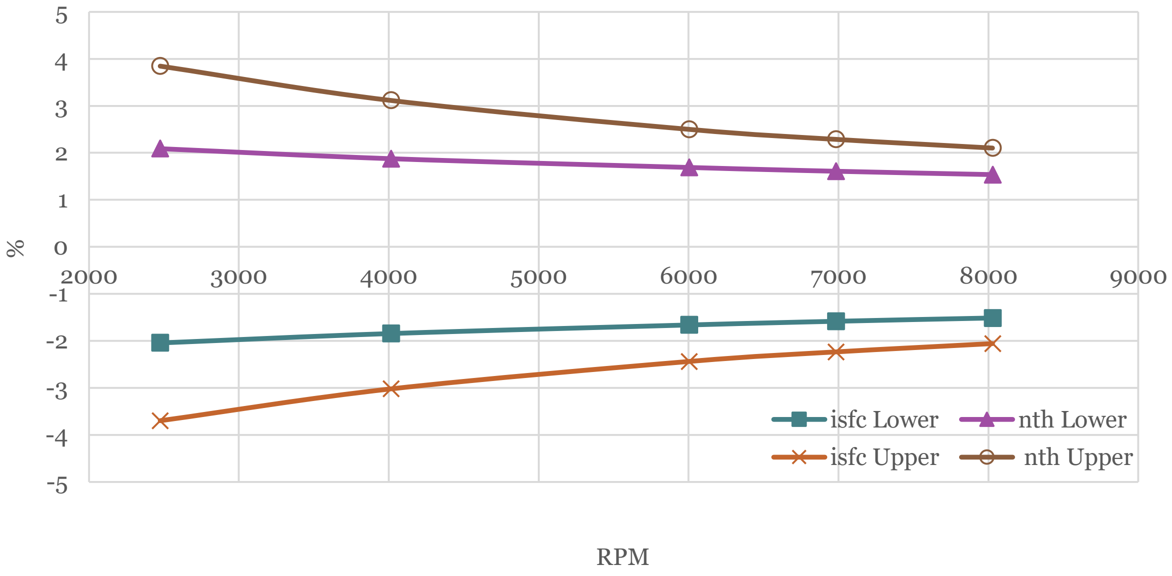

Figure 2.13 Turbo Theoretical Upper and Lower Bound Improvements in *isfc* and η_{th}

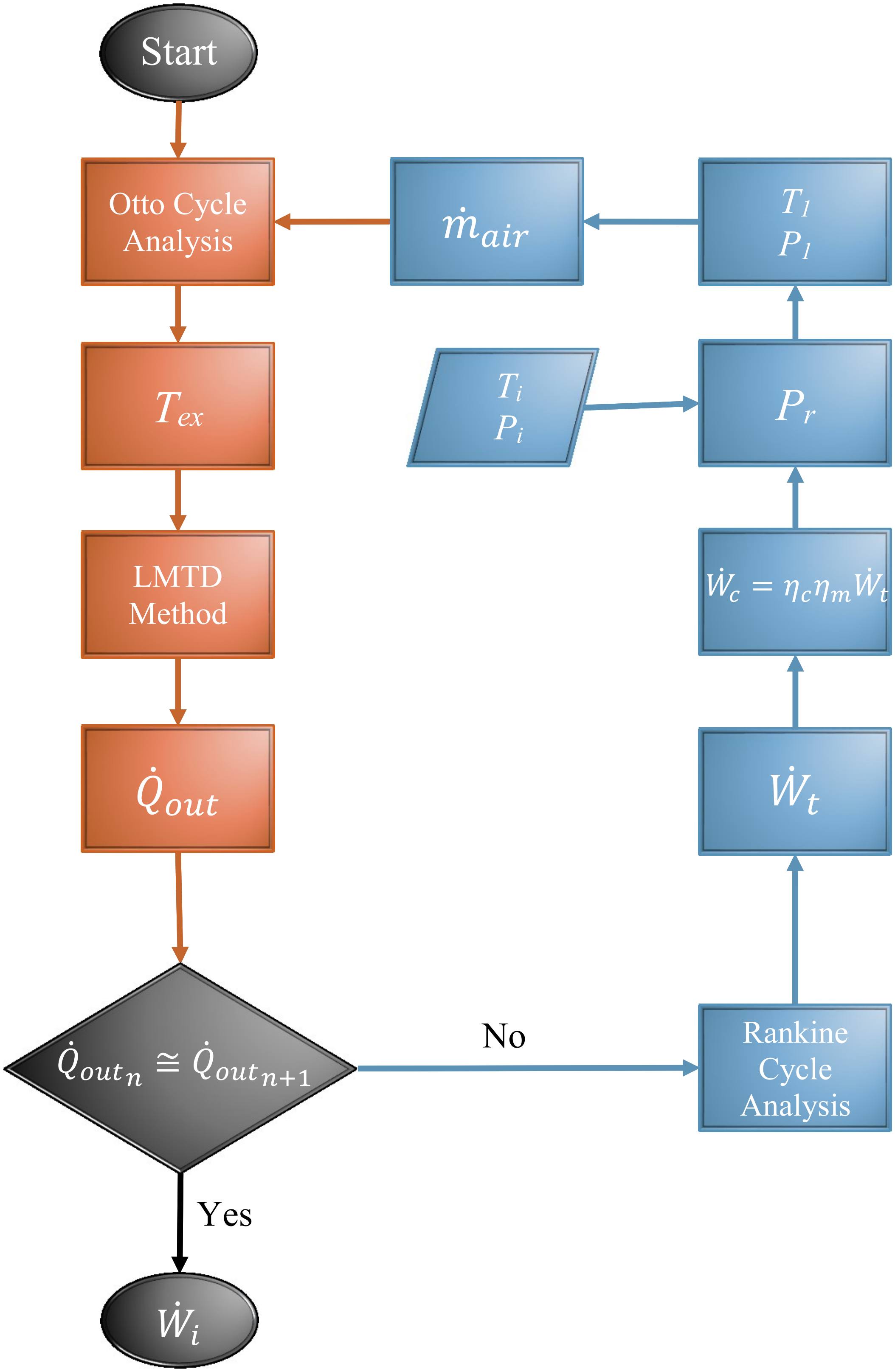

Figure 2.14 Combined Cycles Iterative Process Flow Chart

3. EXPERIMENTAL APPARATUS DESIGN AND PROCEDURES

Now that the theoretical analysis is complete and that a good understanding of the expected results has been attained, the detailed description of the experimental hardware and procedure can be done. This section will examine the design and construction of the heat exchanger boiler section and will depict its installation relative to the engine. Details on the type of instrumentation used during the experimental runs and their locations shall be supplied here as well.

3.1 Experimental Hardware and Designs

3.1.1 Heat Exchanger Design

It should be noted that the design of the exhaust boiler model as well as all other components was achieved using the SolidWorks CAD software and their technical drawings can be viewed in Appendix E. As it can be seen in Figure 3.1, the prototype consists of four independent runners each having their heat exchanging section where the boiling occurs. This isometric view details the general design of the exhaust manifolds with its mounting bracket and support. The bungs before and after the boiler sections on the exhaust runner tubes are where the thermocouples will be mounted and the ones on the heat exchanger section are the inlets and outlets of the water as well as one reserved for thermocouples. Furthermore, Figure 3.2 depicts how the prototype is mounted on the engine.

Figure 3.1 Isometric View of Exhaust Manifold

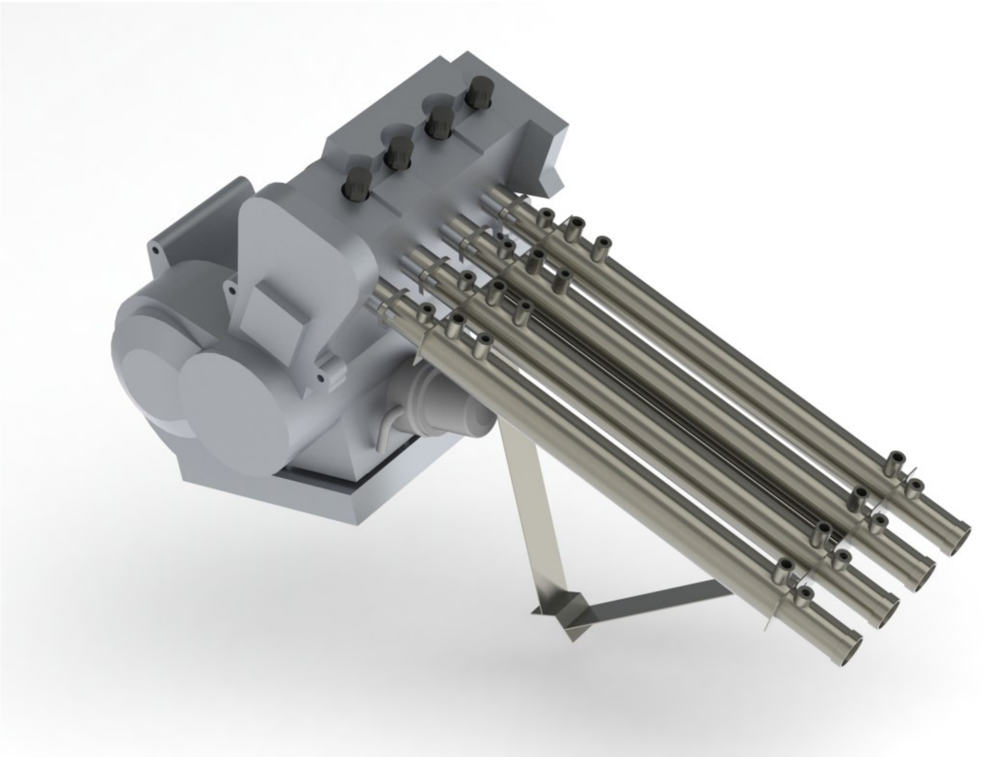

Figure 3.2 Exhaust Manifold Mounted onto Engine

3.1.2 Pump Inlet

A simple pickup was designed in order to be installed upstream of the water pump for the purpose of housing temperature and pressure sensors used to determine the water inlet temperature to the system.

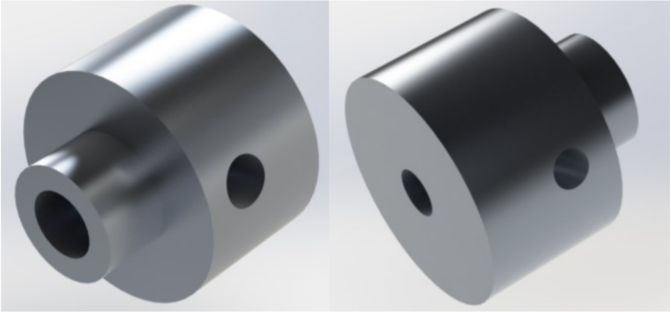

Figure 3.3 Pump Inlet

3.1.3 Feed Water Splitter

In order to distribute the water as evenly as possible between the four runners, a water splitter was designed for this task. As seen in Figure 3.4, extra holes were included in the design in order to accommodate temperature and pressure sensors for pump performance monitoring purposes.

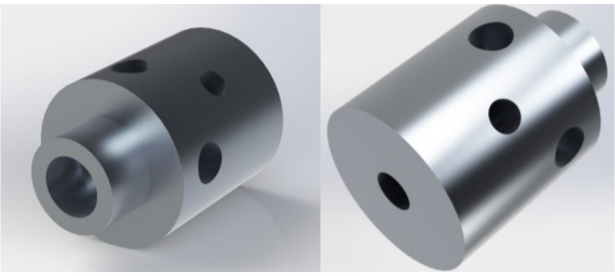

Figure 3.4 Feed Water Splitter

3.1.4 Steam Collector

A steam collector was added to the system and was specifically designed to gather the steam from all four runners in order to have a single inlet to the turbine. Temperature and pressure sensors have been mounted to this unit in order to serve as a data point for the maximum temperatures and pressures attainable via this setup. Figure 3.5 clearly depicts this component.

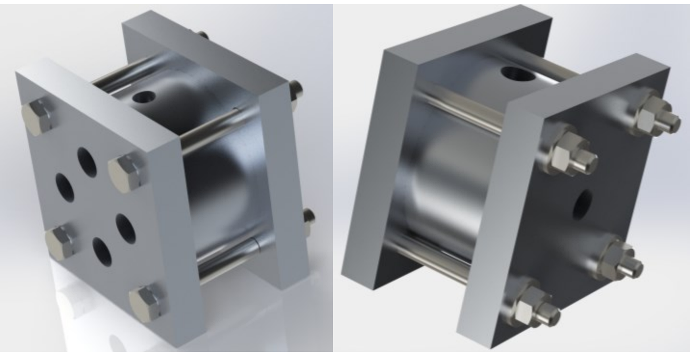

Figure 3.5 Steam Collector Assembly

3.1.5 Water Pump

The water pump used for the experiments, as seen in Figure 3.6, was a Singflo DP-160S running on 120 VAC at 0.55 amps, capable of operating at a water volume flow rate of 5.5 L/min at 1.103 MPa (160 psi). The water flow rate and pressure were externally controllable via a potentiometer setup.

Figure 3.6 Electrical Water Pump

3.1.6 Tubing and Accessories

The main tubing used to feed the boilers with water and to route the generated steam into the collector was stainless steel single wire braided Teflon hoses from Aeroquip capable of handling a maximum operating temperature of 260℃ at 20.68 MPa. As for the various adapters and fittings used across the system, they were either made from anodized aluminum or stainless steel.

3.2 Experimental Instrumentation

The main thermocouples used on the water circuit side as well as in the exhaust runners during the experimentations were rugged 304 stainless steel pipe plug configuration K type ungrounded Omega sensors. Others used at various locations were J type. The thermocouples have limits of error of 2.2°C or 0.75% (whichever is greater).

The pressure transducers used upstream and downstream of the water pump were PX209-015G5V with an accuracy of 0.25%. As for the pressure transducer used in the steam collector, it was a PX32B1-150GV sensor from Omega capable of reading up to 1.034 MPa (150 psi) at 168℃ with an accuracy of 0.25%.

The volume flow rate sensor used during the experiments was a Saier SEN-HZ 21 FB which has a working range from 1 to 30 L/min at a maximum operating pressure of 1.7 MPa (247 psi) and temperature of 80℃.

The power supplies used to power up the instrumentation were BK Precision 1740B a Xantrex LXD20-3/5 and an Anatek 25-2D.

3.3 Data Collection

3.3.1 Engine Dynamometer

The key component that made this research possible was the engine dyno. The test engine was mounted on a SuperFlow SF-833 hydraulic engine dynamometer with a rated range and torque measurement accuracy of 0–1,000 ft-lb (0–1350 N-m) x 0.3 ± 0.2% [17]. The dynamometer test bench with Xconsole was used to perform the steady-state control tests and a portion of the data acquisition.

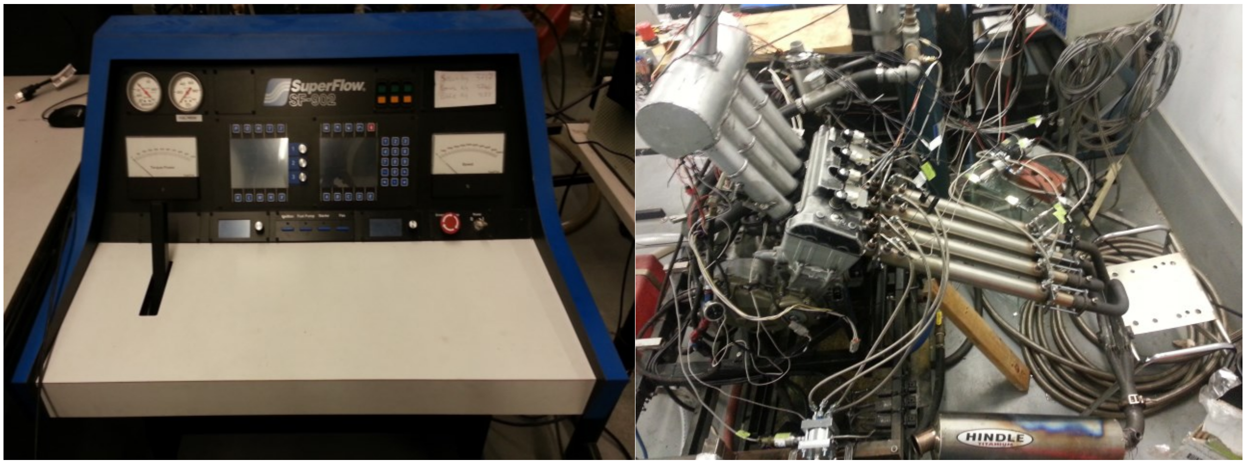

Figure 3.7 Engine Dynamometer with the Xconsole

3.3.2 LabVIEW Data Acquisition

The core of the data acquisition was performed by means of a National Instruments NI cDAQ-9178 module and the LabVIEW software. Except for six thermocouples used by the Xconsole, all other instrumentation was connected to the DAQ for signal processing in conjunction with LabVIEW which was then used in order to log the experimental data via a laptop.

Figure 3.8 Data Acquisition Module

3.3.3 MoTeC M400 ECU

The experimental engine was fully controlled by a reprogrammable MoTeC M400 Electronic Control Unit that allows the user to have a complete control over the inputs into the engine, such as fuel flow, ignition timing as well as other available compensations. It also allows for a close monitoring of the engine's status and additional data logging.

Figure 3.9 MoTeC M400 ECU

3.4 Experimental Setup

Prior to explaining the experimental procedure, it is important to clearly depict the experimental system in schematic form to clearly identify the location of each components as well as to understand the location of each thermocouples and pressure transducers. Following a detailed examination of Figure 3.10, the reader should have a clear understanding of the whole setup and can now clearly follow along in the next section.

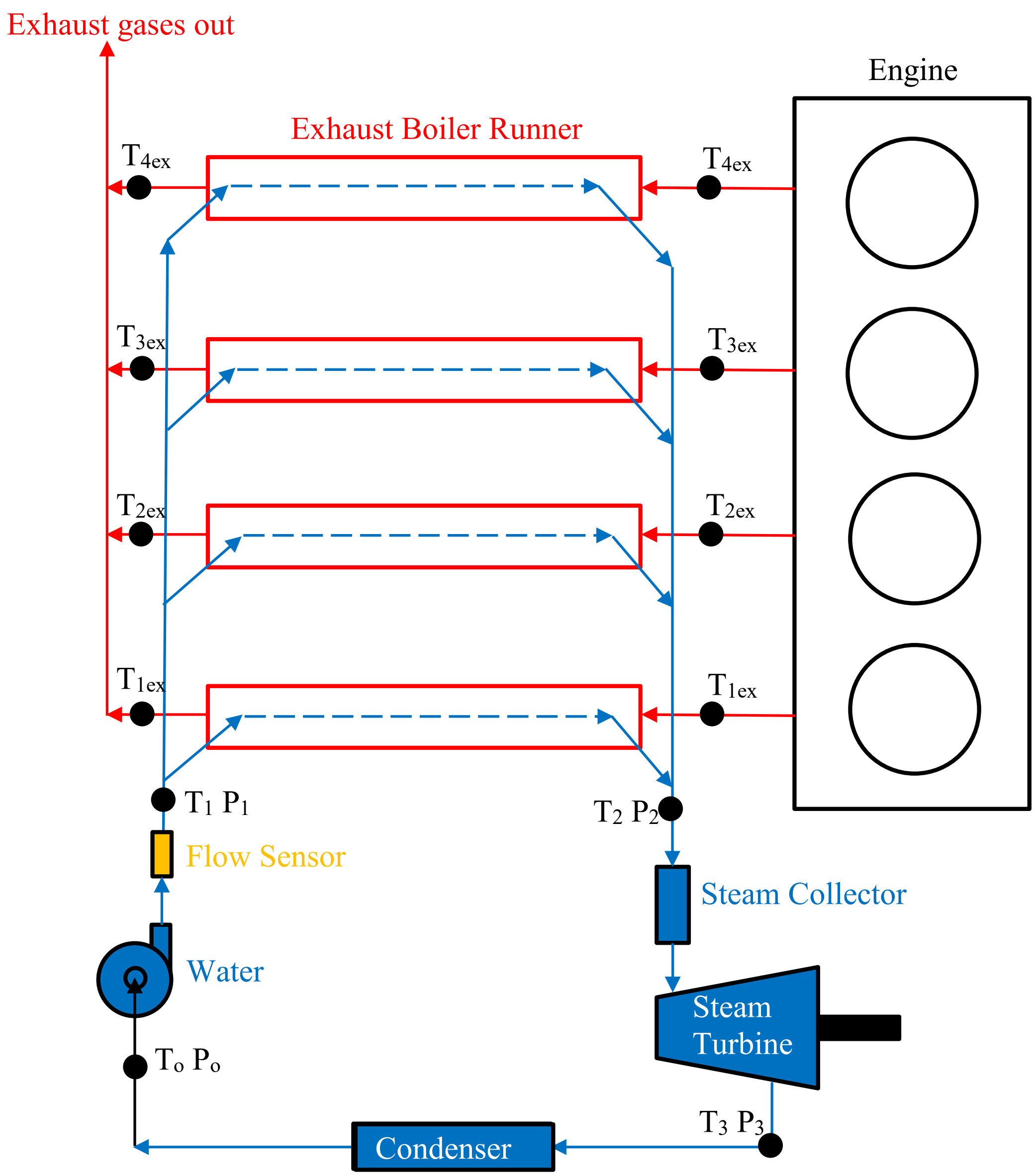

Figure 3.10 Schematic Representation of Experimental Setup

3.5 Experimental Procedure

Now that the reader is familiar with the individual components and instrumentation used in this system and how they fit together along with their locations, the procedure followed to obtain the experimental data can be clearly explained without ambiguity.

Every engine dyno test sessions begun by warming the engine up to operating temperature in order to make sure the engine was running correctly. This was done by holding the engine at 3000 RPM without load until the engine temperature sensor, monitored via the MoTeC ECU, reached 80℃. Once all sensors and parameters were confirmed as being operational, the baseline testing could begin.

In order to fully assess the overall impact of flowing water around the exhaust runners, a baseline dyno run had to be done with no water flow. This was essential to ensure that the energy recovered in the Rankine circuit was not being negated by a simultaneous decrease in engine performance potentially due to the cooling effect of the water onto the runners or due to another phenomenon that would then need to be identified and addressed.

The tests were performed using the hydraulic dyno's Xconsole in order to maintain the engine at a specific speed for the duration of the experiments. Prior to the execution of the baseline runs, the engine's fuel and ignition maps were tuned at wide open throttle condition across the range of speeds in order to yield optimal results for this new experimental setup. The baseline runs were then performed by running the engine at the required speeds, during which its power and torque output as well as the exhaust gases and engine coolant temperatures were constantly being monitored and recorded via the Xconsole. Exhaust gas temperatures before and after the heat exchanger sections of the runners were also being logged via the DAQ and LabVIEW program. Various engine sensors, such as the intake air temperature, manifold absolute pressure, fuel pressure, exhaust gas air/fuel ratio and others were being recorded via the MoTeC ECU.

The next step was to repeat the exact same dyno run yet with water being run through the exhaust boilers. All the same sensors previously mentioned were being monitored and recorded along with the water temperatures and pressures at various locations around the system, as detailed in Figure 3.10, as well as the volume flow rate, all of which being logged via the DAQ and LabVIEW software. The engine was held at a constant speed until the temperature values across the systems had stabilised for at least a minute.

4. EXPERIMENTAL RESULTS & DISCUSSION

4.1 Experimental Results

It should be mentioned here that several runs were performed at each engine speed and the values used to generate the graphs below of the experimental results are the average of the values collected at various speeds. The selection of the target dwell speeds for data collection were based on the fact that the engine is more stable at certain speeds, namely: 2500, 4000, 4500, 6000, 7000 and 8000 RPM. It should be noted that the engine has the capability of running up to 14000 RPM, but for safety of the operators and concern on engine durability while dwelling at such high speeds, the experiments were capped at 8000 RPM.

The first series of experimental data that is presented here are the temperatures of the exhaust gases measured at each runner as they enter the heat exchanger section. These are depicted in Figure 4.1 for the baseline value and in Figure 4.2 with the water flowing in the jacket.

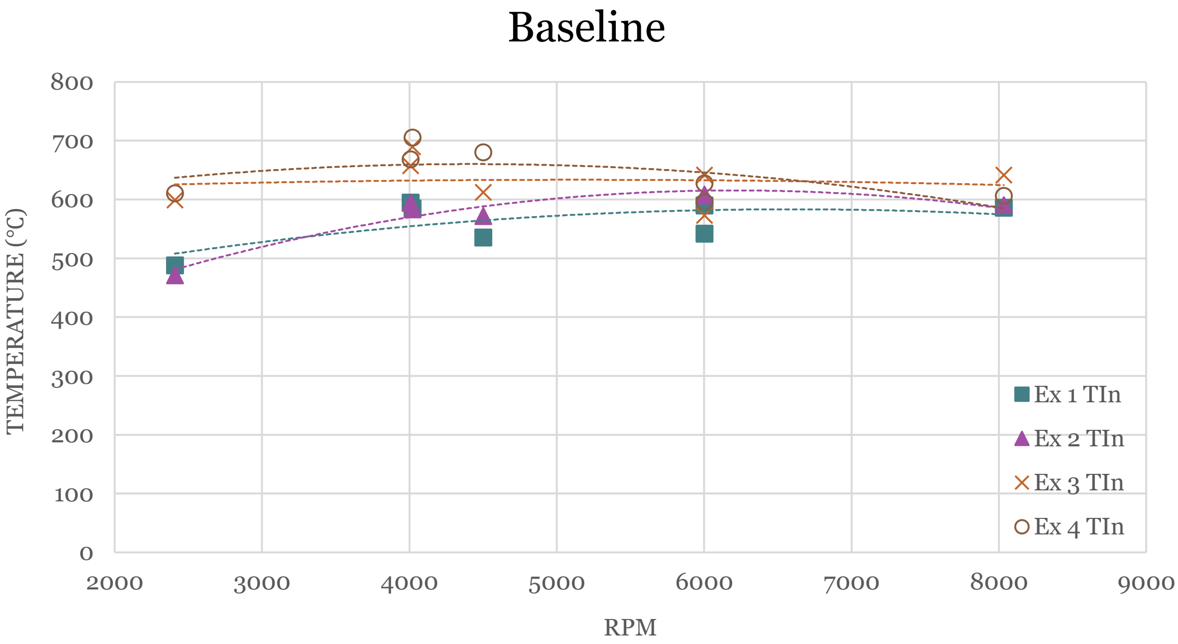

Figure 4.1 Exhaust Gas Temperature Inlet to Heat Exchanger per Runner – Baseline

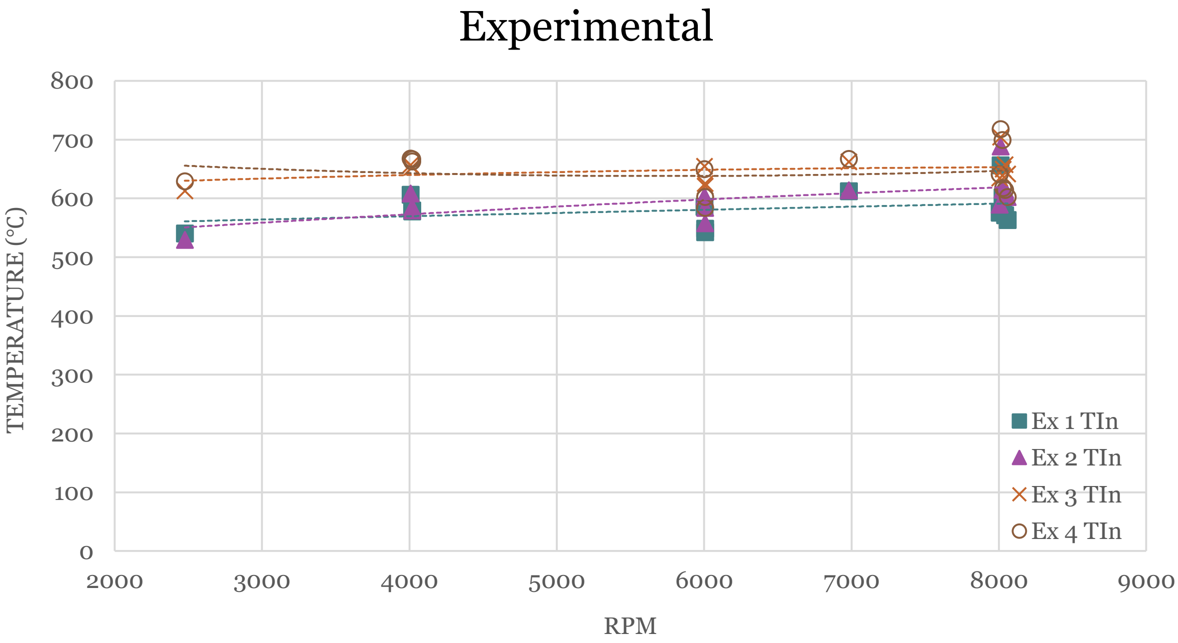

Figure 4.2 Exhaust Gas Temperature Inlet to Heat Exchanger per Runner – Experimental

Following a close examination of Figure 4.1 and the underlying data, it is determined that the baseline average exhaust temperature across all engine speeds for all runners combined is 601.8℃. As for the average exhaust temperature with the water flowing in the annular volume as depicted in Figure 4.2, it is 618.2℃, which amounts to a difference of about 2.69%.

The next point of interest here is the temperature of the gases as they exit the heat exchanger section displayed below in Figure 4.3 and Figure 4.4.

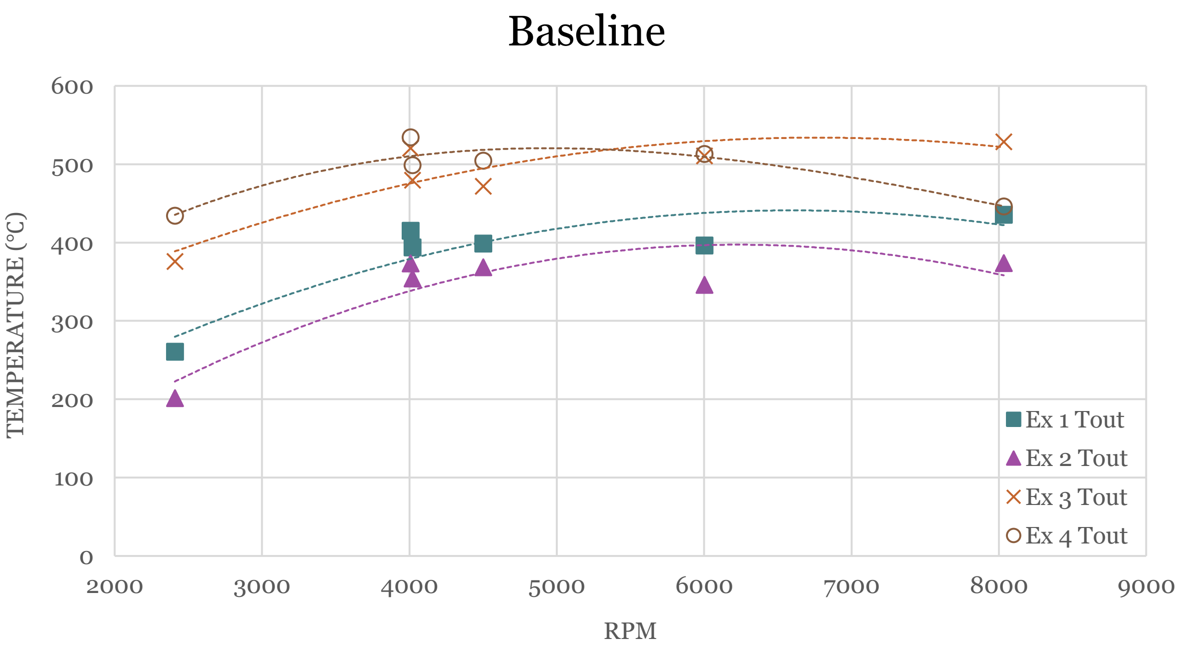

Figure 4.3 Exhaust Gas Temperature Outlet from Heat Exchanger per Runner – Baseline

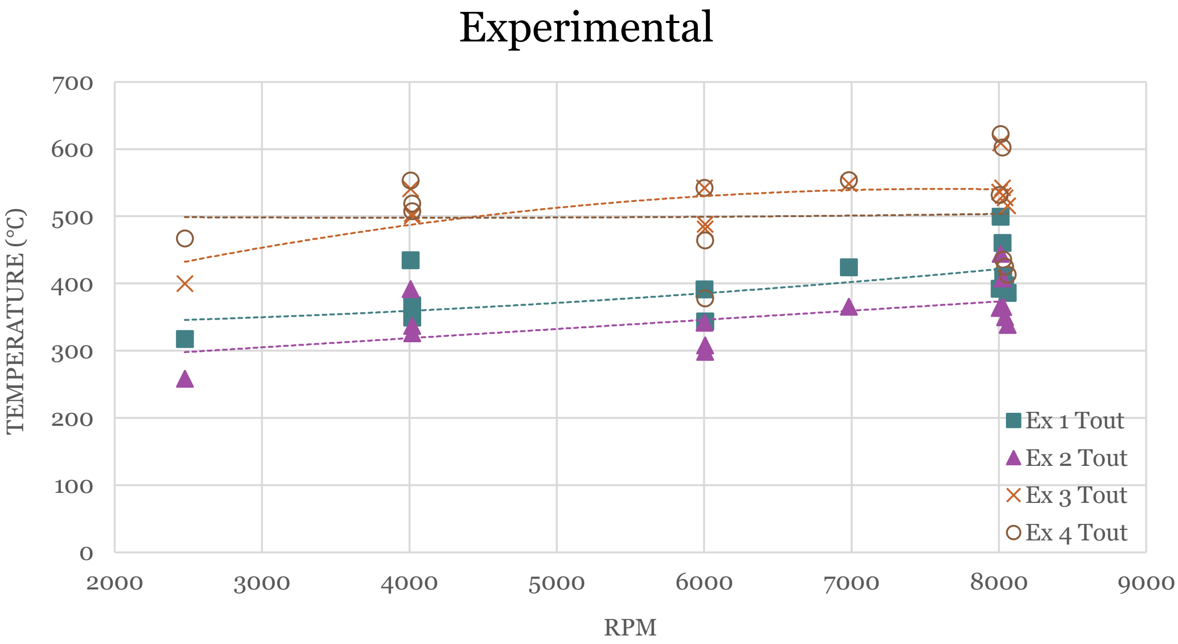

Figure 4.4 Exhaust Gas Temperature Outlet from Heat Exchanger per Runner – Experimental

Following a close examination of the outlet temperatures, it is observed here that the baseline average exhaust temperature across all engine speeds for all runners combined is 422.2°C. As for the average exhaust temperature with the water flowing in the annular volume as depicted in Figure 4.4, it is 440.8°C. This amounts to a difference of about 4.32%.

Prior to moving on to the amount of energy released from the exhaust gases, the variations in temperatures of exhaust gases as they pass through the heat exchanger section is graphically depicted in Figure 4.5 and Figure 4.6, for the baseline and test runs respectively.

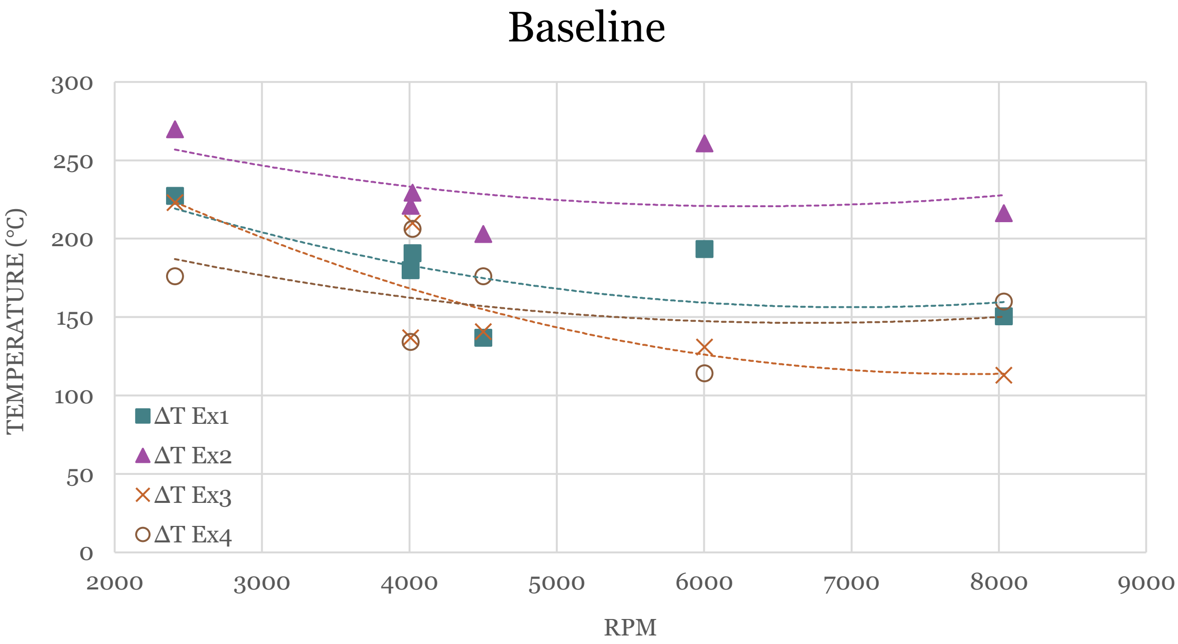

Figure 4.5 Exhaust Gas Temperature Variation per Runner – Baseline

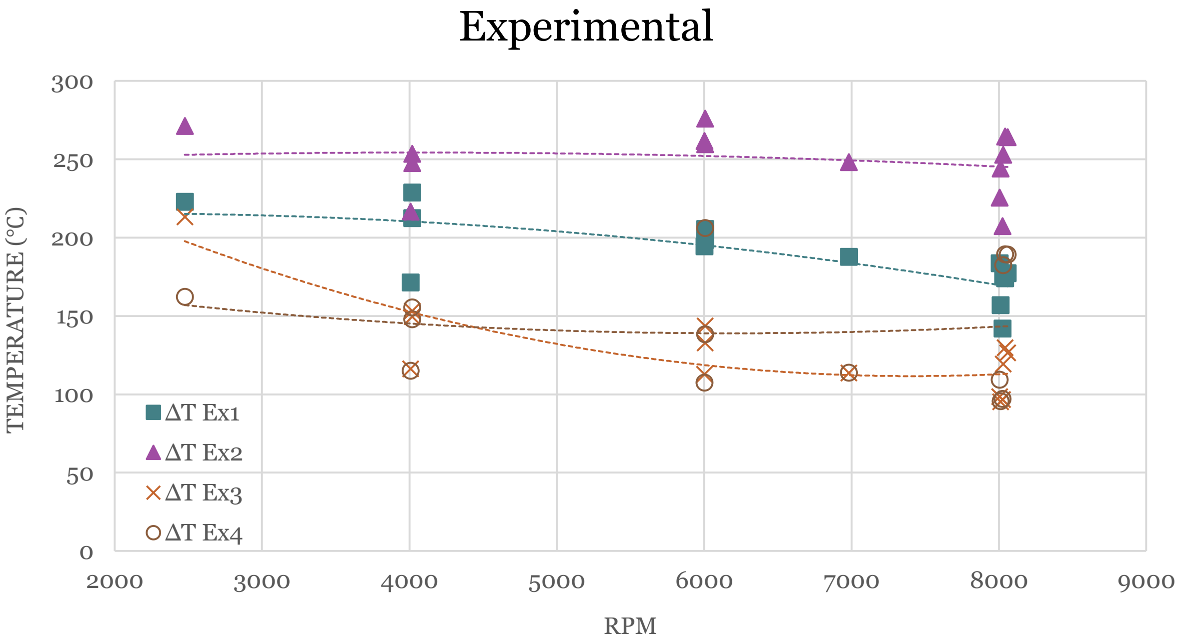

Figure 4.6 Exhaust Gas Temperature Variation per Runner – Experimental

A brief look at the data behind the temperature variations reveals that the baseline average variation in exhaust temperature across all engine speeds for all runners combined is 183.3°C. As for the average temperature delta with the water flowing in the annular volume, it is 177.4°C. This results in a difference of approximately 3.29%.

Now that the exhaust temperatures and variations have been reported, the amount of heat released in function of engine speed can be examined. Figure 4.7 and Figure 4.8 below, display the magnitude of the heat released per runner as well as the total amount of heat expelled through the heat exchanger section for the baseline and test runs respectively.

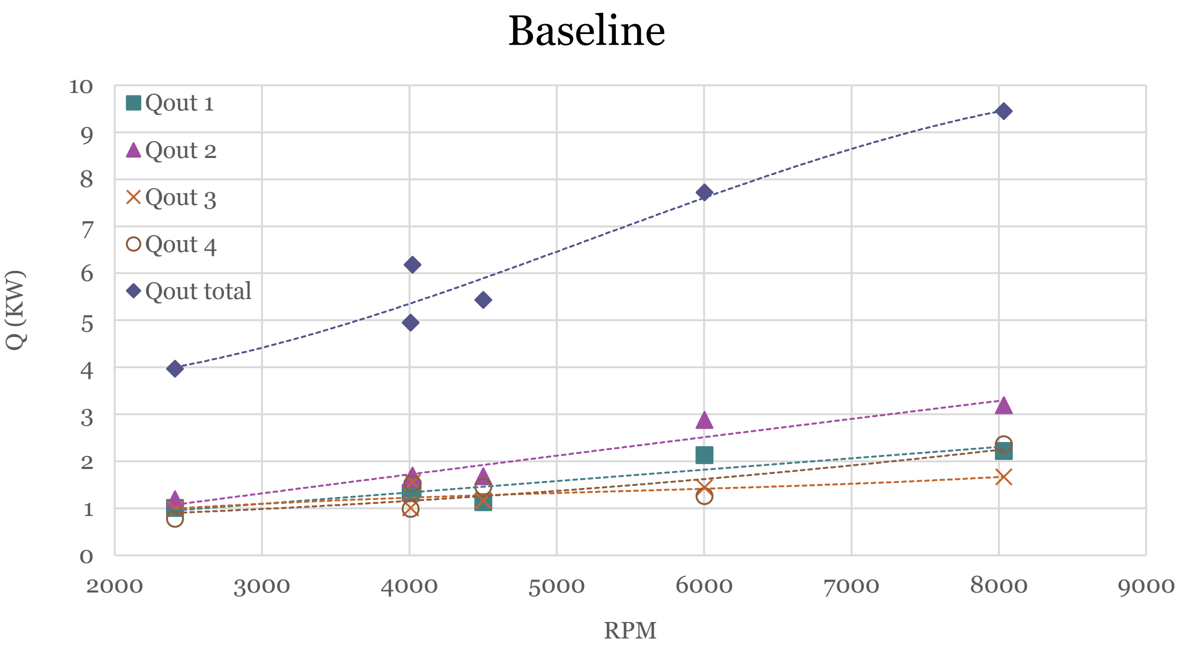

Figure 4.7 Heat Released in Function of Engine Speed – Baseline

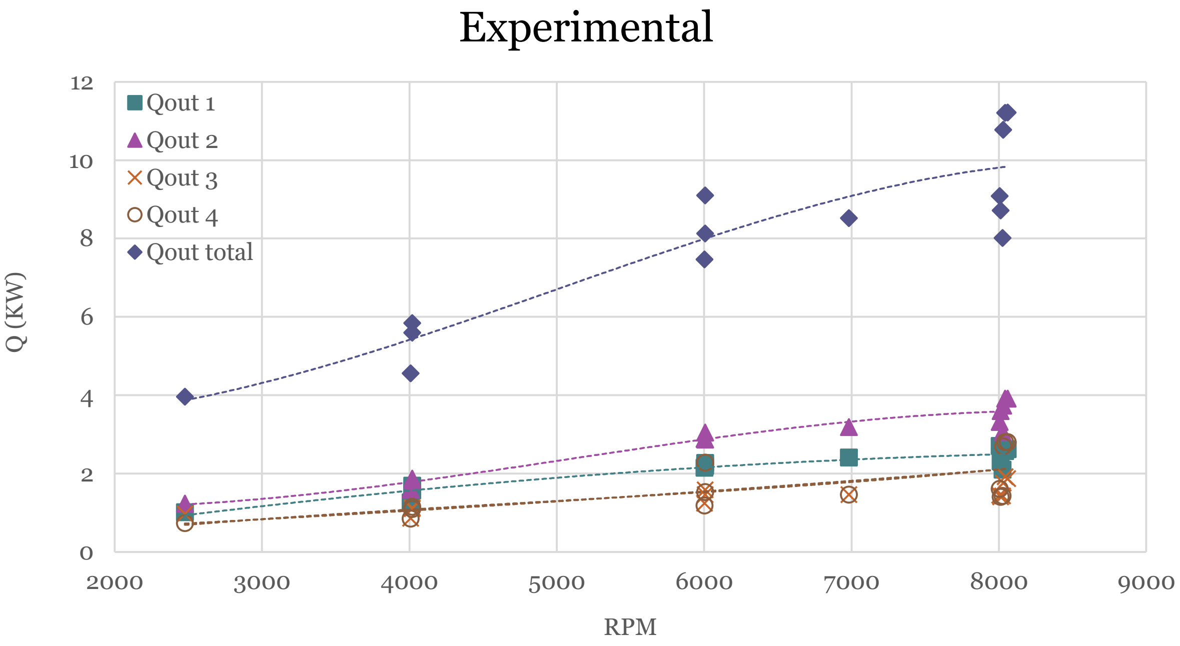

Figure 4.8 Heat Released in Function of Engine Speed – Experimental

Having the total amount heat released through the exhaust gases at various engine speeds, the next data series of interest will be the magnitude of heat recovered by the water flowing through the heat exchanger in function of engine speed. This relation is illustrated in Figure 4.9.

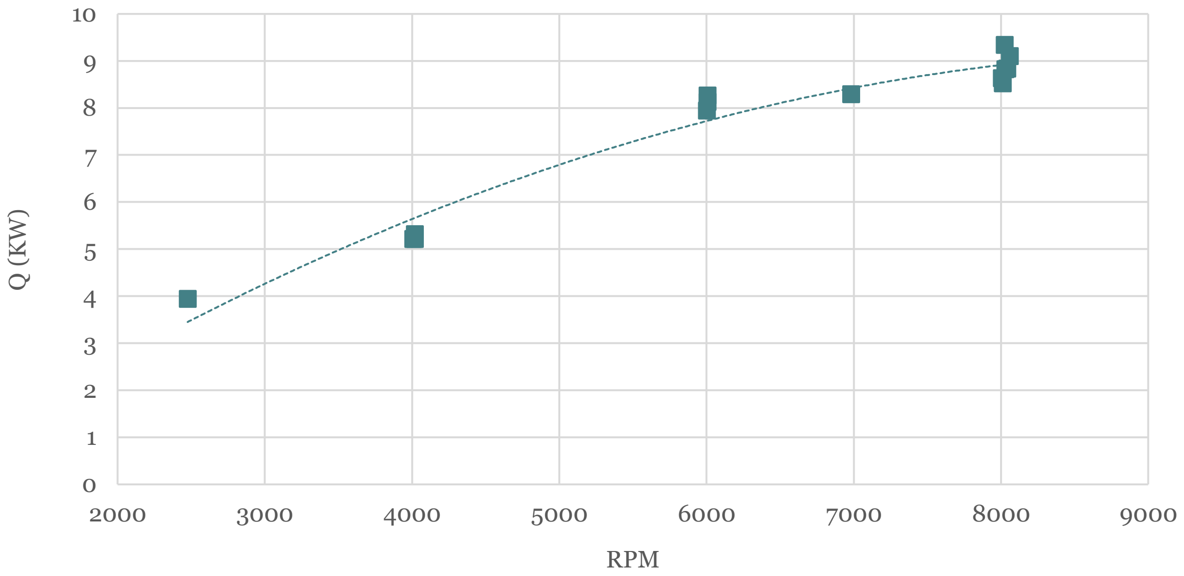

Figure 4.9 Heat Absorbed by the Water as a Function of Engine Speed

A side-by-side examination of Figure 4.8 and Figure 4.9 reveals that the amounts of energy released through the waste gases and recuperated through the water circuit are quite similar and follow similar functions with respect to engine speed.

The final data set that needs to be presented prior to proceeding to an in depth analysis of the results, is a comparison of the engine's performances as the water is flowing in the water jackets to the baseline values.

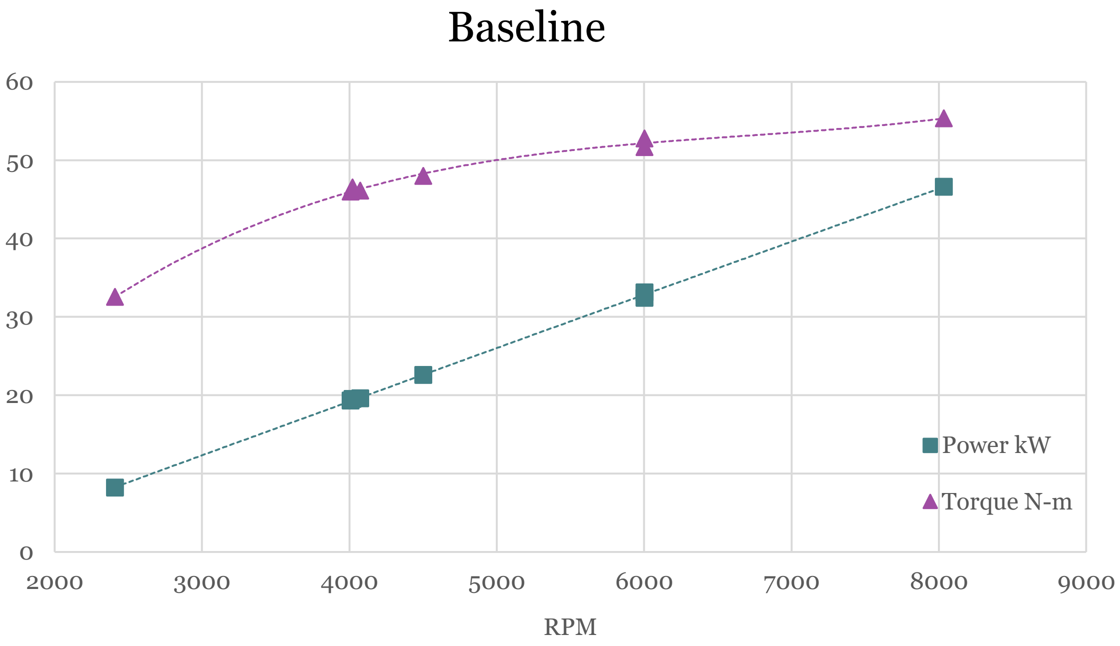

Figure 4.10 Engine Power and Torque as a Function of RPM – Baseline

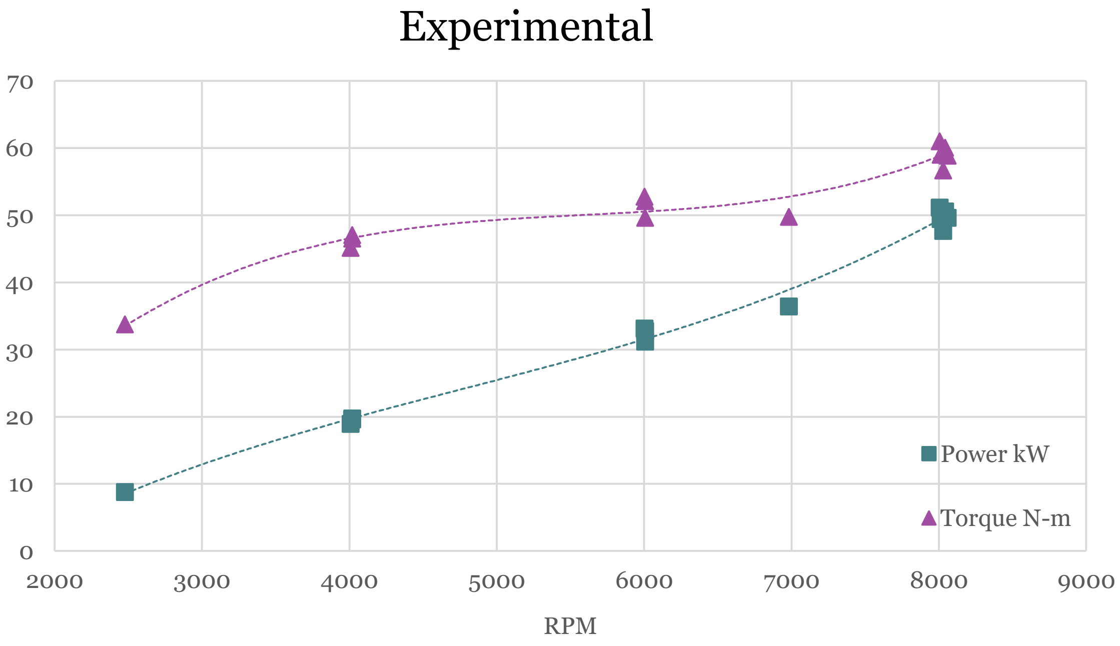

Figure 4.11 Engine Power and Torque as a Function of RPM – Experimental

A first glance at Figure 4.10 and Figure 4.11 will reveal that the baseline power and torque curves are quite similar from the ones obtained while running water through the heat exchangers, yet it should be noted that due to engine difficulties while trying to obtain the 7000 RPM data point for the baseline, this point was unfortunately impossible to obtain. The objective of comparing the experimental performance curves to the baseline ones was primarily to demonstrate that flowing water in the heat exchanger didn’t directly reduce the engine’s performances, thus potentially partially or completely negating any energy recovery achievable via this system. It is interesting to note here that not only did the experimental runs not display any decline in performances, but they actually resulted in slight improvements over the baseline values, namely interesting improvements of 6.72% and 6.99% in engine power and torque respectively near the 8000 RPM range.

4.2 Comparison to Theoretical Values

Now that the experimental data has been displayed, it will be interesting to compare the theoretically predicted values to the actual ones obtained.

The first set of data that will be compared will be the average temperature difference in the exhaust gases across the heat exchangers. Figure 4.12 depicts both upper and lower bound theoretically predicted values onto which the experimental data has been added. It can be clearly seen that although the higher set of theoretical values seem to better predict the magnitude of the temperature variations, the lower bound series seems to better correlate the trend.

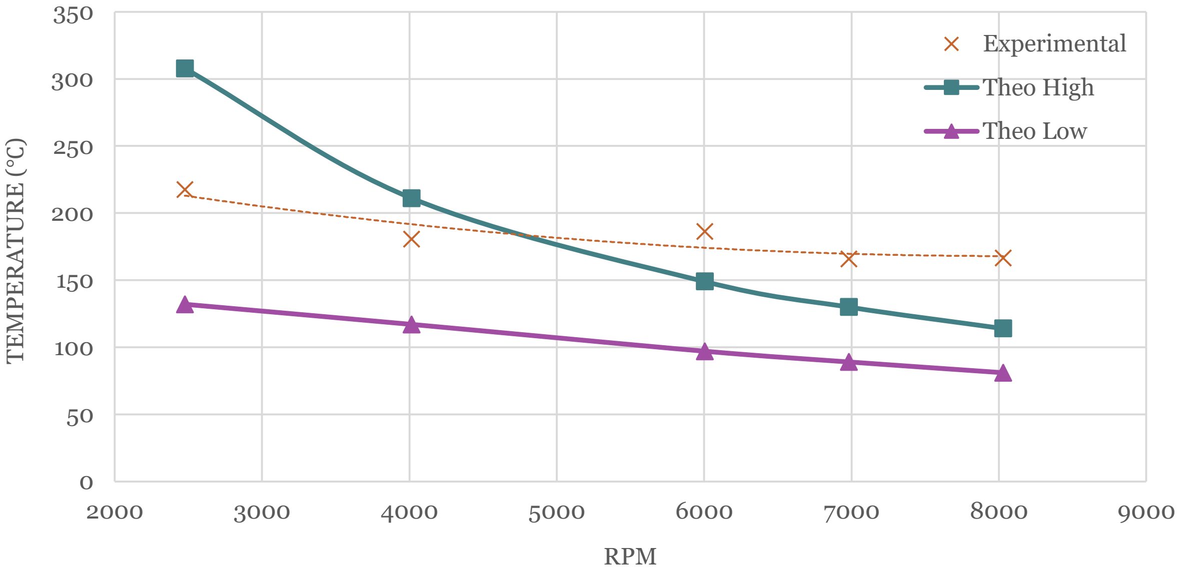

Figure 4.12 Average Exhaust Gas Temperature Variation Theoretical and Experimental

The next set of experimentally obtained data to be compared to the calculated one shall be the heat released from the spent gases. Following an examination of Figure 4.13, it can be stated that the experimental values were well within the theoretical boundaries up until about 4000 RPM after which, the magnitude of heats released surpass the upper bound predictions and also seem to diverge in direction.

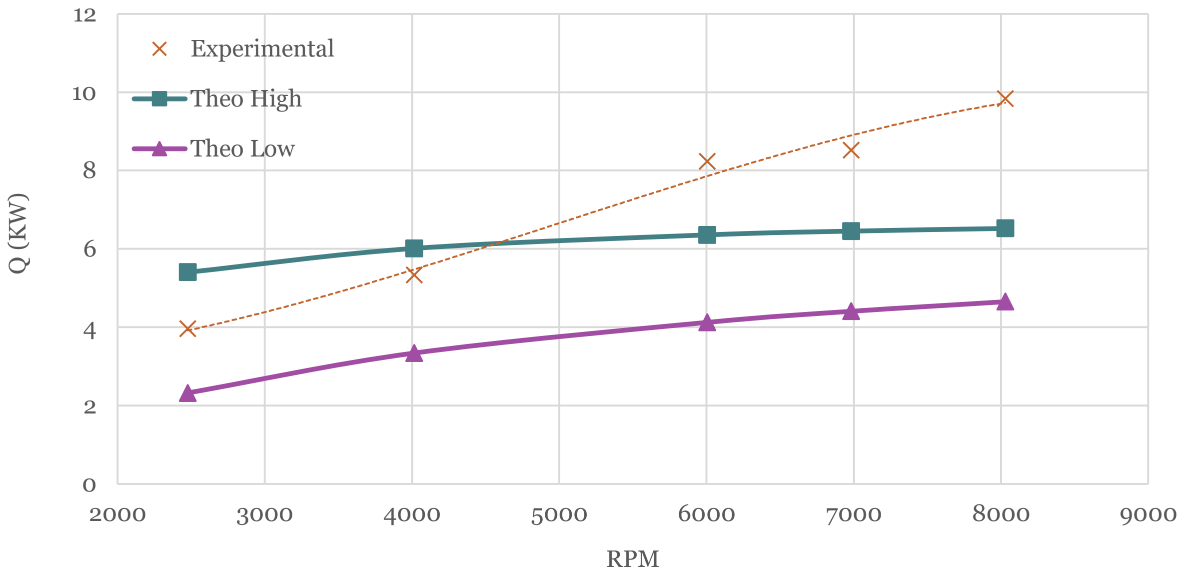

Figure 4.13 Heat Released in Function of Engine Speed Theoretical and Experimental

Following a complete compilation of the experimental data and its graphical representations, it was deemed important to contrast the brake power to the theoretically predicted indicated power output in order to first see if the calculated values accurately predicted the general trend and magnitude of the experimental results. As seen in Figure 4.14, this is clearly the case, the trend and magnitude both seem to confirm the validity of the underlying theory used to arrive at predicted values. Furthermore, to get a general idea of how the input energy was being utilised and the magnitude of its partition into each category (brake power, cooling, exhaust and other), this data is conveniently displayed first in a cumulative stacked column fashion, seen in Figure 4.15. Secondly, the same data is displayed in Figure 4.15 as a ratio of the total heat input per engine speed so that the reader can clearly view its evolution with engine speed. It is interesting to note here that the energy distribution percentage and evolution with engine speed is showing an analogous trend as reported in another similar research [7].

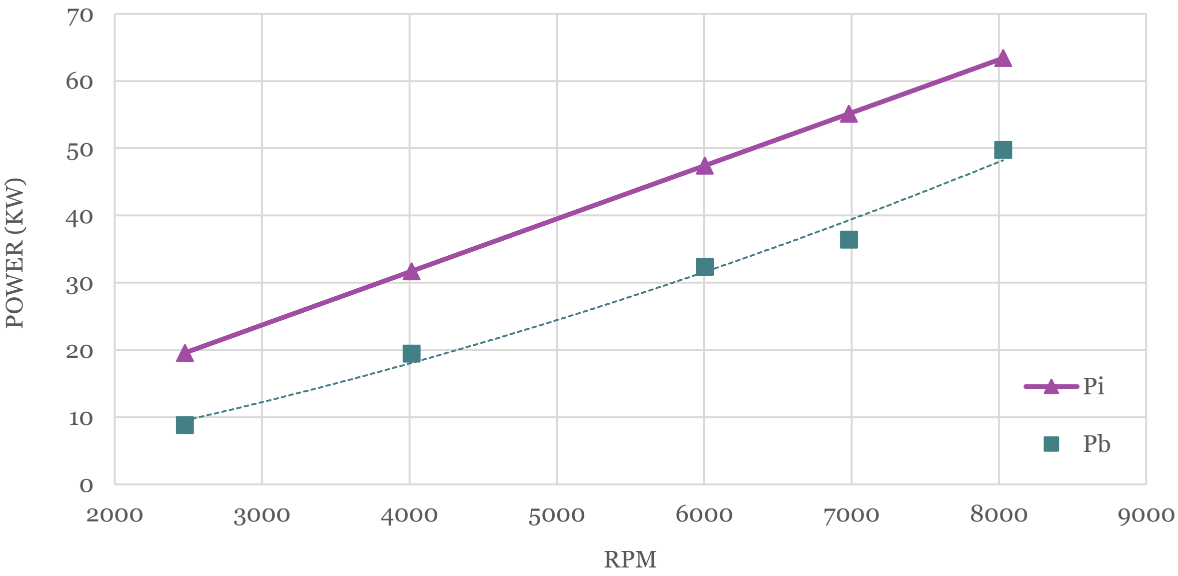

Figure 4.14 Theoretical Indicated & Average Experimental Brake Engine Power

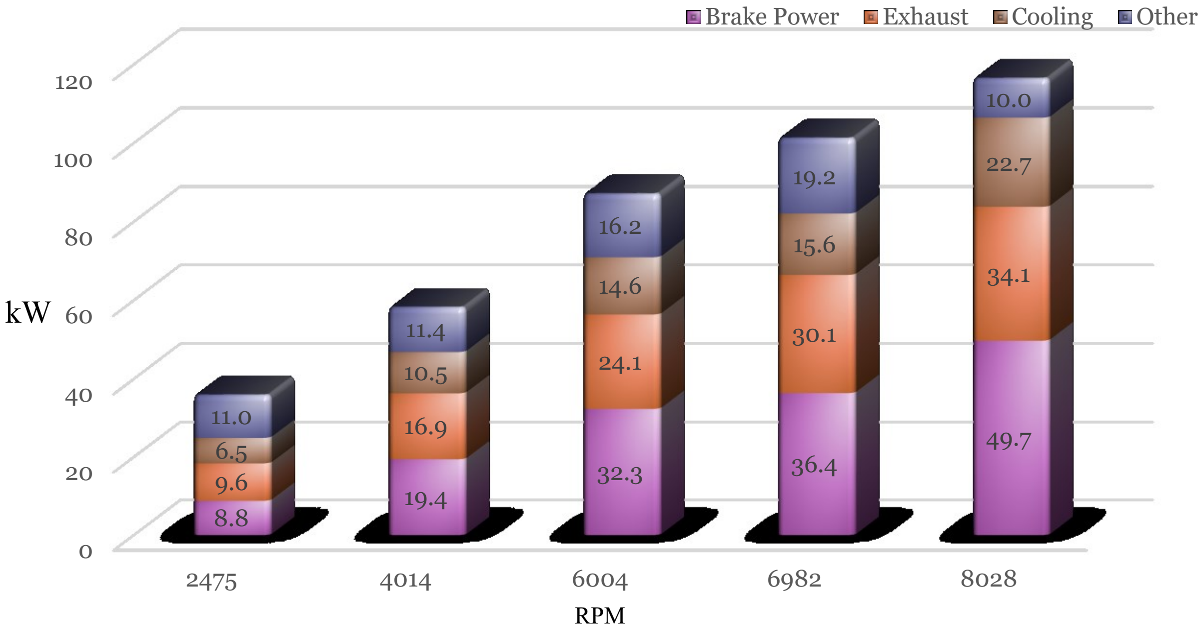

Figure 4.15 Energy Utilisation Magnitude per Engine Speed

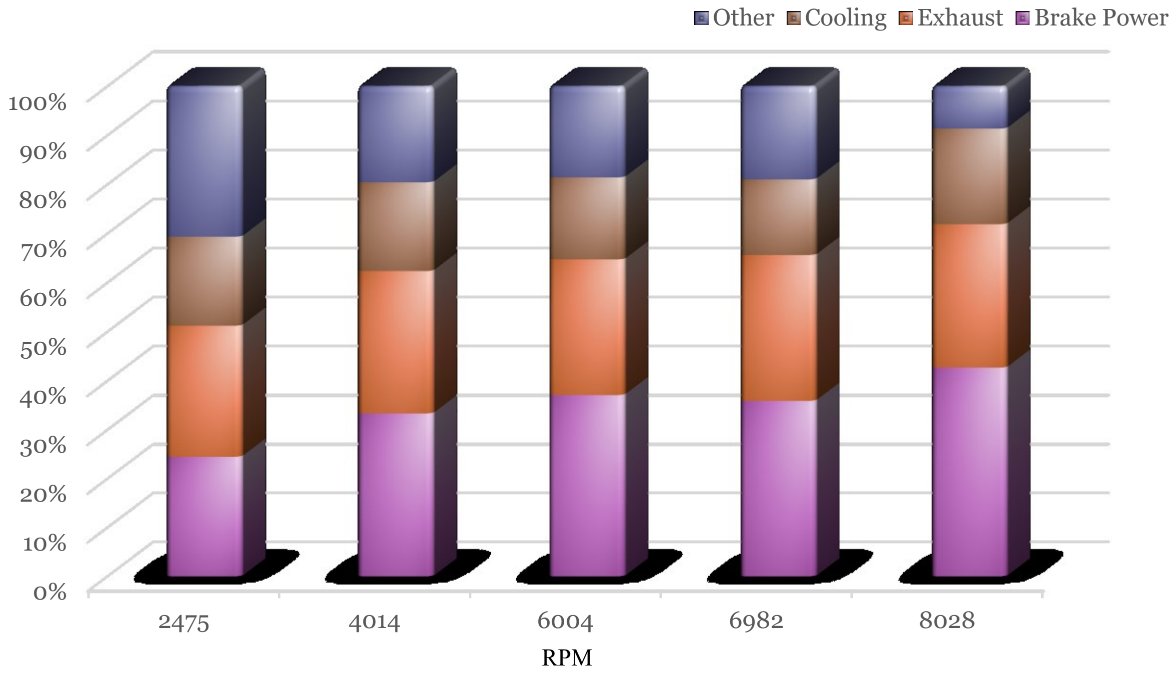

Figure 4.16 Energy Utilisation Percentage per Engine Speed

4.2.1 Sources of Discrepancy in Predicted Results

As seen in Figure 4.13, it is clear that the theoretically predicted values seem to level off at higher engine speeds while experimental data seems to show a slightly different trend. Initially the heat released during the tests were within the theoretical bounds up until about 4000 RPM, from which point they kept on increasing. This phenomenon could be attributed to a combination of factors, yet following a review on this issue, this divergence is mainly attributed to the fact that the Nusselt number, and thus the convection heat transfer coefficient, of an internal flow is significantly higher in the entrance region where the flow is thermally developing compared to the hydrodynamically developed downstream flow. It is considered to have reached a constant value only past a distance of 10 diameters, prior to which the generated results are considered as being conservative, as is obviously the case in these experiments [11]. This fact could indeed clearly explain the variation in question here since this entrance distance represents about 75.3% of the heat exchanger length in the present case. It is clear now that the exhaust runner section is mostly in the thermal entrance region which offers a reasonable explanation for the higher than expected heat released at this stage.

Another fact that could possibly have contributed to this discrepancy of the experimentally recorded data, yet to a lesser extent, is the conceivably lower than predicted surface temperature of the exhaust runners. As it is recorded in Table C.3 of Appendix C, the inlet water temperature was on average about 15.7℃ as opposed to the 85℃ used in the theoretical calculations. This was done for several reasons, mainly in order to keep a constant inlet temperature across experiments since the water being run through the boilers was externally supplied and not from the engine's water circuit, for simplicity of the experiments. Furthermore, the experimental mass flow rate actually used for the water was also significantly higher than the one required to yield the calculated results in the Rankine circuit. This was done in order to limit the maximum temperature reached by the water mainly to avoid a phase change, which would significantly change the properties of the working medium as the phase change would occur and beyond. The aforementioned would make practical calculations post-experimentation much more complicated since an average value for these parameters would have to be obtained or complicated integrals would have to be solved for simultaneously. This was also for operator safety reasons. Now the lower inlet water temperature and higher mass flow rate both have the effect of reducing the wall surface temperatures which in turn increase the magnitude of heat released from the exhaust gases, the reader is directed to Section 2.2.2 for a complete theoretical understanding of this phenomenon.

4.3 Adjusted Theoretical Potential of Steam Turbocharging

Now that the data has been clearly presented and compared to the theoretically predicted values, the true potential of this system can be detailed for the reader using actual data. The steam turbocharger circuit can be clearly detailed for a good understanding of how it could ideally operate.

In the first case, the steam turbine is coupled to a generator in order to recover the produced power, as was the case in the theory section and therefore the same efficiencies have been used here as well. The calculated average values have been tabulated in Appendix C for review and the potential energy recovery this setup has to offer have been graphically depicted in Figure 4.17 which shows a peak recovery of 1.4805 kW near 8000 RPM. Figure 4.18 shows how the recovery has a greater impact at lower engine speeds, namely a peak improvement of 7.446% in engine thermal efficiency and a possible reduction of 6.930% in brake specific fuel consumption.

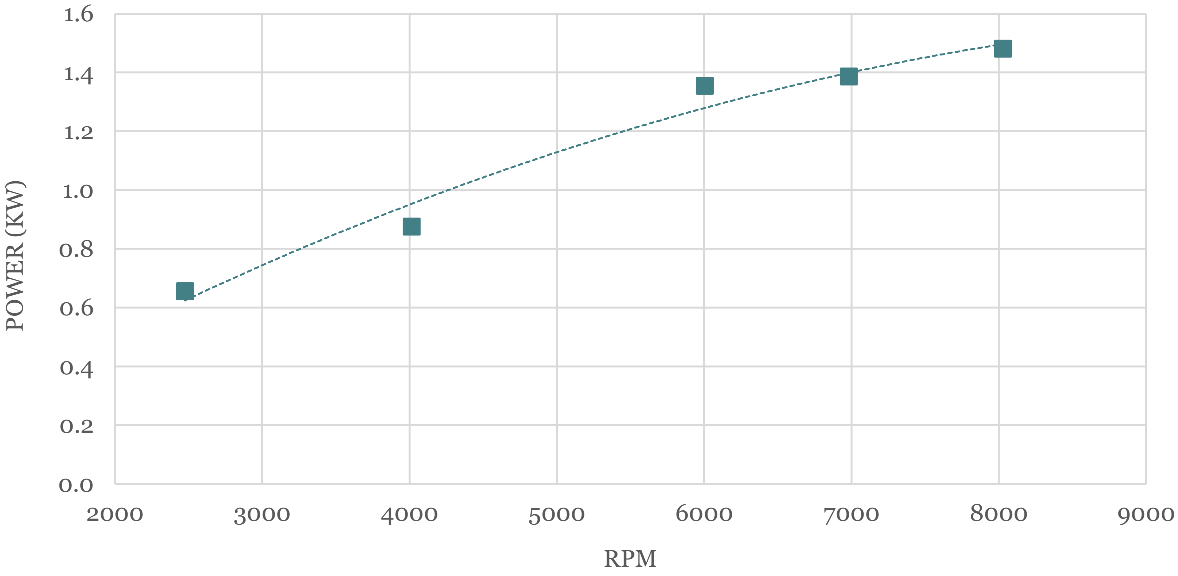

Figure 4.17 Potential Experimental Energy Recoverable by Generator

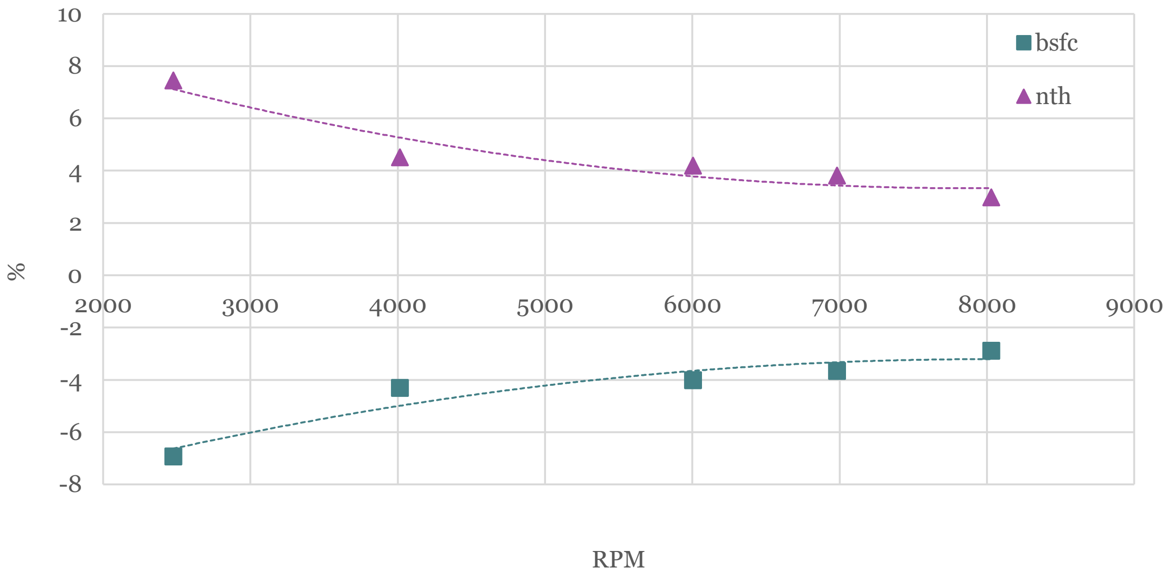

Figure 4.18 Potential Experimental Improvements in *bsfc* and Thermal Efficiency

In the second case, instead of coupling the turbine to generator, it is coupled directly to a compressor. This route was investigated and the results were reproduced in Appendix D for review. By adding a compressor, it is possible to gain up to 35.00% in brake engine power near 2500 RPM as seen in Figure 4.19. It should be noted here that in order to obtain the new figures for the brake engine power once it would be under forced induction, it was conservatively assumed that the engine's thermal efficiency remained constant at the values calculated from prior experimental data and therefore any increase in fuel injection would result in an increase in engine brake power by a ratio dictated by the engine's experimental thermal efficiency at the speed in question. The recovered energy was first used as a power input to the compressor in order to obtain an approximate initial pressure ratio. The process was then iterated using a similar technique as described in Section 2.4 in order to solve for the new engine mass flow rate and intake temperature yet keeping the power input to the compressor as constant since this figure was experimentally obtained and is considered here to be invariable for the purpose of these calculations.

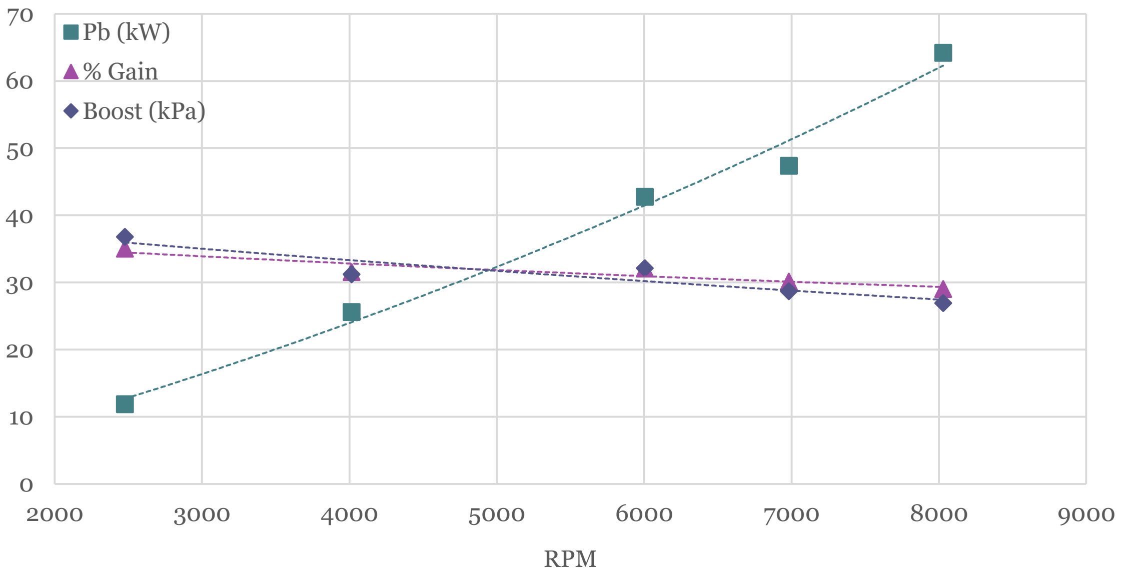

Figure 4.19 Potential Brake Power Gain with Steam-Turbo

4.3.1 Potential Power Density Improvements

The ultimate point of interest here is power density improvements of the current setup. In order for this increase in power to be worth it, it needs to outweigh the mass addition caused by the components required to make this possible in the first place. By taking a look at Table 4.1, the reader can have a detailed look into the weight of the individual components of the system which have been weighed following disassembly of the experimental engine. It should be noted here that an approximate, yet very conservative, value was arbitrarily selected for the generator's weight as well as for the volume of water in closed system. Furthermore, the components designed here were for the sole purpose of this experimental study and their weight could easily be reduced for actual application and therefore these weights are also to be considered as very conservative for the purpose of this section. The boiler's weight was not included since the engine would need an exhaust system regardless of this experiment and therefore it was purposely left out of the table in this section.

To analyse the first case, the original engine's wet weight from Table 2.1, which includes engine oil and coolant, is used and the weight of the generator system is added to it. It is therefore determined that the final system weight would be 77.69 kg. Adding in the peak recovered energy, namely 1.4805 kW near 8000 RPM, to its brake engine power and dividing by the new weight yields a power density of 0.619 kW/kg which represents a reduction of 13.41% in this figure.

The next case is determined by doing the same exercises described above yet for the steam-turbocharger system. The final system weight here would be 78.93 kg and the peak brake power used would be 64.16 kW which ultimately results in a power density of 0.813 kW/kg, a 13.73% increase in the figure.

Following this preliminary analysis, it would seems obvious that using the steam-turbocharger approach would be logical route since it yields positive improvements in power density. It should be noted here that using a generator system still yields improvements in thermal efficiency and reduction in *bsfc*, facts that are not to be neglected since in fixed applications where weight is not an issue, this system still offers attractive incentives.

Table 4.1 System Component Weight Specifications

Generator-System	
Component	***Weight (g)***
Pump collector	270
Pump	670
Flow rate	30
Water Splitter	310
Steel Braided Lines	1160
Steam Collector	1010
High Pressure Sensor	190
Thermocouples	45
Kalina Radiator	500
Generator	3200
System Water	5000
Total	**12385**

Steam-Turbocharger	
Component	***Weight (g)***
Pump collector	270
Pump	670
Flow rate	30
Water Splitter	310
Steel Braided Lines	1160
Steam Collector	1010
High Pressure Sensor	190
Thermocouples	45
Kalina Radiator	500
Generator	3200
System Water	5000
Compressor	1240
Total	**13625**

4.4 Kalina Cycle Post-Analysis

A brief note here should be made on the usefulness of heat recovery from the cooling system in order to preheat the water prior to sending it to get superheated in the boilers. Looking at the quantity of heat absorbed across the engine speeds, it is determined that on average, the Kalina cycle heat recovered accounts for about 3.59% of the total recovered heat. A quick glance at the heat released through the experimental cooling system shows that the heat required to drive the Kalina cycle represents, on average, a mere 1.85% of the magnitude of heat release via this mode, a magnitude which is obtained by using the temperature delta across the cooling tower along with the engine water pump flow rate correlation to engine speed. Since all inlet and outlet temperatures as well as mass flow rates of both circuits are known, a quick thermal analysis can be done here to determine the required size for the water to water heat exchanger required for this application.

In order to assess the actual usefulness of this component, its weight should be low enough in order to yield a power density above the engine's original figure of 0.715 kW/kg. Using the experimentally determined Kalina recovered energy value of 0.3186 kW near 8000 RPM, this heat exchanger along with the water inside it shouldn't weigh more than 0.446 kg. Furthermore, it should be investigated if this benefit outweighs the cost and downsides of this added system complexity and therefore if this modest heat gain is worth the trouble of adding an additional radiator.

4.5 Turbine Preliminary Design

In order to complete this analysis, it is essential to cover the preliminary design of the turbine needed in order to efficiently drive the compressor using the experimental data as design limitations. Now before proceeding to the operational parameters of the steam turbine, a compressor selection needs to be made so that a range shaft speeds can be identified. Now taking a look at Appendix D, it can be observed that the selected compressor should operate at a pressure ratio within a range of 1.265 to 1.364 and at a mass flow rate of 0.01668 to 0.05169 kg/s (2.206 to 6.837 lb/min). Assuming that a Garrett® compressor is selected and using the previously mentioned selection criteria, a GT1548 would fit the current application [18]. This compressor and its performance map are displayed in Figure 4.20 for clarity.

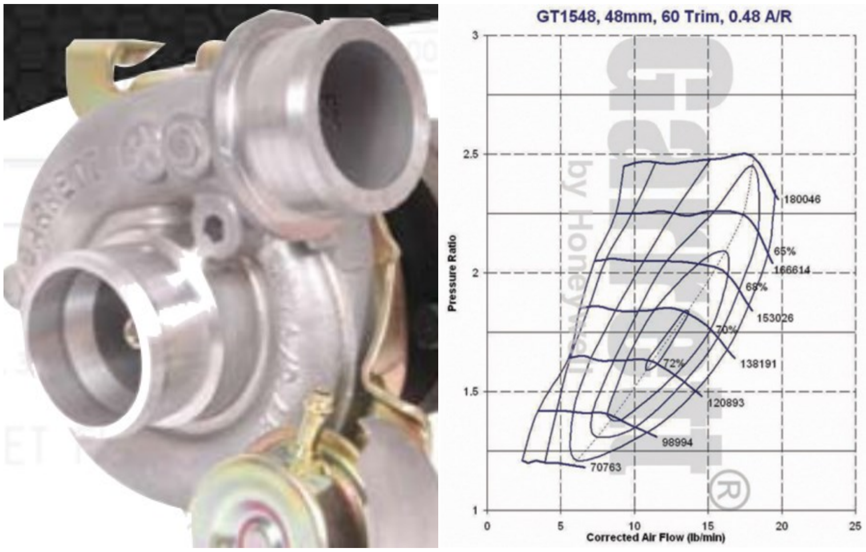

Figure 4.20 Garrett$^{®}$ GT1548 Compressor and its Performance Map [18]

From the GT1548 compressor's map, it can be clearly seen that the compressor would operate at an average speed of approximately 84879 RPM (8888.5 rad/sec), this shall be the initial design speed for the turbine. Using the experimental data for the Rankine circuit from Appendix C, the turbine inlet temperature and pressure used for the purpose of this preliminary design will be 675.2 K and 800.0 kPa respectively. The average water mass flow rate and turbine power output across the engine speeds shall be used here, namely $2.365 \cdot 10^{-3}$ kg/s and 1.278 kW respectively.

Now that the preliminary design parameters are set, focus can be shifted to obtaining the required turbine dimensions in order to see if this is feasible. Assuming the steam turbine will be an impulse type with a conservative turning angle of $\theta = 145^{\circ}$ [12]:

$$\dot{W}_t = \omega \tau_{out} \tag{4.1}$$

$\rightarrow \tau_{out} = 0.1438 \text{ N} \cdot \text{m}$

$$\tau_{out} = R_t(1 - cos\theta)\rho A_{nozzle} V(V - U) \tag{4.2}$$

where:

$$U = R_t\omega \tag{4.3}$$

$$\dot{m}_{water} = \rho A_{nozzle} V \tag{4.4}$$

therefore Eq. (4.2) becomes:

$$\tau_{out} = R_t(1 - cos\theta)\dot{m}_{water}(V - R_t\omega) \tag{4.5}$$

In order to solve Eq. (4.5) and obtain the exit velocity of the steam from the nozzle onto the turbine blades, an initial estimate needs to be made for the radius of the turbine. Using a radius of 0.0600 m yields a steam velocity of 1091 m/s as it exits the nozzle, which results in a nozzle cross-sectional area of $8.359 \cdot 10^{-7}$ m^2 or a nozzle diameter of $1.032 \cdot 10^{-3}$ m.

Now since the velocity of the steam seems quite high, it is presumed that the flow would be choked and therefore the analysis has to continue in order to further refine the geometries and to make sure that the flow dynamics and properties required to drive the turbine at the required specifications are feasible. To verify the choked velocity, first the static pressure of a choked flow need to be obtained [19]:

$$\frac{P^*}{P_o} = \left(\frac{2}{n+1}\right)^{\frac{n}{(n-1)}} \tag{4.6}$$

where P^* is the choked flow static pressure, P_o the stagnation pressure and n is equal to 1.3 since it is an exponent used for superheated steam which has been obtained experimentally [19].

Now:

$$V^* = \sqrt{nP^*v} \tag{4.7}$$

where V^* is the choked velocity and v the specific volume of the steam.

This analysis results in obtaining a choked steam flow velocity of 590.7 m/s which is well below the required velocity above. This means that further consideration is needed in this matter.

Shifting focus on the average angular speed the turbine is meant to be subjected to, it would be wise to make sure that the turbine blades are capable of withstanding the stresses they would be exposed to. In order to simplify this preliminary design, the blades will be assumed as having a constant cross-sectional area. An initial turbine wheel design is seen in Figure 4.21. Using this design in order to obtain an approximate blade cross-sectional area ($2.421 \cdot 10^{-5}$ m^2) and using aluminium alloy 6061-T6 as the material of choice for the turbine construction with an arbitrary safety factor of 1.3 [16]:

Figure 4.21 Preliminary Turbine Wheel Design

$$(\sigma_{ct})_{max} \cong \frac{4}{3}\pi N^2 \rho_b A \tag{4.8}$$

Solving for *N* in Eq. (4.8) yields a maximum allowable rotational speed of 25921 RPM for the turbine wheel. This will be an additional parameter that will have to be kept in mind when completing the turbine design. Since the compressor needs to be rotating at about 84879 RPM, either a 3.27:1 gear ratio will need to be utilised or an alternative solution will need to be conceived. Furthermore, it should be noted that only the centrifugal tensile stress has been considered at this design stage and that additional limitations need to be verified simultaneously in order to yield a viable design. Example of such design constraints include, but are not necessarily limited to, creep, high-cycle fatigue, thermomechanical fatigue, gas bending stress and centrifugal bending stress when the centroids of the blade cross-sections at different radii do not lie on a radial line.

Since this section is included to essentially give the reader an idea of the path to be taken in order to begin the design of the steam turbine, the present analysis will stop here since it is beyond the scope of this research, but needless to say this a mere approximation of what the overall turbine dimensions would be and further analysis is required in order to optimise the design of this critical component.

4.6 Potential Application

This section has been added as a concluding segment in order to describe in detail how the steam-turbocharger circuit could be constructed in order to yield optimal results from the application of this system.

The reader is initially directed to Figure 4.22 in order to gain an understanding of the component locations with respect to each other. The Rankine cycle has been left intact and the Kalina cycle was left out for simplicity. What has been added here is the compressor circuit on the air intake and a generator located on the steam turbine/compressor housing. The way this system would operate would be by running the Rankine circuit as efficiently as possible in order to allow the steam turbine to produce as much power as possible under all conditions. Now the pressure ratios generated by the compressor would be controlled via the generator which would act as a regulating device, limiting the compressor speed by applying an electrical load to the shaft connecting the turbine to the compressor which would by the same occasion recharge the battery. The current could also be reversed in the cases when the steam turbine isn’t producing enough power for the compressor to generate the required pressure ratios as dictated by the engine’s complete tuning.

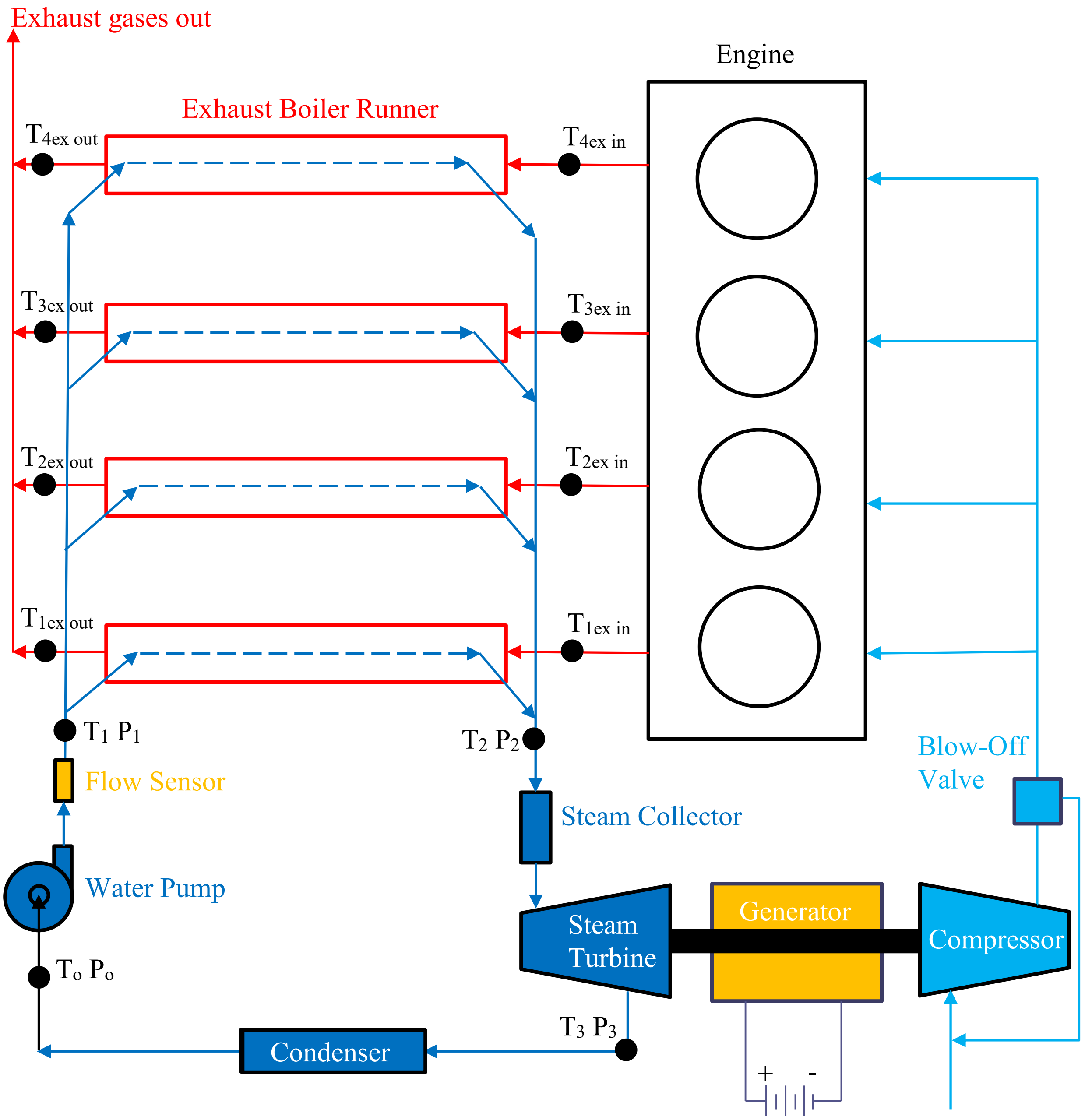

Figure 4.22 Complete Steam-Turbocharger and Generator System Configuration

5. CONCLUSIONS & RECOMMENDATIONS

5.1 Concluding Remarks

The main target of this research was successfully reached and it was clearly confirmed that steam turbocharging is indeed an efficient energy recovery system and that this method could be applied to internal combustion engines with little to no baseline operational disruptions. It was determined that between 3.957 and 9.833 kW of thermal energy could be recovered from the exhaust gases by means of double-pipe heat exchanger with water running through the annular volume in order to recover the wasted heat. From there, the superheated steam was theoretically expanded in a steam turbine to provide a realistic proof of concept by using typical efficiency values found in similar systems. Using a generator to recover the energy from the turbine would mean converting between 0.6552 to 1.4805 kW into useful energy, representing a 2.977 to 7.446% improvement in the engine's thermal efficiency and reduction of 2.891 to 6.930% in *bsfc*. Unfortunately this method would reduce the engine's power density by 13.41% and is therefore suggested for stationary applications where weight is not an issue.

Using the power produced by the turbine to drive a compressor was determined as being the best option for vehicle applications since these results were much more promising. Given the engine's mass flow rates, the energy recovered by the turbine was deemed enough to power a Garrett® GT1548 compressor at pressure ratios ranging from 1.265 to 1.364, which represents supplying the engine with intake air at 26.84 to 36.87 kPa (3.892 to 5.348 psi) above atmospheric. This translates into improvements ranging from 28.99 to 35.00% in engine brake power, leading to an improvement in engine power density of 13.73%.

It is important to note that the baseline and experimental engine power and torque curves were quite similar which confirms that the energy recovery achievable via this system does not impact the engine's performances in any way.

A point that is deemed worthy to highlight was the fact that the magnitude of heat released from the exhaust gases was on average 86.8% and 14.8% higher than the lower and upper bound theoretical predictions, respectively. Yet the trend followed very closely that set by the lower bound values. This significant divergence of the experimental results from theory was attributed to the fact that the Nusselt number is significantly higher in the entrance region of an internal flow since it is thermally developing up to a distance of 10 diameters, which represents 75.3% of the heat exchanger length in this case.

Furthermore, there were no significant variations between the baseline and experimental exhaust temperature variations through the heat exchanger sections, namely a difference of about 3.29% on average or 5.9℃ which is considered to be negligible given the fact that the most recorded exhaust gas temperatures exhibit a variance of about same magnitude during the steady state experiments. What is interesting to note here is that the experiments where water was flowing through the annular volume were the ones that experienced, on average, the smaller temperature difference, which is an additional reason to consider this variation between both sets as being insignificant.

5.2 Suggestions and Future Work

Future work on this subject should first focus on the optimization of the exhaust heat absorption side of the equation. By adding fins inside the exhaust runners, the heat transfer surface area can be greatly enhanced, thus resulting in additional energy recovery. Another subject to be considered, is the possibility of staggering the fins in order to induce additional turbulence in the exhaust system which would contribute towards increasing the convection heat transfer coefficient, thus further increasing the recovered heat. It should be noted that this would eventually lead to increased backpressure of the exhaust system and thus its impact needs to be carefully studied. A brief analysis was done using CFD in order to get a feel as to what kind of impact this would have on the system. As seen in Appendix F, it would seem that the fins added have a negligible impact on the flow, yet by using this added surface area back in the theoretical equations, they could potentially increase the recovered heat by as much as 55.9% or more depending on the engine speed.

Another route that would be interesting to explore, is how the engine’s transient behaviour effects the heat absorption capabilities and performances of this system. Furthermore, the use of an intercooler in order to cool down the compressed air is highly advised in order to gain additional power from this setup. In concluding, a final word of advice for future research in this field would be to make sure to include precise correlation for the friction and heat transfer coefficients for the entrance regions in order to yield more accurate theoretical results.

BIBLIOGRAPHY

[1] J. S. Jadhao, D. G. Thombare and D. S. Sakharale, "Review on Exhaust Gas Heat Recovery for I.C. Engine," *International Journal of Engineering and Innovative Technology,* vol. 2, no. 12, pp. 93-100, 2013.

[2] M. He, X. Zhang, K. Zeng and K. Gao, "A Combined Thermodynamic Cycle Used for Waste Heat Recovery of Internal Combution Engine," *Energy,* vol. 36, pp. 6821-6829, 2011.

[3] A. Büchi, "Combustion machine consisting of a compressor (turbine compressor), a piston engine, and a turbine in sequential arrangement". Germany Patent 204630, 16 November 1905.

[4] S. R. Cikanek and K. E. Bailey, "Regenerative Braking System for a Hybrid Electric Vehicle," *American Control Conference,* vol. 4, pp. 3129-3134, 2002.

[5] B. Rajagopalan and V. Gopal, "Magnetorheological Fluid Based Kinetic Energy Recovery System," *SAE Technical Paper,* Vols. 10.4271/2011-28-0070, 2011.

[6] A. M. Noor, R. C. Puteh and S. Rajoo, "Waste Heat Recovery Technologies in Turbocharged Automotive Engine - A Review," *Journal of Modern Science and Technology,* vol. 2, no. 1, pp. 108-119, 2014.

[7] J. Fu, J. Liu, Y. Yang, C. Ren and G. Zhu, "A New Approach for Exhaust Energy Recovery of Internal Combustion Engine: Steam Turbocharging," *Applied Thermal Engineering,* vol. 52, pp. 150-159, 2013.

[8] Honda Motor Co., Ltd., *Service Manual CBR600F4i,* Tokyo, 2000.

[9] C. R. Ferguson and A. T. Kirkpatrick, *Internal Combustion Engines: Applied Thermosciences*, 2nd ed., New Delhi: Wiley, 2012.

[10] Y. A. Çengel and M. A. Boles, *Thermodynamics: An Engineering Approach*, 6th ed., New York: McGraw-Hill, 2007.

[11] Y. A. Çengel and A. J. Ghajar, *Heat and Mass Transfer: Fundamentals and Applications*, 4th ed., New York: McGraw-Hill, 2011.

[12] R. W. Fox, P. J. Pritchard and A. T. McDonald, *Introduction to Fluid Mechanics*, 7th ed., Hoboken, NJ: Wiley, 2009.

[13] J. John and T. Keith, *Gas Dynamics*, 3rd ed., Upper Saddle River, NJ: Pearson Prentice Hall, 2006.

[14] C.-R. Kuo, S.-W. Hsu, K.-H. Chang and C.-C. Wang, "Analysis of a 50 kW Organic Rankine Cycle System," *Energy,* vol. 36, pp. 5877-5885, 2011.

[15] J. A. Mathias, J. R. Johnston, J. Cao, D. K. Priedeman and R. N. Christensen, "Experimental Testing of Gerotor and Scroll Expanders Used in, and Energetic and Exergetic Modeling of, an Organic Rankine Cycle," *Journal of Energy Resources Technology,* vol. 131, no. 1, pp. 012201(1)-012201(9), 2009.

[16] H. I. H. Saravanamuttoo, G. F. C. Rogers, H. Cohen and P. V. Straznicky, *Gas Turbine Theory*, 6th ed., Harlow, England: Pearson Prentice Hall, 2009.

[17] SuperFlow Technologies Group, *Engine Dynamometer Operator Manual XCONSOLE, SF-902, & RACERS PACK REV: 4.21.2010,* Colorado Springs, 2010.

[18] Honeywell, "Garrett®," [Online]. Available: http://www.turbobygarrett.com/turbobygarrett/sites/default/files/default_images/turbogroup/performance_maps/466755-3comp.jpg. [Accessed 15 March 2016].

[19] V. Babu, *Fundamentals of Gas Dynamics*, 2nd ed., Hoboken, New Jersey: John Wiley & Sons, 2015.

[20] H. Gao, C. Liu, C. He, X. Xu, S. Wu and Y. Li, "Performance Analysis and Working Fluid Selection of a Supercritical Organic Rankine Cycle for Low Grade Waste Heat Recovery," *Energies,* vol. 5, pp. 3233-3247, 2012.

APPENDIX A THEORETICAL ENERGY RECOVERY TABLES

Table A.1 Otto Cycle Preliminary Analysis

T_1 (K)	318.3
P_1 (kPa)	96.0
T_2 (K)	869.8
P_2 (kPa)	3279
T_3 (K)	3518
P_3 (kPa)	13262
T_4 (K)	1682
P_4 (kPa)	507.4
T_e (K)	1178
P_e (kPa)	105
f	0.02363
imep (kPa)	1579
isfc $\left(\frac{\mathbf{kg}}{\mathbf{kW{\cdot}hr}}\right)$	0.1565
ϕ	1.05
LHV (MJ/kg)	44.50
r_c	12.5
n_r	2
η_v	0.95
η_c	0.95
η_{th}	0.5441

Table A.2 Engine Heat Input and Work Output

N (RPM)	2475	4014	6004	6982	8028
$\dot{W}_{in}$ (kW)	5.240	8.498	12.71	14.78	17.00
$\dot{Q}_{in}$ (kW)	35.92	58.26	87.14	101.3	116.5
$\dot{W}_{out}$ (kW)	24.90	40.38	60.39	70.23	80.75
$\dot{Q}_{out}$ (kW)	18.51	30.01	44.89	52.21	60.03
$\dot{W}_{pump}$ (kW)	-0.1114	-0.1806	-0.2702	-0.3142	-0.3613
$\dot{W}_{i}$ (kW)	19.54	31.70	47.41	55.13	63.39

Table A.3 Heat Transfer Analysis Constants

Exhaust Side	
A_s (m^2)	0.05507
D_i (m)	0.03632
L (m)	0.4826
A_x (m^2)	1.036E-3

Water Side	
A_s (m^2)	0.07417
D_i (m)	0.03810
D_o (m)	0.04831
D_h (m)	0.01021
Nu	4.921
h_o	171.7
T_i (K)	358

Table A.4 Engine Exhaust Port Parameters

D_v (m)	0.02
L (m)	0.007
A^* (m^2)	8.796E-4
L/D_v	0.35
C_d	0.55
$A^*_{corrected}$ (m^2)	4.838E-4
A_x (m^2)	1.036E-3
$A_x / A^*_{corrected}$	2.142

Table A.5 Lower Bound Heat Released from Exhaust

N (RPM)	2475	4014	6004	6982	8028
$\dot{m}_{air}$ (kg/s)	0.01235	0.02004	0.02997	0.03485	0.04007
$\dot{m}_{fuel}$ (kg/s)	8.497E-4	1.378E-03	2.061E-03	2.397E-03	2.756E-03
$\dot{m}_{ex}$ (kg/s)	0.01320	0.02141	0.03203	0.03725	0.04283
V_{ex} (m/s)	10.63	17.25	25.80	30.00	34.50
Re	2.492E+03	4.041E+03	6.045E+03	7.030E+03	8.083E+03
f	0.04855	0.04130	0.03644	0.03484	0.03345
Nu	8.343	14.28	20.70	23.58	26.52
$h_i\left(\frac{\mathrm{W}}{\mathrm{m^2 \cdot K}}\right)$	17.94	30.71	44.52	50.70	57.02
T_i (K)	1178	1178	1178	1178	1178
T_s (K)	522	623	707	737	765
T_e (K)	1046	1061	1081	1089	1097
ΔT_{lm} (K)	-587.5	-494.0	-420.7	-394.8	-370.6
$\dot{Q}_{out}$ (kW)	2.321	3.341	4.125	4.409	4.654

Table A.6 Lower Bound Heat Absorbed into Water

N (RPM)	2475	4014	6004	6982	8028
$\dot{Q}_{in}$ (kW)	2.321	3.341	4.125	4.409	4.654
T_i (K)	358	358	358	358	358
T_s (K)	522	623	707	737	765
T_e (K)	517	618	702	732	760
ΔT_{lm} (K)	45.55	65.48	81.02	86.41	91.37

Table A.7 Lower Bound Rankine Circuit Energy Recovery

N (RPM)	2475	4014	6004	6982	8028
$\dot{m}_w$ (kg/s)	8.996E-4	1.196E-3	1.385E-3	1.448E-3	1.507E-3
T_1 (K)			333.1		
P_1 (kPa)			20.00		
T_2 (K)			333.1		
P_2 (kPa)			800.0		
$T_{2.5}$ (K)			358.2		
$P_{2.5}$ (kPa)			800.0		
T_3 (K)	517.0	618.0	702.1	732.0	760.1
P_3 (kPa)			800.0		
T_4 (K)			333.2		
P_4 (kPa)			20.00		
η_p			0.65		
$\dot{W}_p$ (kW)	9.074E-4	1.206E-3	1.397E-3	1.460E-3	1.520E-3
$\dot{Q}_{Kalina}$ (kW)	0.09419	0.1252	0.1450	0.1516	0.1578
$\dot{Q}_{in}$ (kW)	2.321	3.341	4.125	4.409	4.654
$\dot{Q}_{out}$ (kW)	1.853	2.614	3.152	3.338	3.515
η_t			0.7		
$\dot{W}_t$ (kW)	0.3939	0.5974	0.7770	0.8470	0.9170

Table A.8 Lower Bound Otto Cycle Improvements

N (RPM)	2475	4014	6004	6982	8028
$\dot{W}_i$ (kW)	19.54	31.70	47.41	55.13	63.39
η_g			0.9		
$\dot{W}_r$ (kW)	0.3537	0.5366	0.6980	0.7610	0.8239
isfc new $\left(\frac{\text{kg}}{\text{kW}\cdot\text{hr}}\right)$	0.1537	0.1539	0.1542	0.1544	0.1545
isfc improvement (%)	-1.778	-1.665	-1.451	-1.361	-1.283
η_{th} new	0.5539	0.5533	0.5521	0.5516	0.5512
η_{th} improvement (%)	1.810	1.693	1.472	1.380	1.300

Table A.9 Upper Bound Heat Released from Exhaust

N (RPM)	**2475**	**4014**	**6004**	**6982**	**8028**
$\dot{m}_{air}$ **(kg/s)**	0.01235	0.02004	0.02997	0.03485	0.04007
$\dot{m}_{fuel}$ **(kg/s)**	8.497E-4	1.378E-03	2.061E-03	2.397E-03	2.756E-03
$\dot{m}_{ex}$ **(kg/s)**	0.01320	0.02141	0.03203	0.03725	0.04283
V_{ex} **(m/s)**	194.7	194.7	194.7	194.7	194.7
Re	4.561E+04	4.561E+04	4.561E+04	4.561E+04	4.561E+04
f	0.02141	0.02141	0.02141	0.02141	0.02141
Nu	104.0	104.0	104.0	104.0	104.0
$h_i\left(\frac{\mathrm{W}}{\mathrm{m^2\cdot K}}\right)$	223.7	223.7	223.7	223.7	223.7
T_i **(K)**	1178	1178	1178	1178	1178
T_s **(K)**	850	921	960	971	980
T_e **(K)**	870.2	966.9	1029	1048	1064
ΔT_{lm} **(K)**	-109.7	-122.1	-129.1	-131.0	-132.4
$\dot{Q}_{out}$ **(kW)**	5.403	6.013	6.357	6.454	6.522

Table A.10 Upper Bound Heat Absorbed into Water

N (RPM)	**2475**	**4014**	**6004**	**6982**	**8028**
$\dot{Q}_{in}$ **(kW)**	5.403	6.013	6.357	6.454	6.522
T_i **(K)**	358	358	358	358	358
T_s **(K)**	850	921	960	971	980
T_e **(K)**	845	916	955	966	975
ΔT_{lm} **(K)**	106.1	118.1	124.6	126.4	127.9

Table A.11 Upper Bound Rankine Circuit Energy Recovery

N (RPM)	**2475**	**4014**	**6004**	**6982**	**8028**
$\dot{m}_w$ **(kg/s)**	1.644E-3	1.746E-3	1.805E-3	1.816E-3	1.823E-3
T_1 **(K)**	333.1				
P_1 **(kPa)**	20.00				
T_2 **(K)**	333.1				
P_2 **(kPa)**	800.0				
$T_{2.5}$ **(K)**	358.2				
$P_{2.5}$ **(kPa)**	800.0				
T_3 **(K)**	845.0	916.1	955.0	966.0	975.0
P_3 **(kPa)**	800.0				
T_4 **(K)**	333.2	369.7	388.3	393.6	398.0
P_4 **(kPa)**	20.00				
η_p	0.65				
$\dot{W}_p$ **(kW)**	1.658E-3	1.762E-3	1.820E-3	1.831E-3	1.840E-3
$\dot{Q}_{Kalina}$ **(kW)**	0.1721	0.1828	0.1890	0.1901	0.1908
$\dot{Q}_{in}$ **(kW)**	5.403	6.013	6.357	6.454	6.522
$\dot{Q}_{out}$ **(kW)**	3.888	4.239	4.447	4.492	4.524
η_t	0.7				
$\dot{W}_t$ **(kW)**	1.176	1.365	1.477	1.505	1.526

Table A.12 Upper Bound Otto Cycle Improvements

N (RPM)	**2475**	**4014**	**6004**	**6982**	**8028**
$\dot{W}_i$ **(kW)**	19.54	31.70	47.41	55.13	63.39
η_g	0.9				
$\dot{W}_r$ **(kW)**	1.057	1.227	1.328	1.353	1.372
***isfc* new** $\left(\frac{\text{kg}}{\text{kW}\cdot\text{hr}}\right)$	0.1485	0.1507	0.1522	0.1528	0.1532
***isfc* improvement (%)**	-5.131	-3.727	-2.725	-2.352	-2.118
η_{th} **new**	0.5735	0.5652	0.5593	0.5572	0.5559
η_{th} **improvement (%)**	5.408	3.871	2.801	2.409	2.164

APPENDIX B THEORETICAL STEAM TURBINE POTENTIAL TABLES

Table B.1 Lower Bound Heat Released from Exhaust –Turbo Otto-Rankine

N (RPM)	**2475**	**4014**	**6004**	**6982**	**8028**
P_{atm} **(kPa)**	101.3				
η_m	0.95				
η_c	0.8				
P_r	1.250	1.216	1.187	1.175	1.164
P_1 **(kPa)**	126.6	123.1	120.2	119.0	117.9
T_1 **(K)**	345.3	341.8	338.6	337.4	336.1
$\dot{W}_c$ **(kW)**	0.3419	0.4703	0.6011	0.6487	0.6975
$\dot{m}_{air}$ **(kg/s)**	0.01501	0.02393	0.03528	0.04076	0.04662
$\dot{m}_{fuel}$ **(kg/s)**	1.033E-3	1.646E-03	2.427E-03	2.803E-03	3.206E-03
$\dot{m}_{ex}$ **(kg/s)**	0.01605	0.02558	0.03771	0.04356	0.04983
V_{ex} **(m/s)**	12.77	19.27	28.41	32.83	37.55
Re	2.993E+03	4.516E+03	6.658E+03	7.692E+03	8.798E+03
f	0.04560	0.03987	0.03540	0.03393	0.03264
Nu	10.41	15.89	22.51	25.44	28.44
$h_i\left(\frac{\text{W}}{\text{m}^2\cdot\text{K}}\right)$	22.39	34.17	48.40	54.71	61.16
T_i **(K)**	1146	1148	1150	1151	1151
T_s **(K)**	550	634	712	740	766
T_e **(K)**	1022	1040	1061	1069	1076
ΔT_{lm} **(K)**	-531.0	-457.3	-391.1	-367.7	-345.6
$\dot{Q}_{out}$ **(kW)**	2.619	3.443	4.169	4.430	4.656

Table B.2 Lower Bound Heat Absorbed into Water –Turbo Otto-Rankine

N (RPM)	**2475**	**4014**	**6004**	**6982**	**8028**
$\dot{Q}_{in}$ (kW)	2.619	3.443	4.169	4.430	4.656
T_i (K)	358	358	358	358	358
T_s (K)	550	634	712	740	766
T_e (K)	545	629	707	735	761
ΔT_{lm} (K)	51.25	67.56	81.92	86.94	91.55

Table B.3 Lower Bound Rankine Circuit Energy Recovery –Turbo Otto-Rankine

N (RPM)	**2475**	**4014**	**6004**	**6982**	**8028**
$\dot{m}_w$ (kg/s)	9.920E-4	1.221E-3	1.400E-3	1.453E-3	1.505E-3
T_1 (K)			333.1		
P_1 (kPa)			20.00		
T_2 (K)			333.1		
P_2 (kPa)			800.0		
$T_{2.5}$ (K)			358.2		
$P_{2.5}$ (kPa)			800.0		
T_3 (K)	545.0	628.9	707.0	735.1	761.0
P_3 (kPa)			800.0		
T_4 (K)			333.2		
P_4 (kPa)			20.00		
η_p			0.65		
$\dot{W}_p$ (kW)	1.001E-3	1.232E-3	1.412E-3	1.466E-3	1.518E-3
$\dot{Q}_{Kalina}$ (kW)	0.1039	0.1278	0.1466	0.1522	0.1576
$\dot{Q}_{in}$ (kW)	2.619	3.443	4.169	4.430	4.656
$\dot{Q}_{out}$ (kW)	2.080	2.683	3.193	3.354	3.512
η_t			0.7		
$\dot{W}_t$ (kW)	0.4499	0.6191	0.7910	0.8540	0.9170

Table B.4 Engine Heat Input and Work Output–Turbo Otto-Rankine

N (RPM)	**2475**	**4014**	**6004**	**6982**	**8028**
$\dot{W}_{in}$ **(kW)**	6.909	10.90	15.92	18.32	20.88
$\dot{Q}_{in}$ **(kW)**	43.65	69.59	102.6	118.5	135.6
$\dot{W}_{out}$ **(kW)**	30.89	49.11	72.22	70.23	95.25
$\dot{Q}_{out}$ **(kW)**	22.63	36.04	53.10	61.31	70.12
$\dot{W}_{pump}$ **(kW)**	0.2670	0.3641	0.4575	0.4885	0.5193
$\dot{W}_{i}$ **(kW)**	24.25	38.57	56.76	65.51	74.89

Table B.5 Lower Bound Otto Cycle Improvements –Turbo Otto-Rankine

N (RPM)	**2475**	**4014**	**6004**	**6982**	**8028**
$\dot{W}_{i}$ **(kW)**	19.54	31.70	47.41	55.13	63.39
$\dot{W}_{i}$ **new (kW)**	24.25	38.57	56.76	65.51	74.89
$\dot{W}_{i}$ **improvement (%)**	24.09	21.70	19.72	18.82	18.13
***imep* new (kPa)**	1959	1922	1891	1877	1866
***isfc* new** $\left(\frac{\text{kg}}{\text{kW·hr}}\right)$	0.1533	0.1536	0.1539	0.1540	0.1541
***isfc* improvement (%)**	-2.042	-1.843	-1.661	-1.583	-1.513
η_{th} **new**	0.5555	0.5543	0.5533	0.5528	0.5524
η_{th} **improvement (%)**	2.091	1.877	1.689	1.608	1.536

Table B.6 Upper Bound Heat Released from Exhaust –Turbo Otto-Rankine

N (RPM)	**2475**	**4014**	**6004**	**6982**	**8028**
P_{atm} **(kPa)**	101.3				
η_m	0.95				
η_c	0.8				
P_r	1.564	1.424	1.316	1.281	1.251
P_1 **(kPa)**	158.4	144.3	133.4	129.8	126.8
T_1 **(K)**	376.4	363.0	352.3	348.6	345.5
$\dot{W}_c$ **(kW)**	0.8867	1.022	1.085	1.102	1.117
$\dot{m}_{air}$ **(kg/s)**	0.01725	0.02641	0.03762	0.04302	0.04876
$\dot{m}_{fuel}$ **(kg/s)**	1.186E-3	1.816E-03	2.587E-03	2.958E-03	3.353E-03
$\dot{m}_{ex}$ **(kg/s)**	0.01843	0.02822	0.04020	0.04597	0.05211
V_{ex} **(m/s)**	190.7	191.2	191.6	191.8	191.9
Re	4.468E+04	4.480E+04	4.490E+04	4.494E+04	4.497E+04
f	0.02151	0.02149	0.02148	0.02148	0.02148
Nu	102.4	102.6	102.8	102.8	102.9
$h_i\left(\frac{\mathrm{W}}{\mathrm{m}^2\cdot\mathrm{K}}\right)$	220.1	220.5	221.0	221.1	221.2
T_i **(K)**	1131	1137	1142	1144	1146
T_s **(K)**	847	911	942	952	960
T_e **(K)**	876	968	1018	1034	1048
ΔT_{lm} **(K)**	-110.8	-122.0	-127.6	-128.9	-130.1
$\dot{Q}_{out}$ **(kW)**	5.370	5.926	6.211	6.279	6.341

Table B.7 Upper Bound Heat Absorbed into Water –Turbo Otto-Rankine

N (RPM)	**2475**	**4014**	**6004**	**6982**	**8028**
$\dot{Q}_{in}$ **(kW)**	5.370	5.926	6.211	6.279	6.341
T_i **(K)**	358	358	358	358	358
T_s **(K)**	847	911	942	952	960
T_e **(K)**	842	906	937	947	955
ΔT_{lm} **(K)**	105.6	116.4	121.6	123.3	124.6

Table B.8 Upper Bound Rankine Circuit Energy Recovery –Turbo Otto-Rankine

N (RPM)	**2475**	**4014**	**6004**	**6982**	**8028**
$\dot{m}_w$ **(kg/s)**	1.640E-4	1.741E-3	1.780E-3	1.788E-3	1.796E-3
T_1 **(K)**	333.1				
P_1 **(kPa)**	20.00				
T_2 **(K)**	333.1				
P_2 **(kPa)**	800.0				
$T_{2.5}$ **(K)**	358.2				
$P_{2.5}$ **(kPa)**	800.0				
T_3 **(K)**	842.0	905.9	938.0	947.1	955.1
P_3 **(kPa)**	800				
T_4 **(K)**	335.1	365.0	380.1	384.0	387.9
P_4 **(kPa)**	20.00				
η_p	0.65				
$\dot{W}_p$ **(kW)**	1.655E-3	1.756E-3	1.795E-3	1.803E-3	1.812E-3
$\dot{Q}_{Kalina}$ **(kW)**	0.1718	0.1823	0.1864	0.1872	0.1881
$\dot{Q}_{in}$ **(kW)**	5.370	5.926	6.211	6.279	6.341
$\dot{Q}_{out}$ **(kW)**	3.875	4.211	4.358	4.390	4.426
η_t	0.7				
$\dot{W}_t$ **(kW)**	1.169	1.344	1.428	1.449	1.470

Table B.9 Upper Bound Otto Cycle Improvements –Turbo Otto-Rankine

N (RPM)	**2475**	**4014**	**6004**	**6982**	**8028**
$\dot{W}_i$ **(kW)**	19.54	31.70	47.41	55.13	63.39
$\dot{W}_i$ **new (kW)**	28.32	43.07	60.99	69.60	78.75
$\dot{W}_i$ **improvement (%)**	44.96	35.87	28.65	26.24	24.23
imep **new (kPa)**	2289	2146	2032	1994	1962
isfc **new** $\left(\frac{\text{kg}}{\text{kW}\cdot\text{hr}}\right)$	0.1507	0.1518	0.1527	0.1530	0.1533
isfc **improvement (%)**	-3.698	-3.022	-2.439	-2.236	-2.059
η_{th} **new**	0.5650	0.5610	0.5577	0.5565	0.5555
η_{th} **improvement (%)**	3.847	3.116	2.500	2.287	2.102

APPENDIX C EXPERIMENTAL ENERGY RECOVERY

Table C.1 Experimental Engine Heat Input and Work Output

N (RPM)	2475	4014	6004	6982	8028
$\dot{m}_{fuel}$ (kg/s)	8.497E-4	1.378E-03	2.061E-03	2.397E-03	2.756E-03
$\dot{Q}_{in}$ (kW)	35.92	58.26	87.14	101.3	116.5
$\dot{W}_b$ (kW)	8.80	19.44	32.34	36.39	49.74
$bmep$ (kPa)	711.1	968.5	1077.2	1042.4	1239.1
$bsfc\ \left(\frac{\text{kg}}{\text{kW}\cdot\text{hr}}\right)$	0.3476	0.2552	0.2294	0.2371	0.1995
η_{th}	0.2450	0.3336	0.3711	0.3592	0.4269

Table C.2 Experimental Heat Released from Exhaust

N (RPM)	2475	4014	6004	6982	8028
T_i (K)	851.0	897.7	869.4	911.7	902.1
T_e (K)	633.6	717.1	683.0	745.9	735.6
ΔT (K)	217.4	180.6	186.4	165.8	166.5
$\dot{Q}_{out}$ (kW)	3.957	5.332	8.231	8.514	9.833

Table C.3 Experimental Heat Absorbed into Water

N (RPM)	2475	4014	6004	6982	8028
T_i (K)	289.0	289.5	289.9	288.7	286.5
P_e (kPa)	753.2	755.1	769.8	782.1	786.4
T_e (K)	403.3	409.1	420.1	425.1	438.1
ΔT (K)	114.3	119.6	130.2	136.4	151.6
$\dot{m}_{water}$ (kg/s)	8.208E-03	1.044E-02	1.482E-02	1.446E-02	1.393E-02
$\dot{Q}_{in}$ (kW)	3.943	5.247	8.111	8.287	8.874

Table C.4 Experimental Rankine Circuit Potential Energy Recovery

N (RPM)	**2475**	**4014**	**6004**	**6982**	**8028**
$\dot{m}_w$ (kg/s)	1.347E-3	1.800E-3	2.784E-3	2.849E-3	3.043E-3
T_1 (K)	333.1				
P_1 (kPa)	20.00				
T_2 (K)	333.1				
P_2 (kPa)	800.0				
$T_{2.5}$ (K)	358.2				
$P_{2.5}$ (kPa)	800.0				
T_3 (K)	675.2				
P_3 (kPa)	800.0				
T_4 (K)	333.2				
P_4 (kPa)	20.00				
η_p	0.65				
$\dot{W}_p$ (kW)	1.358E-3	1.815E-3	2.808E-3	2.873E-3	3.069E-3
$\dot{Q}_{Kalina}$ (kW)	0.1410	0.1884	0.2915	0.2983	0.3186
$\dot{Q}_{in}$ (kW)	3.943	5.247	8.111	8.287	8.874
$\dot{Q}_{out}$ (kW)	3.027	4.046	6.258	6.404	6.840
η_t	0.7				
$\dot{W}_t$ (kW)	0.7280	0.9731	1.505	1.540	1.645

Table C.5 Experimental Potential Improvements

N (RPM)	**2475**	**4014**	**6004**	**6982**	**8028**
$\dot{W}_b$ (kW)	8.80	19.44	32.34	36.39	49.74
η_g	0.9				
$\dot{W}_r$ (kW)	0.6552	0.87579	1.3545	1.386	1.4805
***bsfc* new $\left(\frac{\text{kg}}{\text{kW}\cdot\text{hr}}\right)$**	0.3235	0.2442	0.2202	0.2284	0.1937
***bsfc* improvement (%)**	-6.930	-4.311	-4.020	-3.669	-2.891
η_{th} new	0.2632	0.3487	0.3867	0.3729	0.4396
η_{th} improvement (%)	7.446	4.506	4.189	3.809	2.977

APPENDIX D EXPERIMENTAL STEAM TURBINE POTENTIAL OUTPUT

Table D.1 Experimental Engine Potential Heat Input and Work Output–Turbo Otto-Rankine

N (RPM)	2475	4014	6004	6982	8028
P_{atm} (kPa)			101.3		
η_m			0.95		
η_c			0.8		
P_r	1.364	1.308	1.317	1.283	1.265
P_1 (kPa)	138.1	132.5	133.4	130.0	128.2
T_1 (K)	357.1	351.4	352.4	348.8	346.9
$\dot{W}_c$ (kW)	0.5533	0.7396	1.144	1.170	1.250
$\dot{m}_{air}$ (kg/s)	0.01668	0.02636	0.03960	0.04533	0.05169
$\dot{m}_{fuel}$ (kg/s)	1.147E-03	1.813E-03	2.723E-03	3.117E-03	3.555E-03
$\dot{Q}_{in}$ (kW)	48.50	76.64	115.1	131.8	150.3
$bsfc$ $\left(\frac{\text{kg}}{\text{kW·hr}}\right)$	0.3476	0.2552	0.2294	0.2371	0.1995
η_{th}	0.2450	0.3336	0.3711	0.3592	0.4269
bmep new(kPa)	960.0	1274	1423	1356	1598

Table D.2 Experimental Potential Improvements –Turbo Otto-Rankine

N (RPM)	2475	4014	6004	6982	8028
$\dot{W}_b$ (kW)	8.80	19.44	32.34	36.39	49.74
$\dot{W}_b$ new (kW)	11.88	25.57	42.71	47.34	64.16
$\dot{W}_b$ improvement (%)	35.00	31.53	32.07	30.09	28.99

APPENDIX E PARTS CAD DRAWINGS

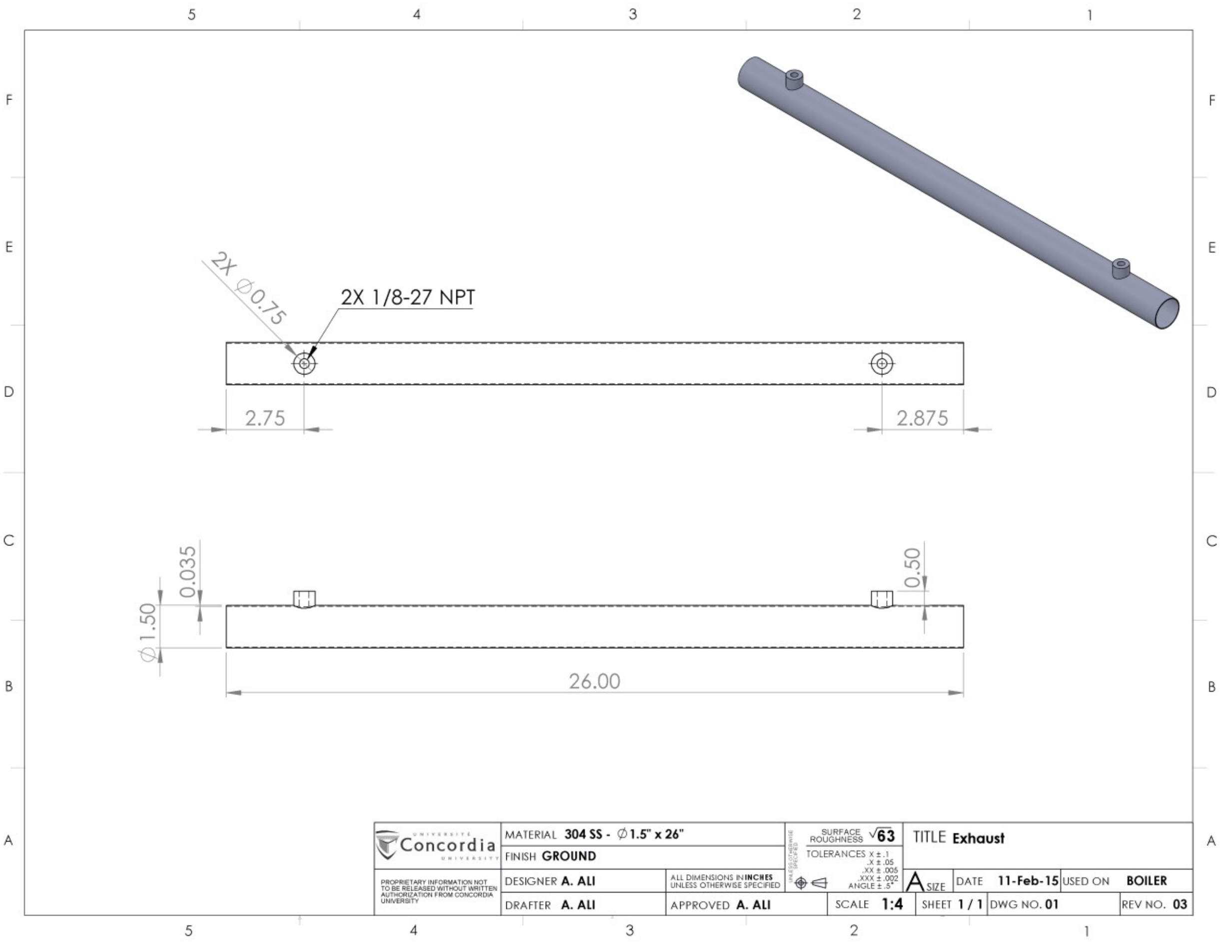

Figure E.1 CAD Drawing of Exhaust

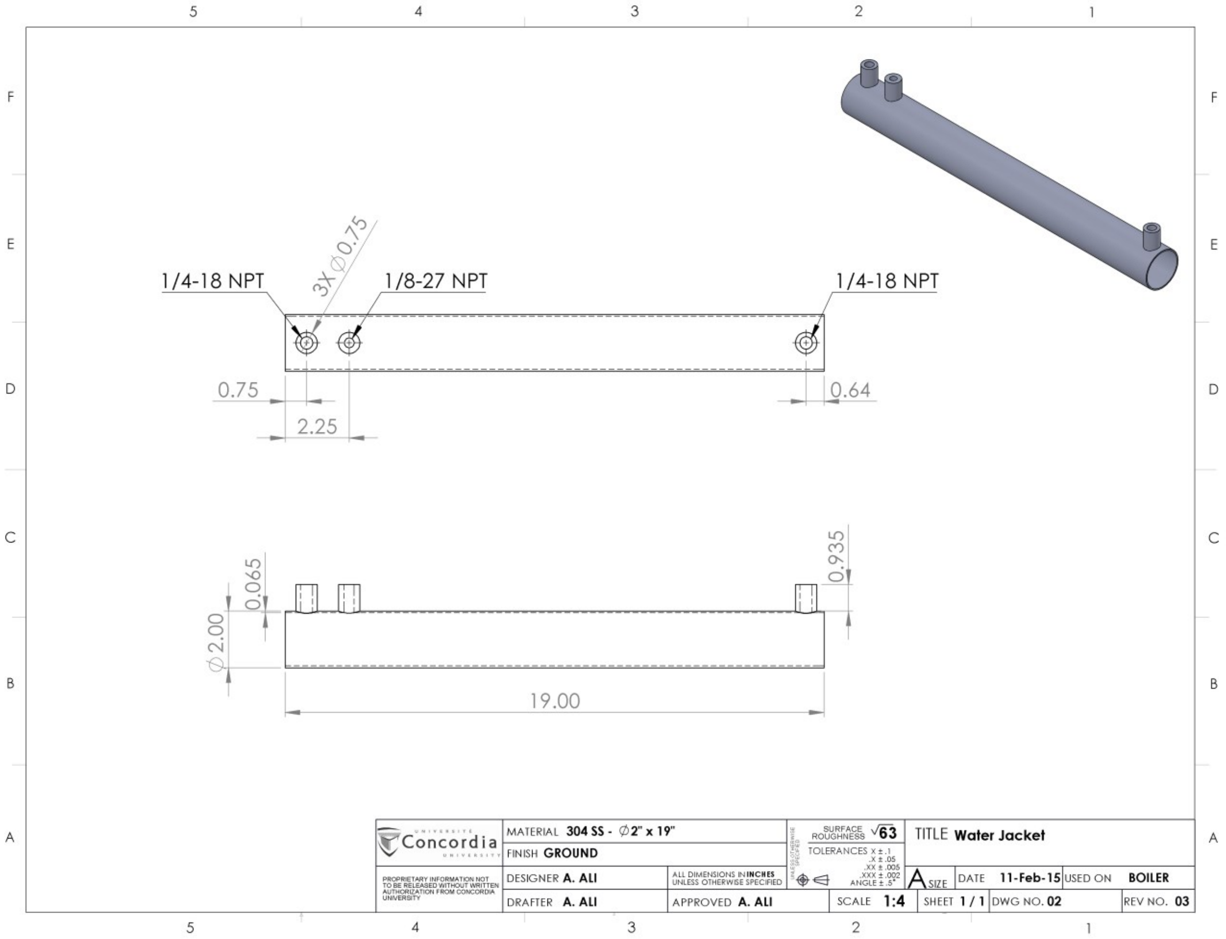

MATERIAL 304 SS - ∅2" x 19"
FINISH GROUND
SURFACE ROUGHNESS √63
TOLERANCES X ± .1 .X ± .05 .XX ± .005 .XXX ± .002 ANGLE ± .5°
UNLESS OTHERWISE SPECIFIED
TITLE Water Jacket
PROPRIETARY INFORMATION NOT TO BE RELEASED WITHOUT WRITTEN AUTHORIZATION FROM CONCORDIA UNIVERSITY
DESIGNER A. ALI
ALL DIMENSIONS IN INCHES UNLESS OTHERWISE SPECIFIED
A SIZE
DATE 11-Feb-15
USED ON BOILER
DRAFTER A. ALI
APPROVED A. ALI
SCALE 1:4
SHEET 1 / 1
DWG NO. 02
REV NO. 03

Figure E.2 CAD Drawing of Water Jacket

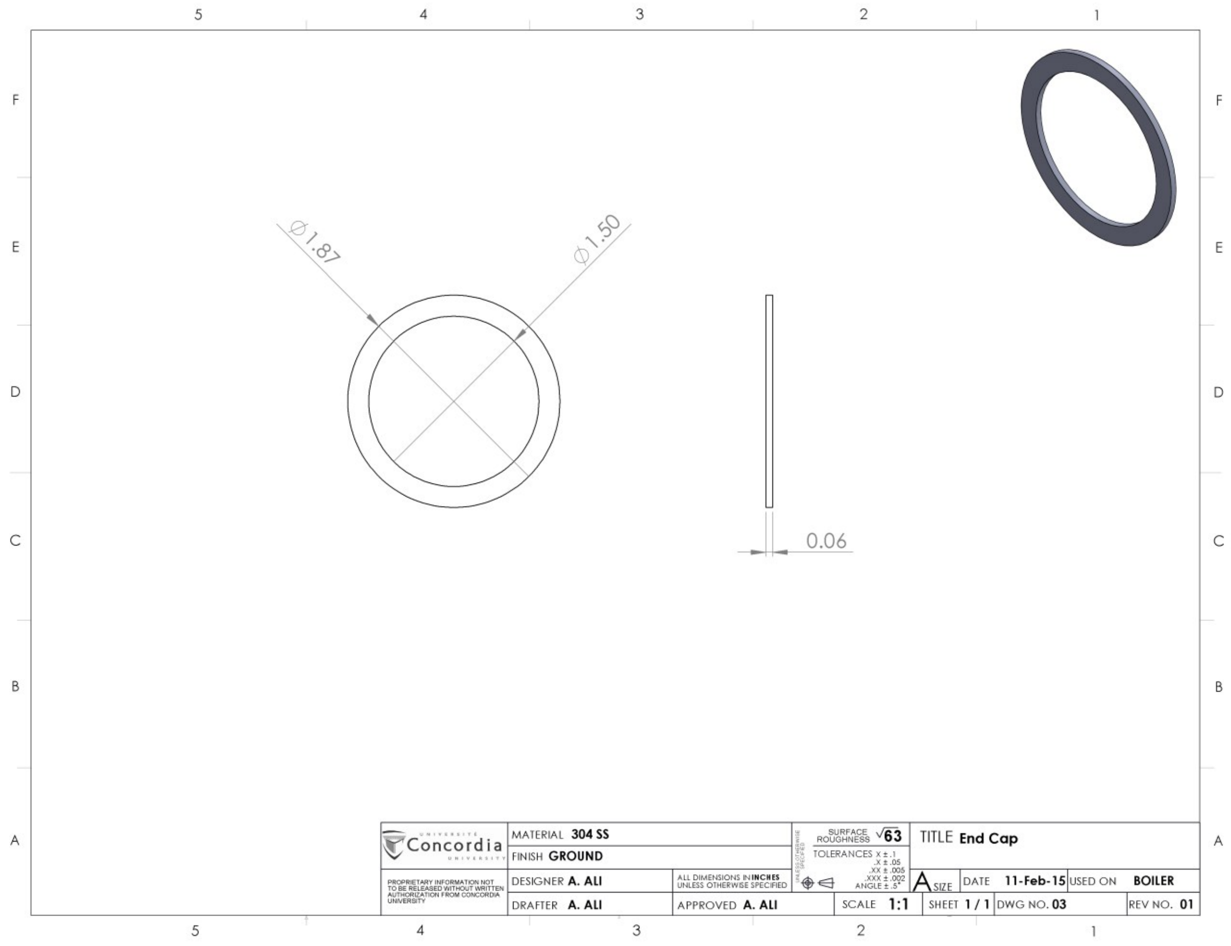

Figure E.3 CAD Drawing of End Cap

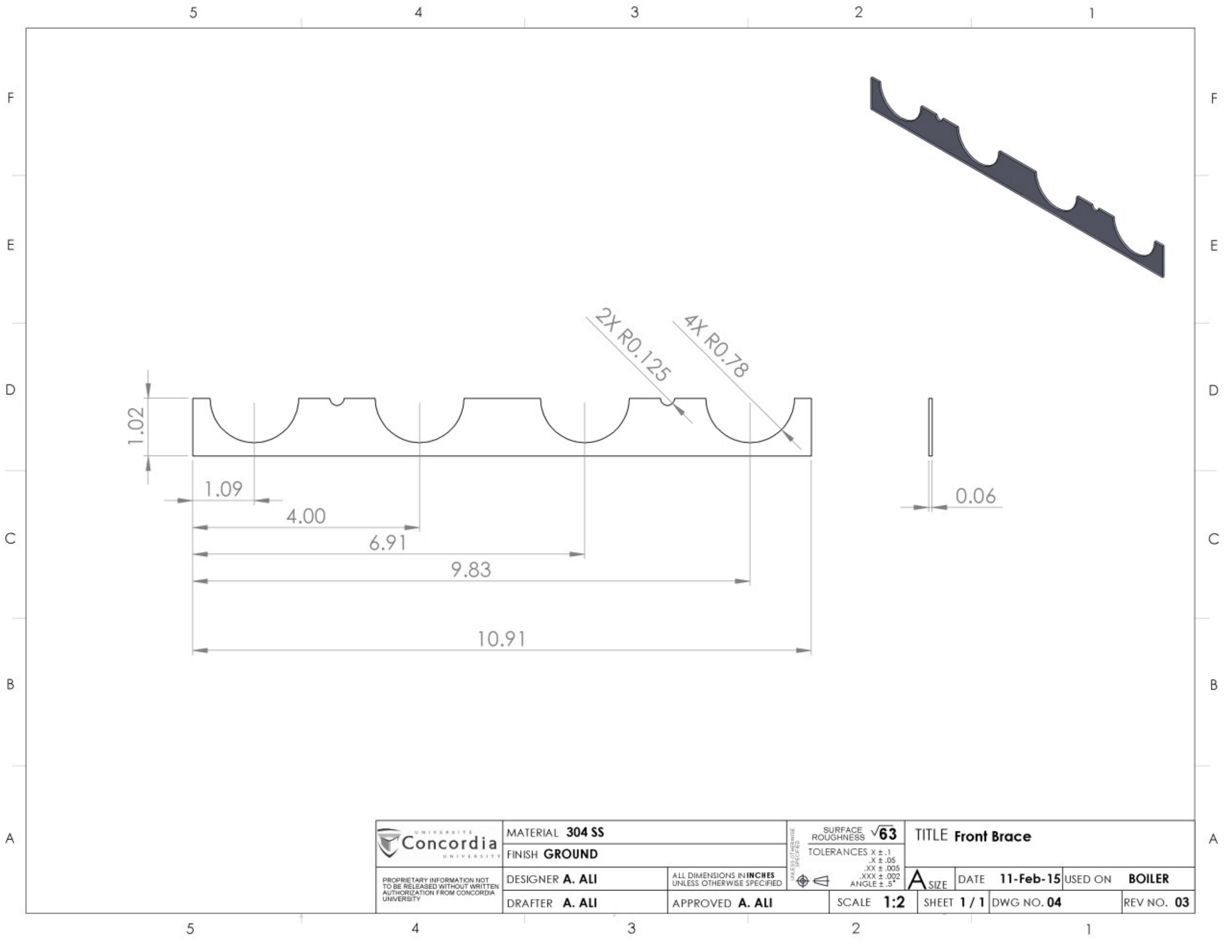

Figure E.4 CAD Drawing of Front Brace

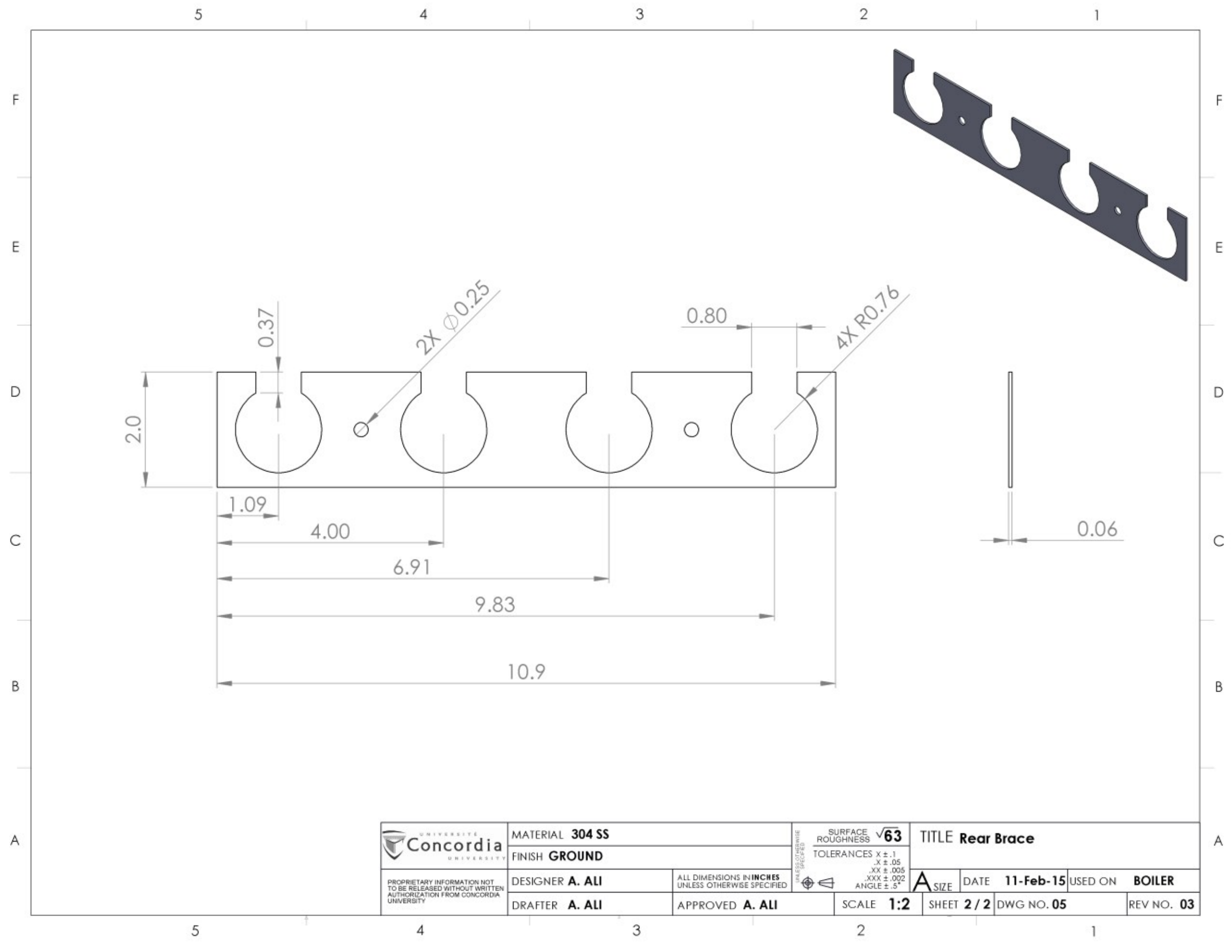

Figure E.5 CAD Drawing of Rear Brace

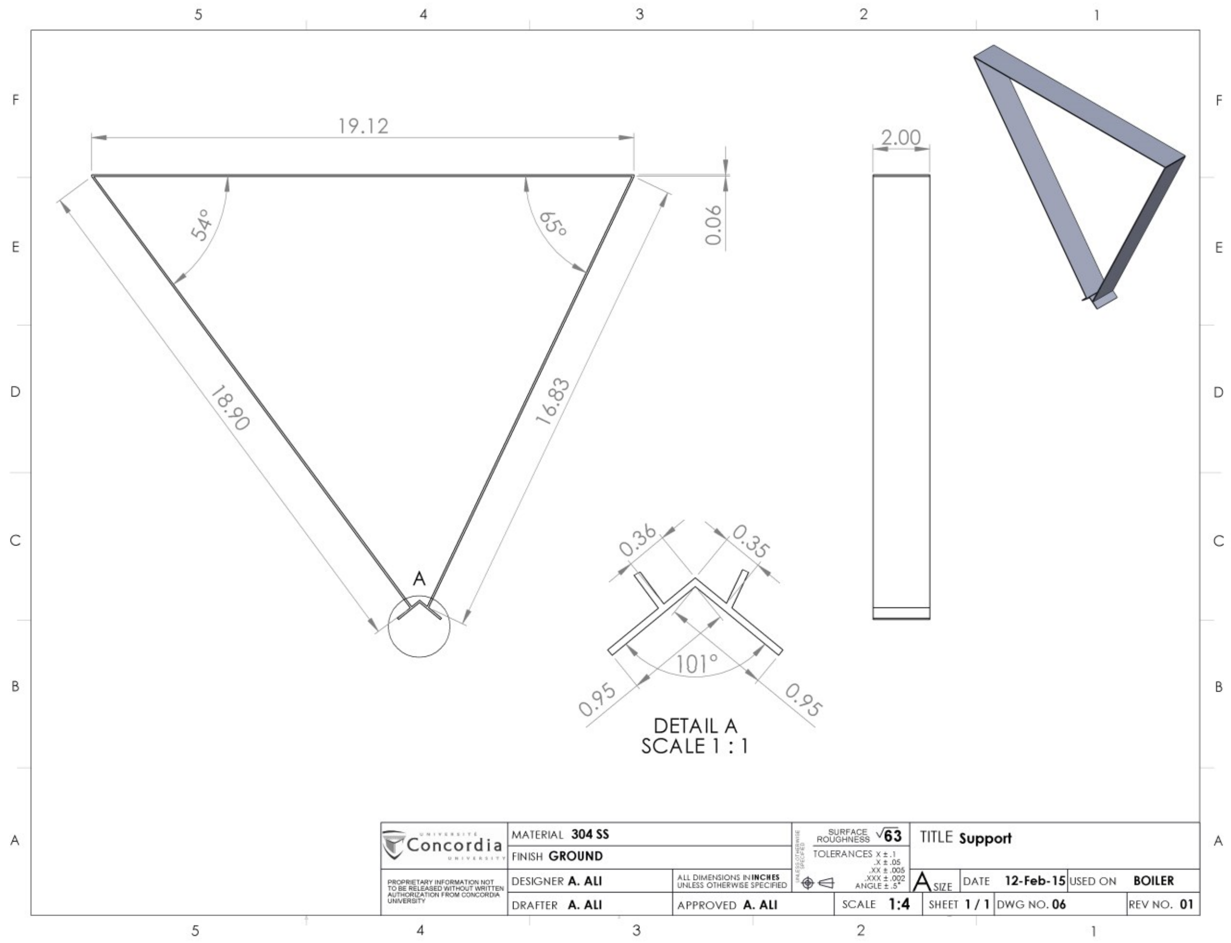

Figure E.6 CAD Drawing of Support

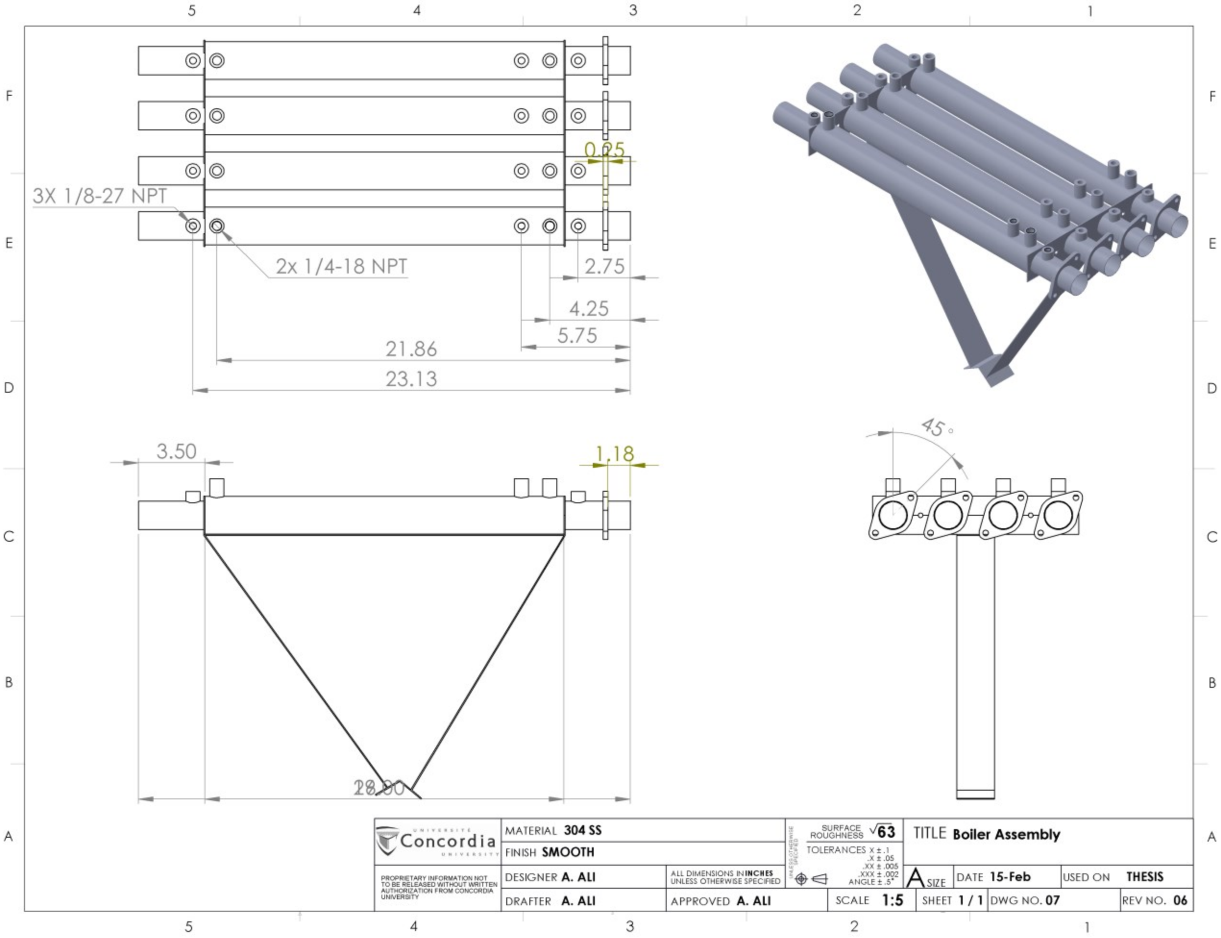

Concordia University
PROPRIETARY INFORMATION NOT TO BE RELEASED WITHOUT WRITTEN AUTHORIZATION FROM CONCORDIA UNIVERSITY
MATERIAL **304 SS**
FINISH **SMOOTH**
DESIGNER **A. ALI**
DRAFTER **A. ALI**
ALL DIMENSIONS IN **INCHES** UNLESS OTHERWISE SPECIFIED
APPROVED **A. ALI**
UNLESS OTHERWISE SPECIFIED
SURFACE ROUGHNESS √**63**
TOLERANCES X ± .1
.X ± .05
.XX ± .005
.XXX ± .002
ANGLE ± .5°
SCALE **1:5**
TITLE **Boiler Assembly**
A SIZE
DATE **15-Feb**
USED ON **THESIS**
SHEET **1 / 1**
DWG NO. **07**
REV NO. **06**

Figure E.7 CAD Drawing of Boiler Assembly

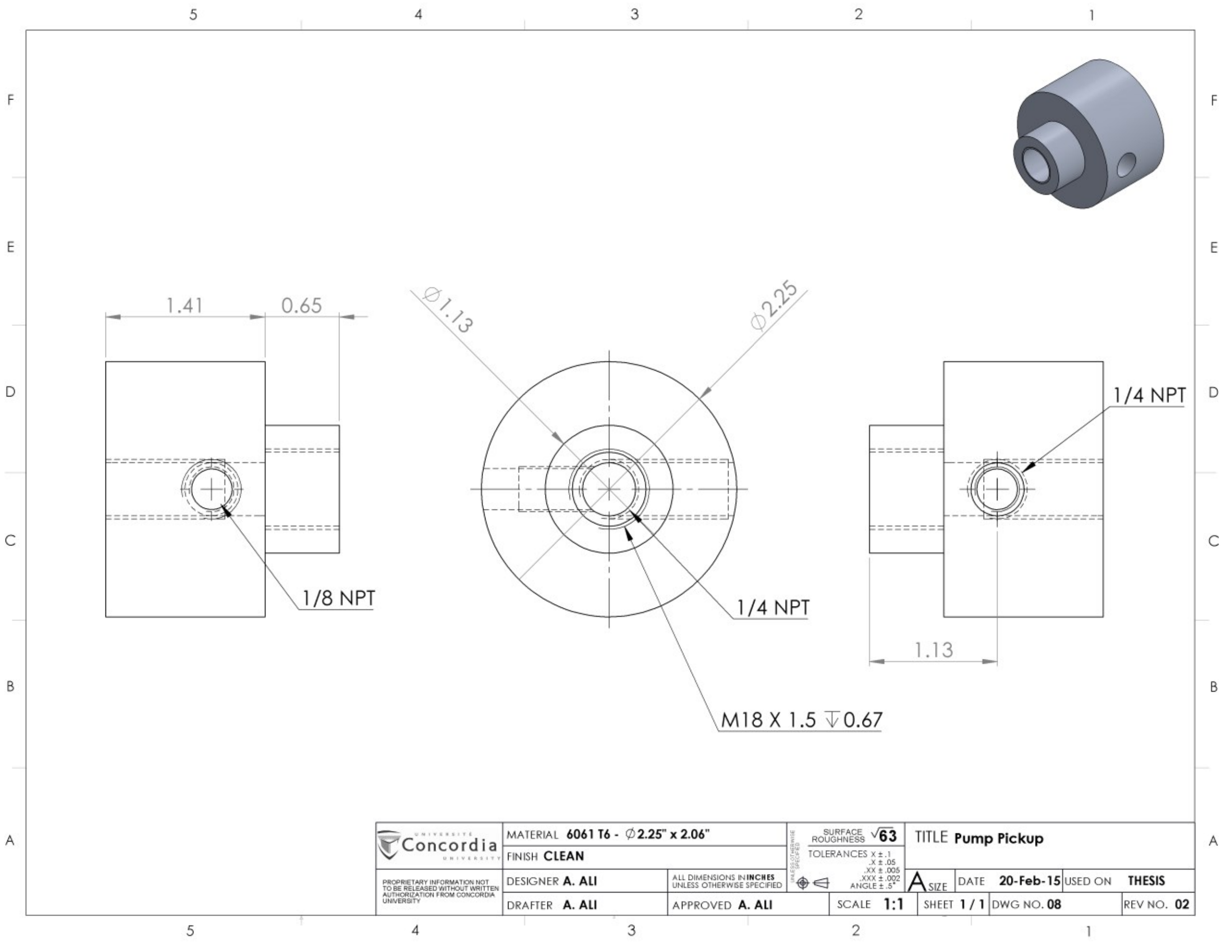

Figure E.8 CAD Drawing of Pump Pickup

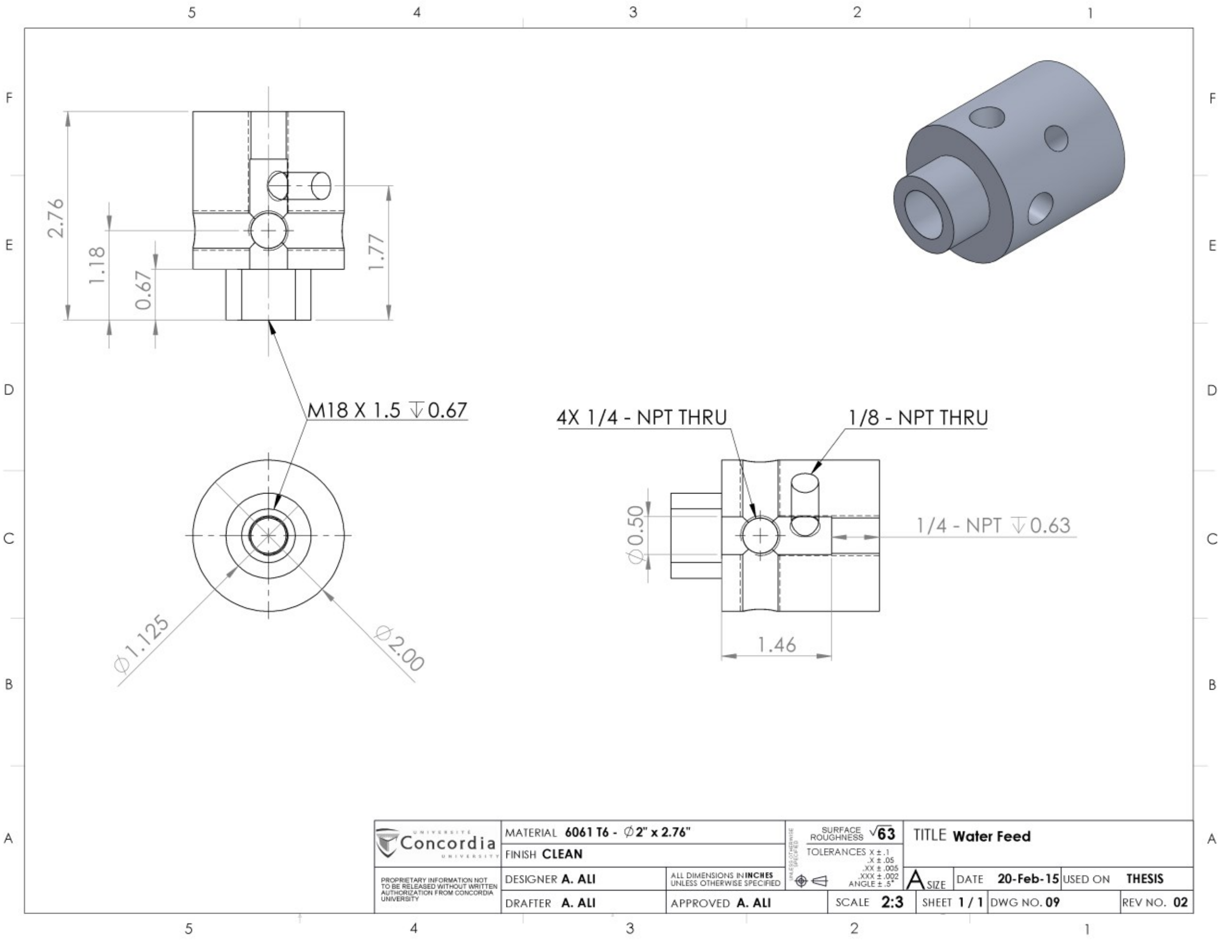

Figure E.9 CAD Drawing of Water Feed

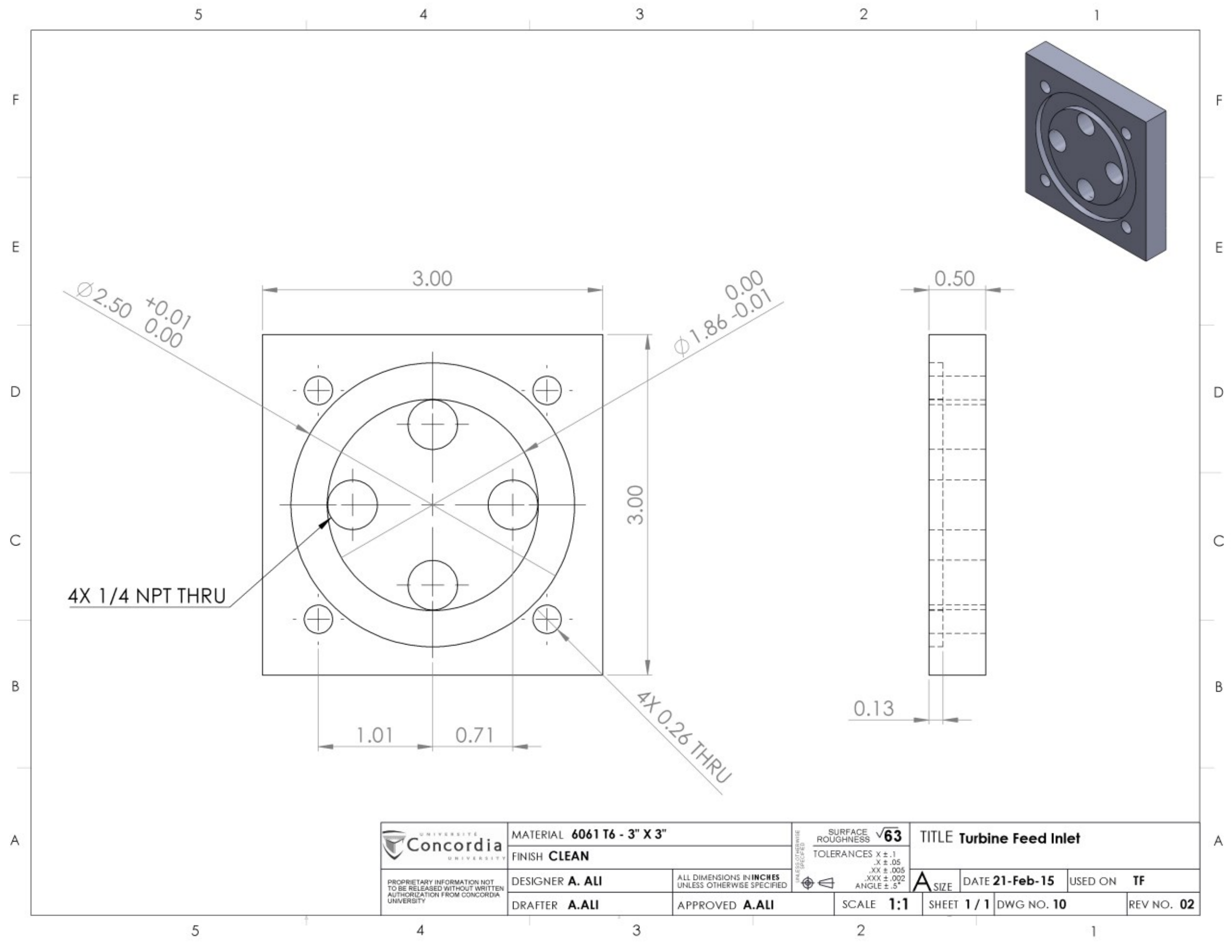

Figure E.10 CAD Drawing of Turbine Feed Inlet

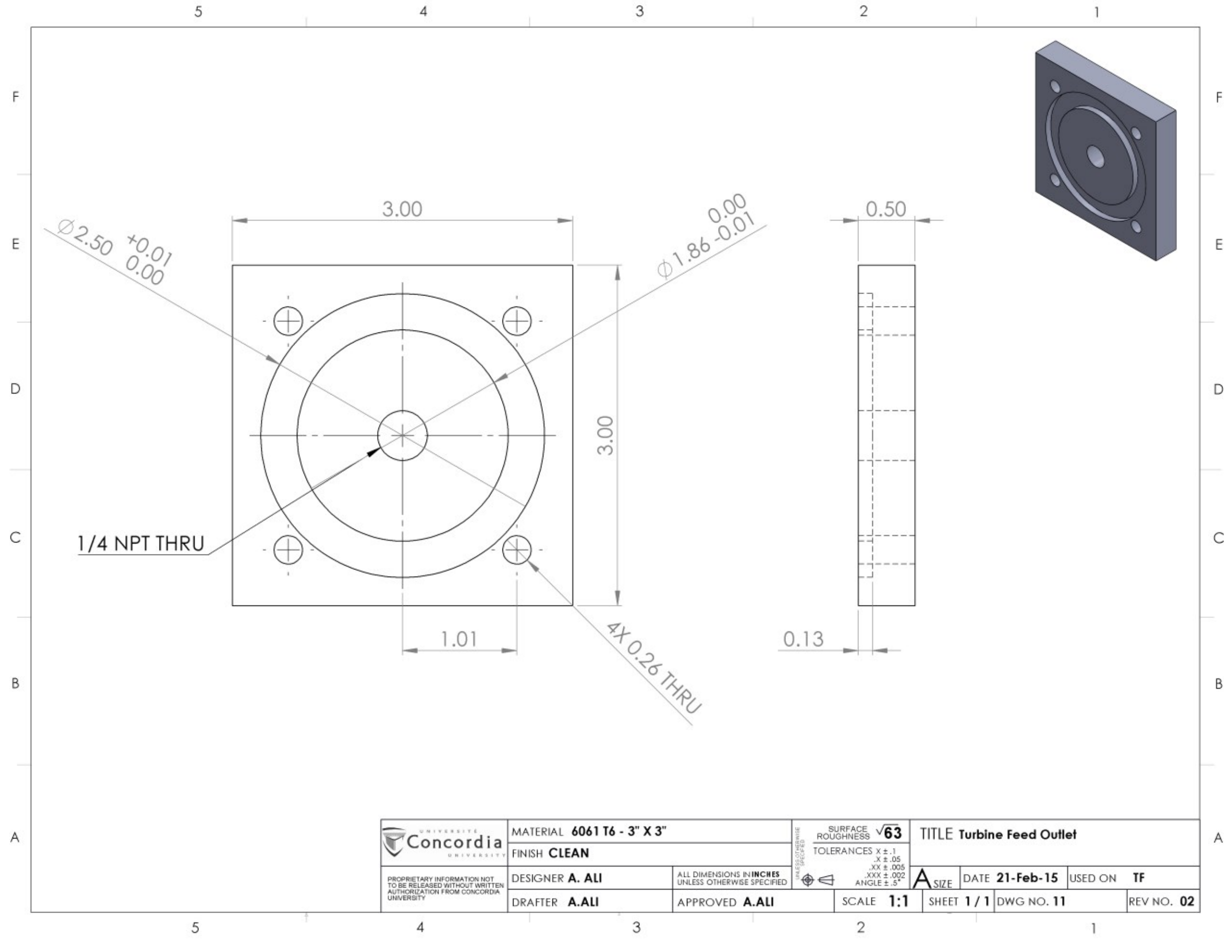

Figure E.11 CAD Drawing of Turbine Feed Outlet

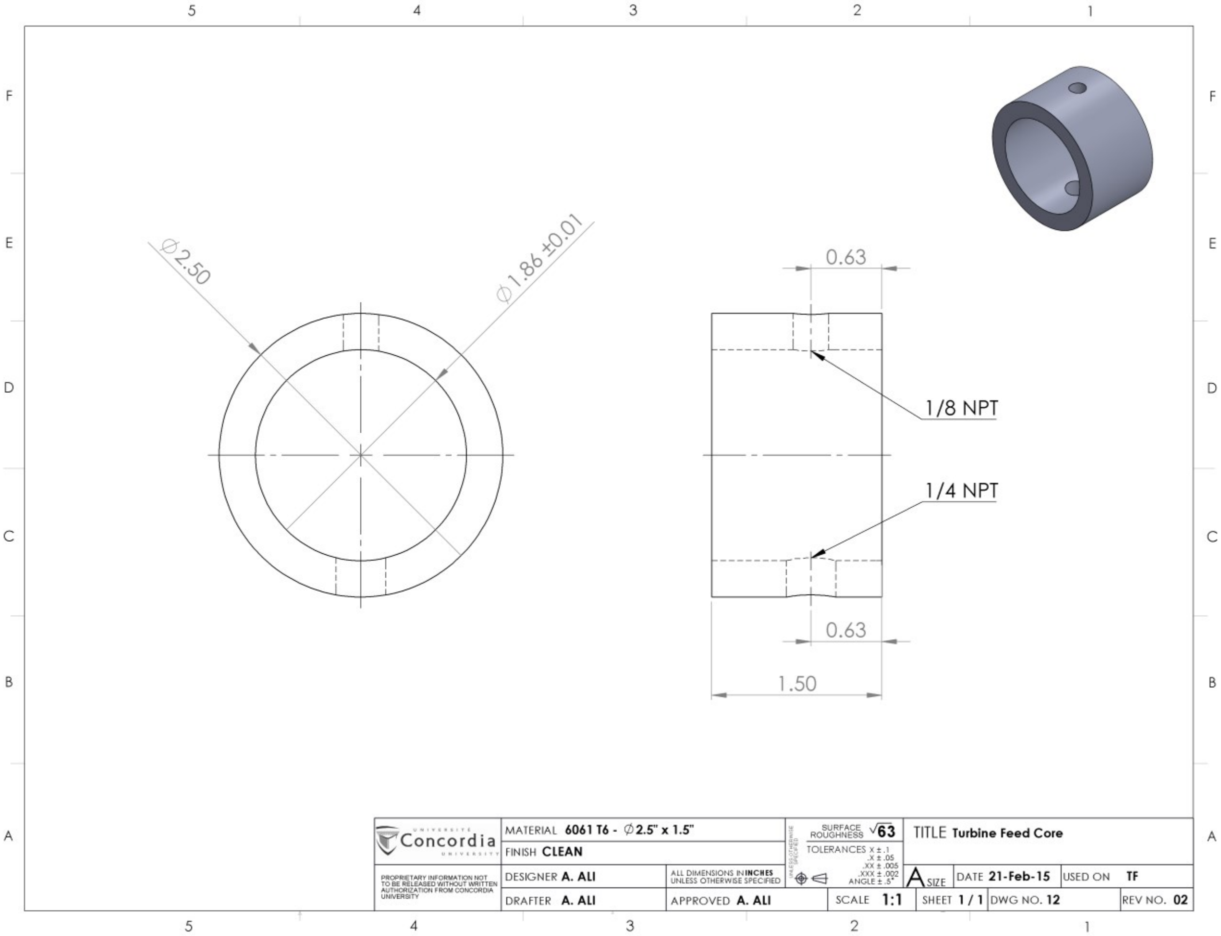

MATERIAL 6061 T6 - ⌀2.5" x 1.5"
FINISH CLEAN
PROPRIETARY INFORMATION NOT TO BE RELEASED WITHOUT WRITTEN AUTHORIZATION FROM CONCORDIA UNIVERSITY
DESIGNER A. ALI
DRAFTER A. ALI
ALL DIMENSIONS IN INCHES UNLESS OTHERWISE SPECIFIED
APPROVED A. ALI
SURFACE ROUGHNESS √63
UNLESS OTHERWISE SPECIFIED
TOLERANCES X ± .1 .X ± .05 .XX ± .005 .XXX ± .002 ANGLE ± .5°
SCALE 1:1
TITLE Turbine Feed Core
A SIZE
DATE 21-Feb-15
USED ON TF
SHEET 1 / 1
DWG NO. 12
REV NO. 02

Figure E.12 CAD Drawing of Turbine Feed Core

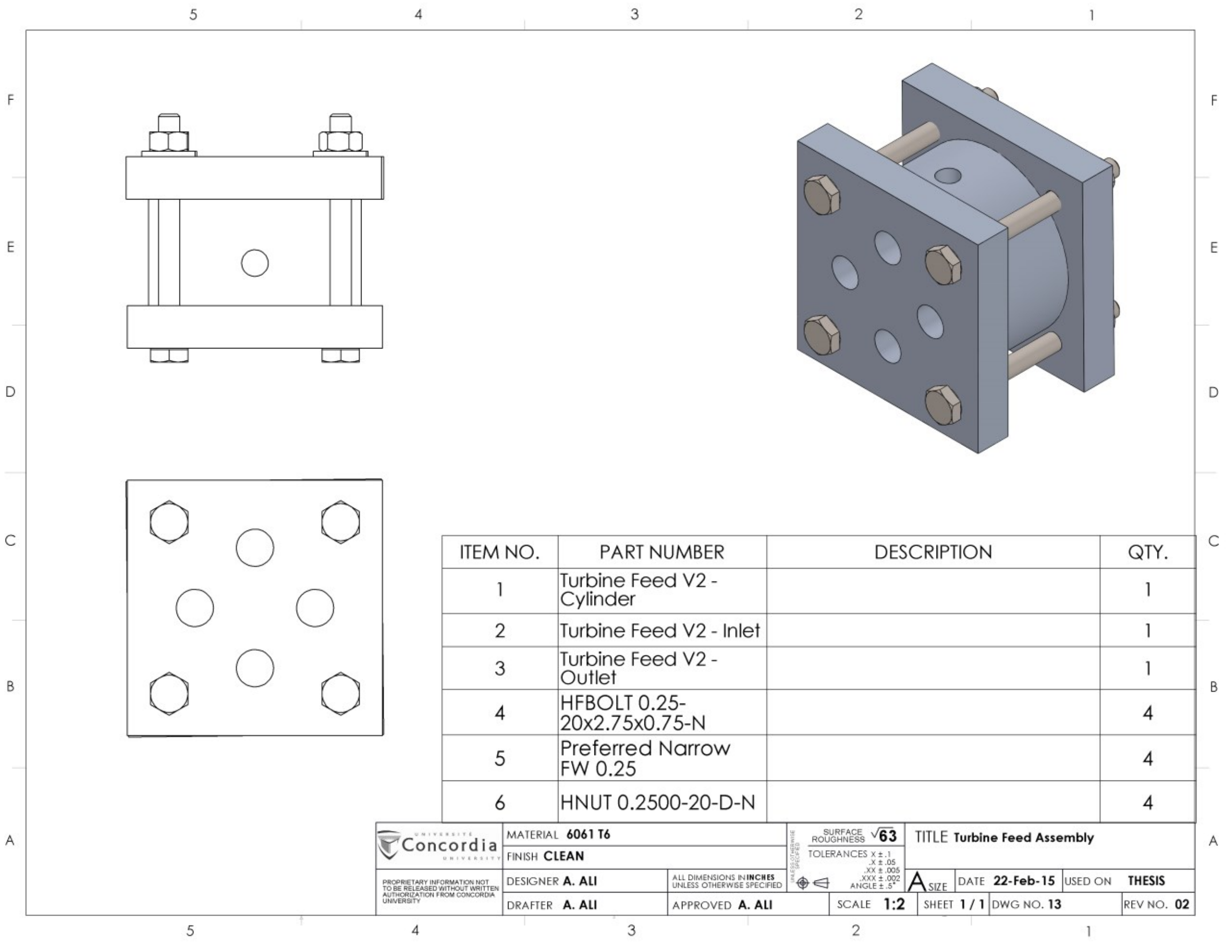

ITEM NO.	PART NUMBER	DESCRIPTION	QTY.
1	Turbine Feed V2 - Cylinder		1
2	Turbine Feed V2 - Inlet		1
3	Turbine Feed V2 - Outlet		1
4	HFBOLT 0.25-20x2.75x0.75-N		4
5	Preferred Narrow FW 0.25		4
6	HNUT 0.2500-20-D-N		4

Université Concordia University
PROPRIETARY INFORMATION NOT TO BE RELEASED WITHOUT WRITTEN AUTHORIZATION FROM CONCORDIA UNIVERSITY
MATERIAL **6061 T6**
FINISH **CLEAN**
DESIGNER **A. ALI**
DRAFTER **A. ALI**
ALL DIMENSIONS IN **INCHES** UNLESS OTHERWISE SPECIFIED
APPROVED **A. ALI**
UNLESS OTHERWISE SPECIFIED
SURFACE ROUGHNESS √**63**
TOLERANCES X ± .1 .X ± .05 .XX ± .005 .XXX ± .002 ANGLE ± .5°
SCALE **1:2**
TITLE **Turbine Feed Assembly**
A SIZE
DATE **22-Feb-15**
USED ON **THESIS**
SHEET **1 / 1**
DWG NO. **13**
REV NO. **02**

Figure E.13 CAD Drawing of Turbine Feed Assembly

APPENDIX F PRELIMINARY CFD ANALYSIS

This section has been added simply to serve as an initial idea of effect of the fin addition in both the water jacket and inside the exhaust runners. Both sides employed the K-Epsilon turbulence method using the intensity and length scale and used a wall surface roughness of $2 \cdot 10^{-6} m$. The inlet boundary condition was a mass flow corresponding to the case and the outlet was an outflow.

Water Side:	**Exhaust Side:**
K-Epsilon:	K-Epsilon:
- 8% turbulence	- 6% turbulence
- Turbulent length: 0.0007147	- Turbulent length: 0.002542
Inlet Boundary Condition:	Inlet Boundary Condition:
- Mass flow rate	- Mass flow rate
- 800000 Pa	- 105000 Pa
Outlet: outflow	Outlet: outflow
Wall: 0.000002 m roughness	Wall: 0.000002 m roughness

2475 RPM – Water Flow

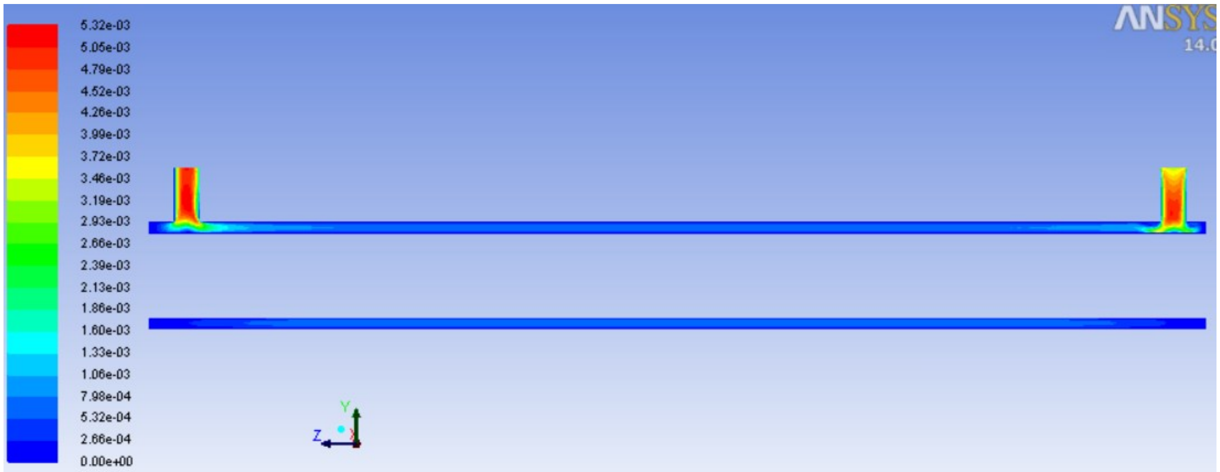

```
  Area-Weighted Average
     Velocity Magnitude                   (m/s)
-------------------------------- --------------------
                          inlet        0.0033967053
                         outlet        0.0033827007
              ---------------- --------------------
                            Net        0.0033897029
```

Figure F.1 CFD Results Water Flow 2475 RPM – No Fins

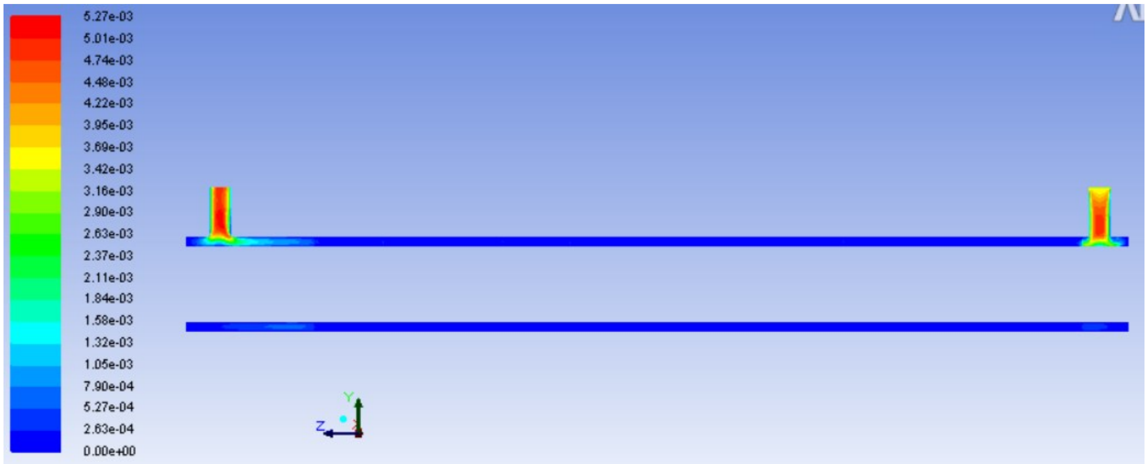

```
  Area-Weighted Average
     Velocity Magnitude                   (m/s)
-------------------------------- --------------------
                          inlet        0.0033967053
                         outlet        0.0033773645
              ---------------- --------------------
                            Net        0.0033870349
```

Figure F.2 CFD Results Water Flow 2475 RPM – Fins

8028 RPM – Water Flow

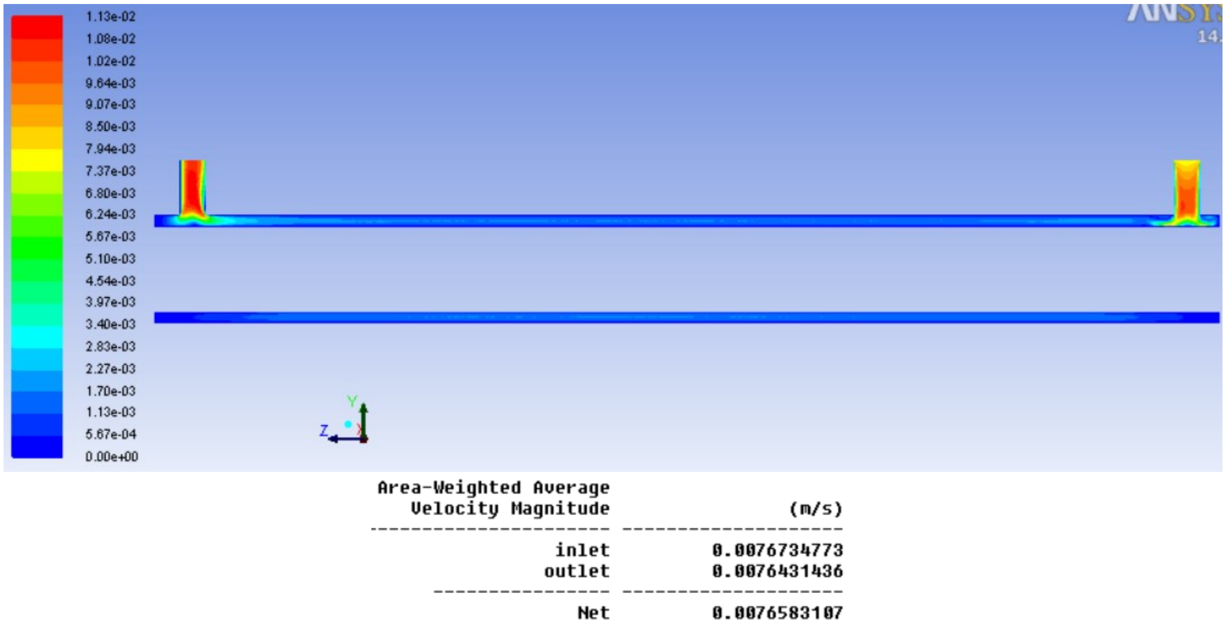

```
         Area-Weighted Average
           Velocity Magnitude                 (m/s)
 ----------------------------- --------------------
                        inlet          0.0076734773
                       outlet          0.0076431436
         -------------------- --------------------
                          Net          0.0076583107
```

Figure F.3 CFD Results Water Flow 8028 RPM – No Fins

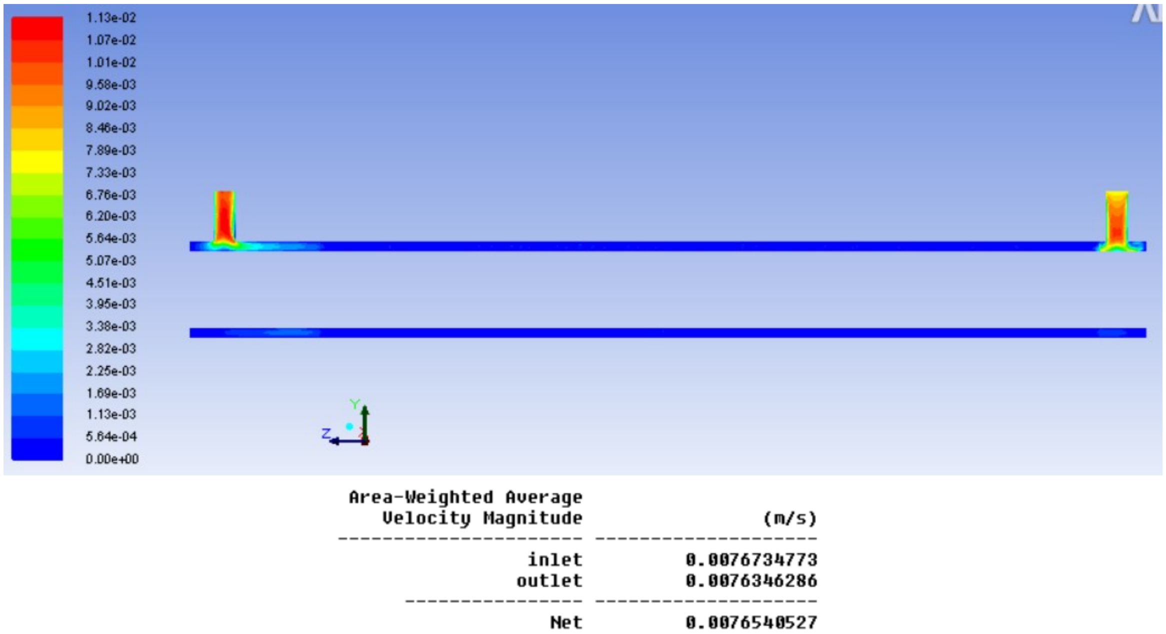

```
         Area-Weighted Average
           Velocity Magnitude                 (m/s)
 ----------------------------- --------------------
                        inlet          0.0076734773
                       outlet          0.0076346286
         -------------------- --------------------
                          Net          0.0076540527
```

Figure F.4 CFD Results Water Flow 8028 RPM – Fins

2475 RPM – Exhaust Flow

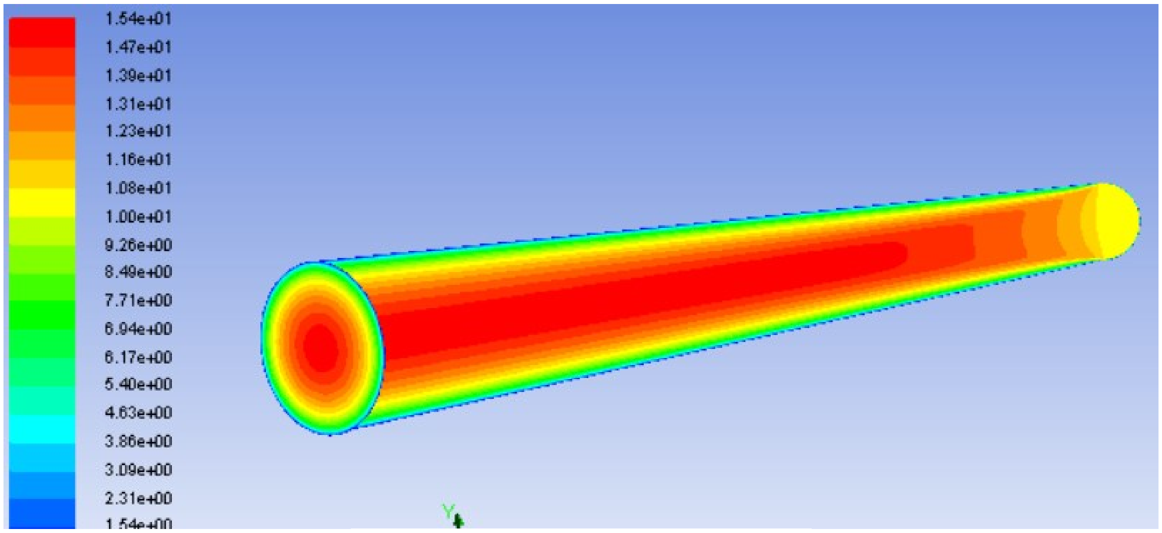

```
Area-Weighted Average
   Velocity Magnitude                  (m/s)
---------------------- --------------------
                inlet             10.654086
               outlet             10.636148
     ---------------- --------------------
                  Net             10.645118
```

Figure F.5 CFD Results Exhaust Flow 2475 RPM – No Fins

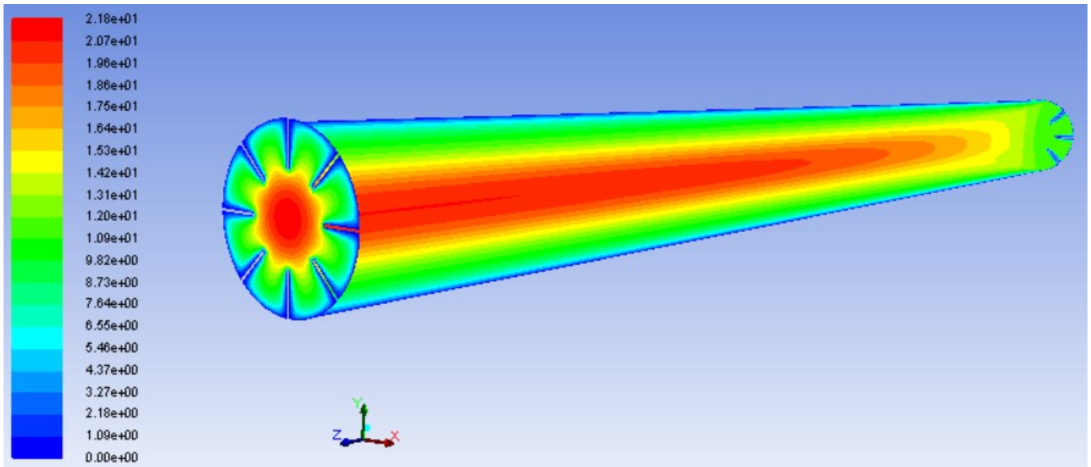

```
Area-Weighted Average
   Velocity Magnitude                  (m/s)
---------------------- --------------------
                inlet             11.040429
               outlet             10.991185
     ---------------- --------------------
                  Net             11.015807
```

Figure F.6 CFD Results Exhaust Flow 2475 RPM – Fins

8028 RPM – Exhaust Flow

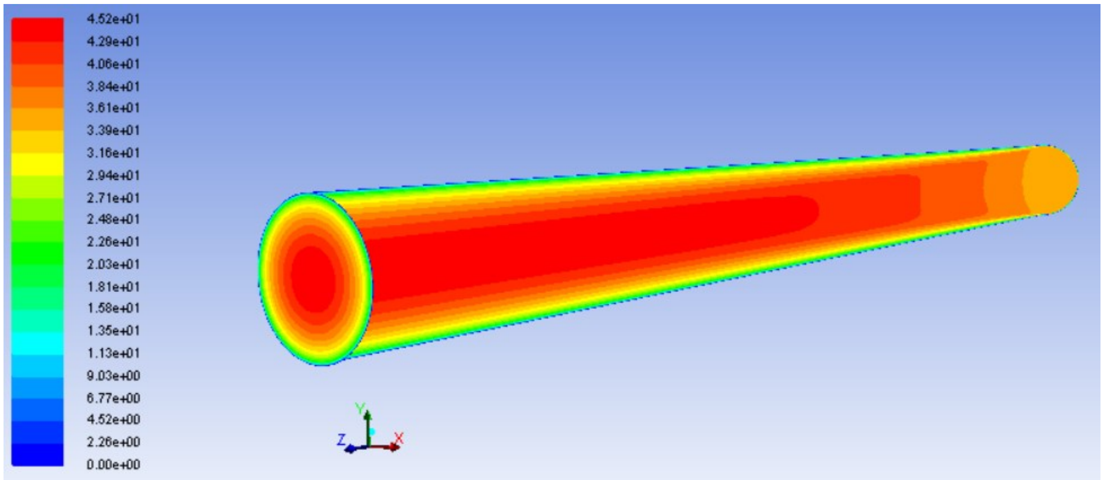

```
Area-Weighted Average
   Velocity Magnitude                  (m/s)
---------------------- --------------------
                inlet            34.566875
               outlet            34.536221
     ---------------- --------------------
                  Net            34.551548
```

Figure F.7 CFD Results Exhaust Flow 8028 RPM – No Fins

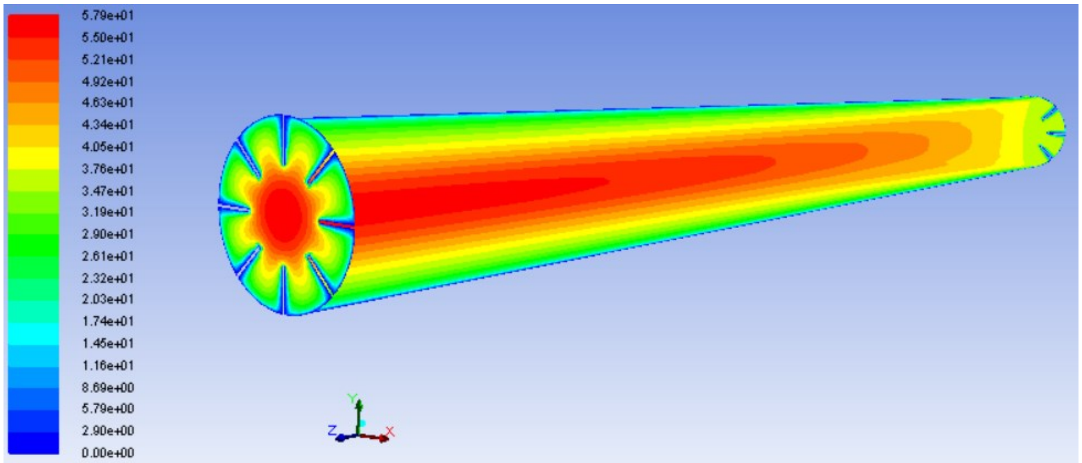

```
Area-Weighted Average
   Velocity Magnitude                  (m/s)
---------------------- --------------------
                inlet            35.820358
               outlet            35.747002
     ---------------- --------------------
                  Net             35.78368
```

Figure F.8 CFD Results Exhaust Flow 8028 RPM –Fins